Università degli Studi di Firenze

DIPARTIMENTO DI MECCANICA E TECNOLOGIE INDUSTRIALI

DOTTORATO DI RICERCA IN PROGETTO E SVILUPPO DI PRODOTTI E PROCESSI INDUSTRIALI

SETTORE SCIENTIFICO DISCIPLINARE ING-IND/14

CICLO XXV

ANALISI DELLE SOLLECITAZIONI STATICHE ED AFFATICANTI IN COMPONENTI DI FORCELLE MOTOCICLISTICHE

DOTTORANDO:

ING. MASSIMILIANO DE AGOSTINIS

TUTOR:

PROF. ING. DARIO CROCCOLO

CONTRORELATORE:

PROF. ING. ANTONIO STROZZI

COORDINATORE DEL DOTTORATO:

PROF. ING. MARCO PIERINI

ANNI 2010/2012

Try not. Do, or do not. There is no try.

Master Yoda

In memoria di Annamaria Fabbrini

Abstract

Lo studio in oggetto ha come obiettivo l'analisi delle sollecitazioni, statiche ed affaticanti, agenti in componenti di sospensioni anteriori motociclistiche. Viene presentata una breve introduzione storica alla sospensione anteriore motociclistica, incentrata sull'architettura oggi maggiormente diffusa, ovvero la forcella teleidraulica. Si passa poi ad esaminare il comportamento degli elementi strutturali chiave della forcella, quando questa viene interessata da carichi di flessione agenti nel piano della ruota del motoveicolo. Tale condizione di carico è di particolare interesse, perché si verifica frequentemente durante la vita del prodotto: si pensi, ad esempio, alla fase di frenata. Infatti, i capitolati di collaudo dei principali costruttori di motoveicoli prescrivono prove sulla forcella tese a ricreare la condizione di frenata d'emergenza. E' stato quindi definito un modello analitico per il calcolo dello stato di tensione nei principali componenti della forcella sotto l'azione di momenti flettenti dovuti alla frenata. Il modello tiene conto di alcune varianti costruttive e di numerosi parametri geometrici della forcella e del motoveicolo. La validazione del modello è stata condotta, in riferimento ad alcuni esemplari reali di forcella, sia mediante confronto con analisi agli elementi finiti che mediante prove estensimetriche su strada. Nel caso di forcelle monodisco, ci si è soffermati sull'analisi dello squilibrio di carico che si verifica fra le due gambe in condizioni di frenata, proponendo alcune strategie di ottimizzazione strutturale. Note le sollecitazioni esterne agenti su ciascuna delle gambe della sospensione, si è passati poi ad analizzare lo stato tensionale della giunzione fra gambe e trapezio inferiore. Tale giunzione è caratterizzata da componenti di tensione statiche dovute all'assemblaggio e da una componente di tensione esterna, variabile nel tempo. Le componenti di tensione statiche provocano una deformazione locale della gamba che implica un innalzamento locale delle tensioni dovute ai carichi d'esercizio. La giunzione è quindi soggetta a cedimenti per fatica. Una parte considerevole delle attività è stata perciò dedicata allo studio della letteratura e, successivamente, allo sviluppo di modelli numerici semplificati che consentissero di simulare il comportamento di detta giunzione. Tali modelli serviranno come base per sviluppare in futuro una metodologia utile per il calcolo dei coefficienti di concentrazione delle tensioni, avente come parametri in ingresso i dati geometrici e di materiale dei componenti. Sono state valutate l'applicabilità e l'efficacia di parametri normalizzanti presenti in letteratura, in grado di descrivere i coefficienti di concentrazione teorica delle tensioni per una intera classe di giunti. L'ambito di applicazione di tali parametri normalizzanti, presenti in letteratura per il caso di albero pieno, è

stato esteso al caso di albero cavo. Infine, è stata progettata una campagna di prove di fatica a flessione rotante, che ha comportato lo sviluppo di una particolare geometria di provino. I risultati ricavabili da tali prove saranno utili per la taratura di futuri modelli numerici.

-

The aim of this study is to analyse the static and fatigue stresses on front motorbike suspension components. After a historical review of front motorbike suspensions, attention is paid to the telehydraulic fork, which is the most common kind of front suspension nowadays. Then, the behaviour of the key structural elements of the fork is examined, under the assumption that the fork is subject to a bending moment acting on the front wheel mid-plane. Such a loading condition is worth of interest, because it happens frequently during the product lifecycle, consider for example the braking manoeuvre, and, moreover, it is part of the testing specifications of the main motorbike producers. It was conceived an analytical model useful for calculating the stress state of the main structural components of the fork under said loading condition. Such a model takes into account some architectural configurations as well as some characteristic geometrical parameters of the fork and of the motorbike. The model was validated referring to some production forks, both by finite element analyses and by experimental mechanics tests on the road. In the case of single brake disc forks, a remarkable effort was made to analyse the load unevenness between the legs during braking, and to propose some strategies aimed at reducing such loading unbalance. Once the external loads distribution was understood, the stress state of the joint between the lower fork clamp and the legs was analysed. Such a joint is characterized by the presence of static stress components due to the assembly and of a time dependent component due to the fork duty cycle. The static stress components are associated with a deformation of the leg which brings about a concentration of the stress due to the superposition of duty cycle loads, which usually determine fatigue failures. A considerable part of the activities was then dedicated to a literature review, aimed at retrieving a numerical model which could simulate accurately the stress state in the vicinity of the joint. Such model will serve as a base for developing a methodology for the calculation of stress concentration factors in said joint. The applicability and effectiveness of a normalizing parameter found in the literature was also evaluated. Such normalizing parameter is available limited to the case of solid shaft: its applicability was extended to the case of hollow shaft. Lastly, a fatigue experimentation was designed, which required the development of an innovative specimen. Results obtained from such experimentation will serve as a reference for the future development and validation of new numerical models.

Summary

1 Introduction **1**

2 Structural analysis of motorbike forks **17**
2.1 Experimental stress analysis 17
2.2 Basics of tire dynamics 24
2.3 The analytical model 27
2.4 Numerical validation of the analytical model 36
2.5 Structural optimization of single disc forks 42

3 Stress analysis of shaft-hub joints in motorbike forks **49**
3.1 Field failures 49
3.2 The fork clamp - leg joint 51
3.3 Stress analysis of the axisymmetric shaft hub joint 52
3.3.1 Hollow shaft 55
3.3.2 Numerical example - hollow shaft 64
3.3.3 Mixed materials 66
3.3.4 Frictional contact 67
3.3.5 External loads 74

4 Fatigue tests **85**
4.1 Materials and methods 85
4.1.1 Design of the specimens 85
4.1.2 Material 90
4.1.3 Measurements and pairs matching 91
4.2 Results 93
4.3 Appendix 97
4.3.1 Drawings 97
4.3.2 Plain specimen - fracture surfaces 98
4.3.3 Shaft hub specimen - fracture surfaces 99

5 Conclusion **101**

Bibliography **103**

Chapter 1

Introduction

Since the late 19^{th} century, engineers started to develop mechanisms aimed at improving the riding comfort of bicycles. Early solutions comprised one or more springs placed at some point of the bicycle framing, which enabled the wheels to rise and fall without communicating vibrations to the central part of the framing itself, the steering bar, the saddle, and therefore to the hand of the rider and to his body. An example of such devices can be appreciated in Fig.1.1 which refers to a U.S. patent dating back to 1901 [1]. The mechanism shown in Fig. 1.1 may be

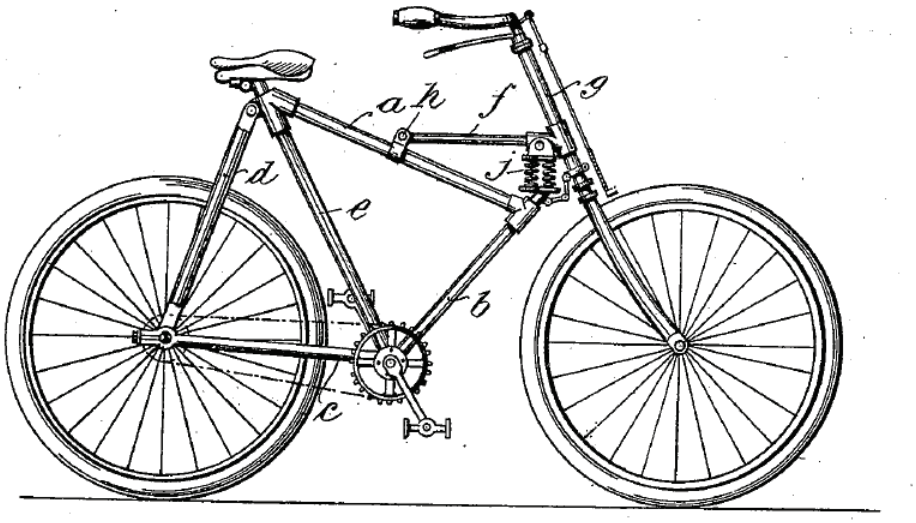

Figure 1.1: 1901 bicycle with spring suspended handlebar, U.S. Patent No.680,048, inventor Emil Koch.

regarded as a first form of front suspension. At that time, devices providing some sort of insulation of the saddle from the road irregularities were already available and covered by patents [2]. Unless the first motorbike appeared in 1869, we have to wait four decades to see the first example of front motorbike suspension, shaped

as a fork [3]. It was introduced by the Scott Motorcycle Company of Shipley, West Yorkshire, England. Referring to Fig. 1.2, it can be seen a mechanism placed in front of a common bicycle fork, which carries the front wheel of the motorbike on the lower, U-shaped ends of its legs. The wheel is decoupled from the main frame

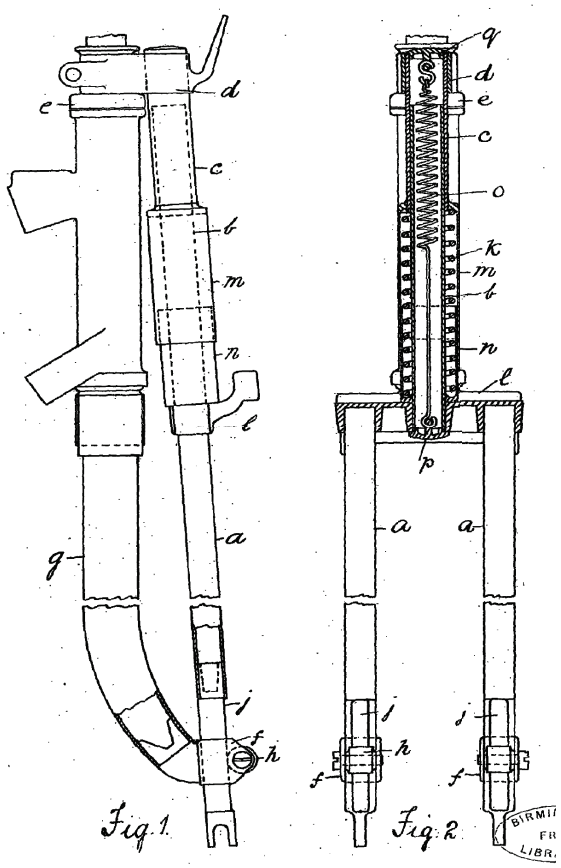

Figure 1.2: 1909 front fork with single coil spring for motorbike, G.B. Patent No.7,845, inventor Alfred Angas Scott.

of the bicycle by means of a couple of tubes sliding with respect to each other, sitting in the middle of the steering crown and attached on top of the steering pin. There are two coil springs inside the tubes, the outer spring is compressed when external loads are applied to the wheel while the internal one is always loaded in tension and its only function is to check the recoil of the compression spring. Although original, this arrangement had little practical application and it is no longer in use. One of its major flaws, shared with its forerunners, is that a single , constant pitch, compression spring may hardly adapt to shocks characterized by an extremely wide amplitude range, like those encountered in a normal ride. In fact, if the spring was too stiff, it would not filter the road

roughnesses when travelling over comparatively smooth roads. On the contrary, a highly flexible spring would be entirely compressed when clearing a severe bump or travelling over comparatively rough roads, thus transmitting undesired vibrations to the rider. In 1914, Arthur Otto Feilbach, founder of Feilbach Motor Co. of Milwaukee, Wisconsin, obtained a patent in the United Kingdom for a motorbike fork comprising a spring preload adjustment mechanism. Such a device can be seen in Fig. 1.3: by means of the nut 19, the spring preload can be adjusted by the rider to adapt to different tracks. Anyway, such a device would not allow to

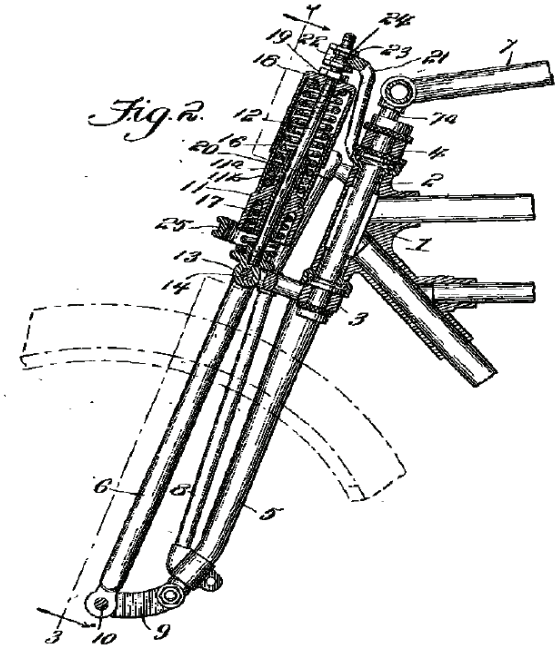

Figure 1.3: 1914 Improvements in Forks for Velocipedes, Motor Cycles and the like, G.B. Patent No.11,301 inventor Arthur Otto Feilbach.

cure all the deficiencies listed above, because the spring setting is still constant during the whole compression and extension strokes. In the early years of 19^{th} century, a young apprentice worked at Feilbach's shop in Milwaukee: his name was William S. Harley, who surely leveraged some of the Feilbach's solutions for developing his own motorbikes. In fact, an invention patented by W. S. Harley in 1925 [4] was designed to overcome the aforementioned limitations. Referring to Fig. 1.4 it can be seen that this architecture is provided with two legs each side, and the front wheel is pivoting around a pin placed at the end of the rear leg. Fig. 1.5 shows some sectional views of the suspension, where four different sets of springs can be identified. Each set is made up of two identical springs, and it is characterized by a certain number of coils, wire cross sectional area and spring

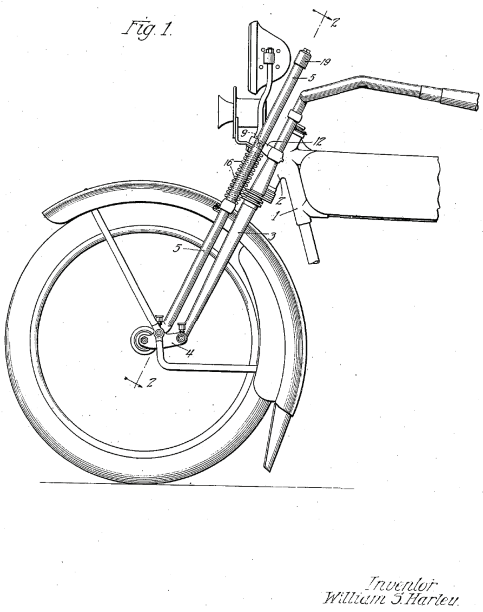

Figure 1.4: side view of 1925 front fork for motorbike, U.S. Patent No.1,527,133 inventor William S. Harley.

index. These three characteristic parameters, along with the modulus of elasticity of the spring wire determine the spring stiffness. So the four sets of springs have different stiffnesses. The two sets of springs contained into the tubes have the lowest stiffness, but a high preload, and serve as compression and rebound springs (dashed line in Fig. 1.6). Owing to the high preload, they readily absorb minor shocks such as encountered when travelling on relatively smooth roads. Conversely, the two long external cushion springs, which sit on top of the lower fork clamp, are characterized by a higher stiffness and a much lower preload (dash-dot line in Fig. 1.6). Owing to the low preload, these springs do not become effective until a relatively severe bump is encountered. The springs of the shortest set are called bumper springs and come into action when very severe bumps are encountered, and the other sets of springs are almost fully compressed (Thin solid line in Fig. 1.6). The overall elastic behaviour of the fork is represented by the solid thick line in Fig. 1.6. Although with some refinements, this architecture can be seen nowadays on some motorbikes produced by Harley Davidson Inc. Among others, the absence of any damping device, the relatively complex springs arrangement, the relatively high weight and a less than optimal serviceability may be cited as the main flaws of this architecture. In 1934, Great Britain patent number 416,594 by Fisker and Nielsen [5] claims the invention of a telescopic fork with internal springs and easily detatchable wheel axle for improved serviceability. This design

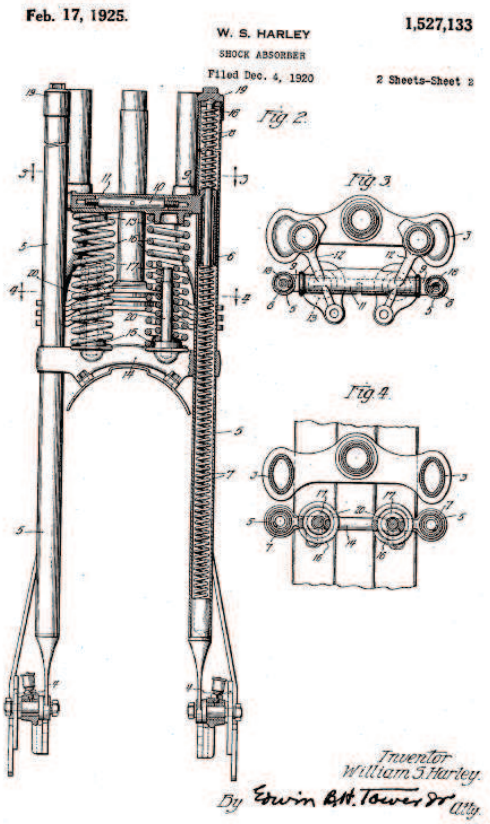

Figure 1.5: three section views of 1925 front fork for motorbike, U.S. Patent No.1,527,133 inventor William S. Harley.

was introduced on the 1934 Nimbus Type C motorbike. There are provided two springs and two telescopic legs (one spring per leg). Each leg ends with a U-shaped recess similar to that shown in Fig. 1.2. The wheel axle is secured to the legs by means of its threaded extremities. This improves serviceability, as the wheel can be easily removed by untightening two nuts on the wheel axle and pulling the wheel downwards. The solution is simple in design and relatively cheap to manufacture and assemble, as well as lighter than older designs which used external components and linkage systems. Its clean appearance makes it resemble modern motorcycle forks: nonetheless, it is expected that such a simpler spring arrangement can not ensure the same comfort performance as the invention of W. S. Harley shown previously. A few years later, a milestone of suspension design was put forward by Rudolf Schleicher of Bayerische Motoren Werke (BMW) and covered by a deutsch patent in May 1939 [6]. This is the first example of telescopic fork with integrated hydraulic shock absorber, and the 1935 BMW R12 motorbike

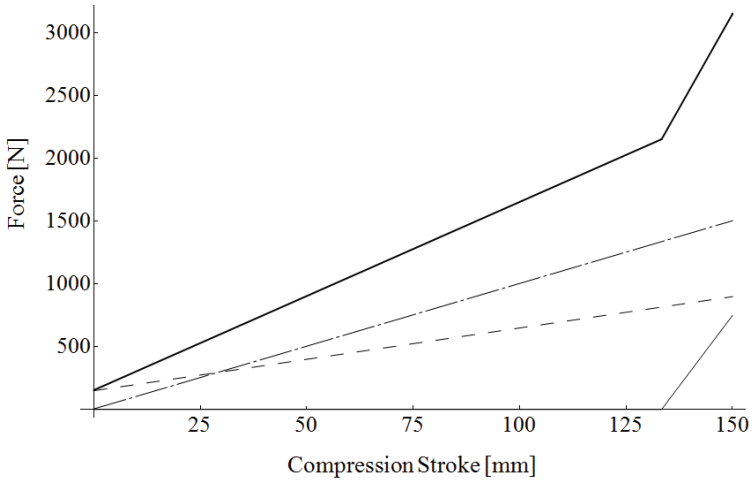

Figure 1.6: qualitative compression behaviour of a front fork like that of U.S. Patent No.1,527,133.

was already equipped with it. It consists of a telescopic fork inside which are added two tubes and a stem carrying a check valve at its lower end: these tubes are filled with a convenient amount of hydraulic fluid. Refferring to the notation in Fig. 1.7, the check valve 10 divides the lower fork tube 1 into a lower and an upper chamber. From the sectional view on the right side of the picture, it is possible to appreciate that a couple of sliding bearings support the movement of the telecopic tubes. During the compression stroke, as a consequence of the upward movement of the lower fork tube 3, of the shock absorber tube 1 and of the guide member 6, a depression is produced above the upper surface of the valve 10. Thus, the valve is drawn up and a free passage is created for the hydrauic fluid flowing from the lower to the upper chamber. This means that during the compression stroke the fork moves without any damping effect. Conversely, during the rebound stroke, the downward movement of the three aforementioned components makes the valve close, forcing the oil to flow through the small annular area between the stem 8 and the guide member 6, and eventually going back to the lower chamber by means of the comparatively large passages 15. Since the annular orifice section and the cross section of the valve are fixed, and the fluid kinematic viscosity is known, it is possible to calculate the pressure drop across the orifice, which is a function of the flow, and therefore of the sole rebound velocity. Such a valve arrangement is peculiar to motorbike forks, and, with slight differences, it can be found on some motorbikes still today. This solution had a few deficiencies too, as for example the dependency of the rebound damping level on the diametral gap between the guide member 6 and the stem 8. It must be remarked that the asymmetric behaviour between compression and rebound strokes is desirable, because relatively low damping in compression allows the wheel to follow the waviness of the road, ensuring a certain roadholding capability to the vehicle.

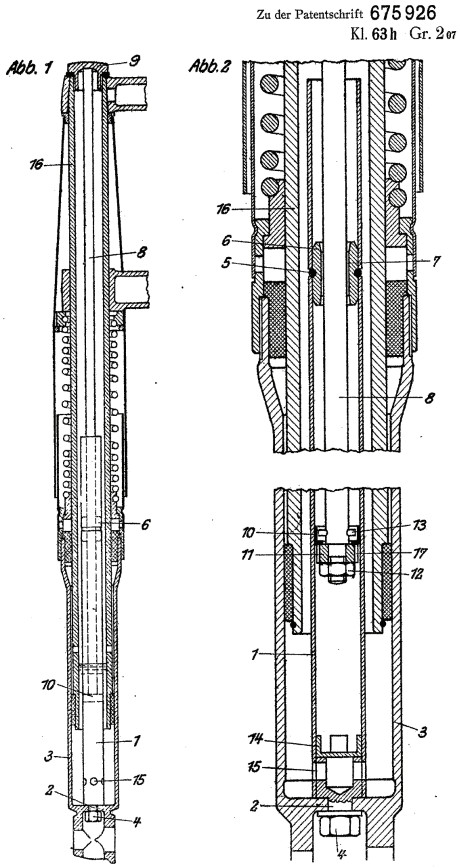

Figure 1.7: Hydraulic shock absorber for motorcycle forks, DE Patentschrift 675,926, inventor Rudolf Schleicher.

At the same time, a stiffer damping on the rebound stroke helps cutting the oscillations of the vehicle body, thus improving comfort. Note that the spring lies outside the hydraulic damper and it is mounted with a certain preload between the lower fork clamp and the stanchion. The tube is retained to the fork clamps by means of a fixed ring under the lower clamp and a nut 9 tightened against the steering fork clamp. An evident drawback of this architecture is that the particular arrangement of the springs does not allow to have a long stroke of the tubular members. Therefore it can likely happen that such stroke would be insufficient when travelling over a rough asphalt surface or on offroad tracks. Perhaps the solution proposed by three engineers of Dowty Equipment Ltd. in 1948 aimed at fixing some of those issues, by replacing the helical spring with a gas spring [7]. As it can be seen in Fig. 1.8 the legs are filled with oil up to the level marked by balloon number 33. An air chamber is formed at the top of each tube, and the two air chambers are in communication with each other through a duct realized

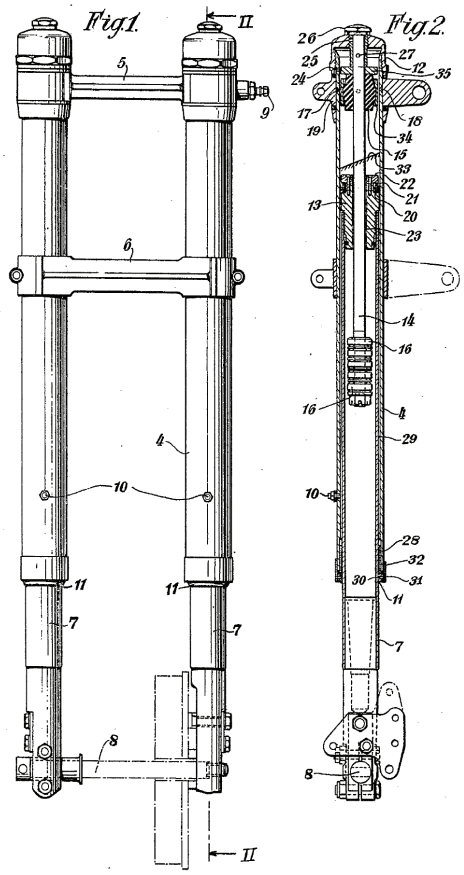

Figure 1.8: An improved telescopic strut or shock absorber, GB Patent 597,036, inventors Peter Walter Burke, Richard Philip Wildey Morris and Arthur Adrian John Willit.

inside the steering clamp. The air pressure can be adjusted to the desired level by means of the inflation valve 9. While the resilience of the fork is afforded by the compressed air, damping is due to the resistance to liquid flow created by the damping heads 16. Such damping heads shall have an established axial length, in order to provide a "frictional" rather than an "orifice-like" damping. Since the fork has no springs, the inventors had to provide some means to arrest the sliding tubes at the stroke extremities. In fact, the damping head consists of a stack of Belleville washers: when, at the end of the extension stroke, said damping head comes into contact with the annular gland 13, the upward movement is arrested gradually, owing to the resilience of the washers. The same effect is obtained for the compression stroke by placing a rubber element 15 beneath the upper cap 12. An attentive observer will surely notice that this one seems to be the

first example of upside-down telescopic hydraulic fork in history. Upside-down forks have their legs arranged so that the outer tubes (or stanchions) are in the upper part of the fork and joined to the triple clamps. This solution provides a greater flexural stiffness to weight ratio, therefore, still today it is used in high end forks for sports motorbikes. During the 1950s, various systems for replacing

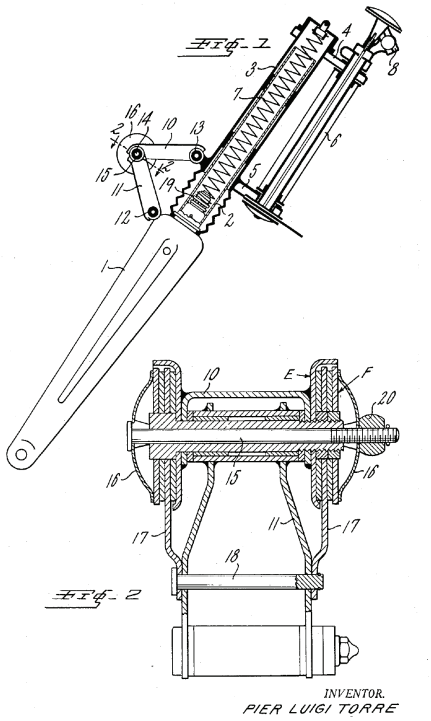

Figure 1.9: Spring suspension system for motorbike front wheels, U.S. Patent 2,756,070, inventor Pier Luigi Torre.

the elastic elements or the viscous damper were presented. A good example could be the invention by Pier Luigi Torre of 1956 [8]. Such architecture has a dry frictional damping element instead of the hydraulic one. There is provided a stack of frictional disks, like those present in a transmission clutch, held together by means of a threaded preloading mechanism which allows to adjust the damping effect to the rider's needs (Fig. 1.9). This solution had little fortune, because it can be no longer seen on any motorbike. During the same years, some new designs for the front suspension of mopeds were presented, among which that by NSU Werke Aktiengesellschaft [9] and that by Edward Turner of Triumhp Engineering Ltd. [10] are prominent. Both of them can not be defined forks, as they are basically single arm suspensions: two sectional views of the second one can be seen in Fig. 1.10. In spite of that, especially Turner's invention, originally applied to the 1958 Triumph Tigress (a scooter designed to have good performance and

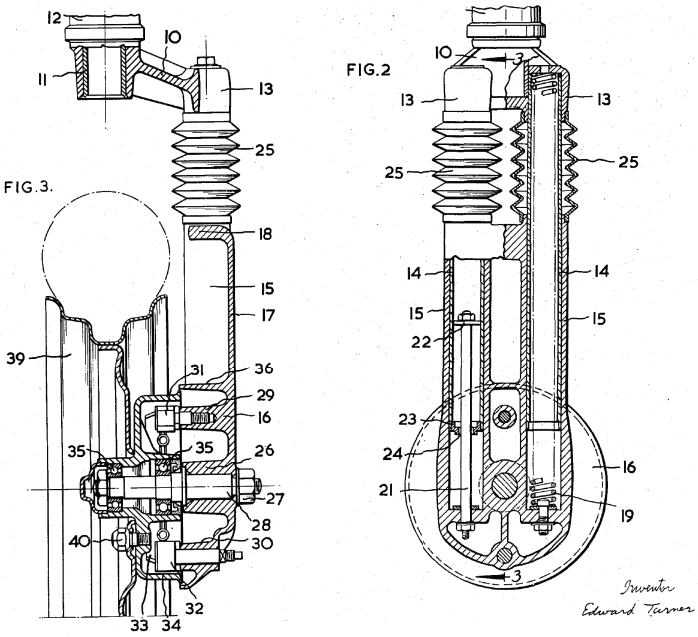

Figure 1.10: Motorcycle front wheel suspension, U.S. Patent, 2,953,395 inventor Edward Turner.

handling for the motorcycle enthusiast), deserves citation because it introduces a clever innovation. From the sectional view on the right of Fig. 1.10 it can be seen that there are actually two struts on the left side of the front wheel. One strut has a coil spring in it (the elastic element) while the other one has a viscous damper like those shown above. Therefore, instead of having hydraulic and elastic elements on both the struts, the two functions are separated and much less components are used. Since they are rigidly connected, the two elements still work in parallel as a mass-spring-damper system. Such a device is currently used for cheaper motorbike forks. It is worth observing that the tubes 14 are secured to the steering crown 13 by brazing or by interference fitting. At the end of the sixties, some detail improvements were put forward with a new design by Joseph P. Roberts [11]. He developed a front fork comprising a hydraulic cushioning device working at extreme stroke positions and a lengthened helical spring. Referring to Fig.1.11, which represents the check valve 66 and the stem 64 approaching the lower end of the stroke (the fork is almost fully compressed), it can be seen how the hydraulic fluid is trapped into a chamber created by the tube 82, the sliding bearing 48 and the outer tube 28. In the light of that, the oil can only flow to the low pressure chamber leaking from between the sliding bearing and the outer tube. Such a small passage area determines a great pressure differential between the two chambers, and then a noticeable cushioning effect on the fork. The conical shape of the element number 60, makes the transition between low damping high damping conditions be smooth.

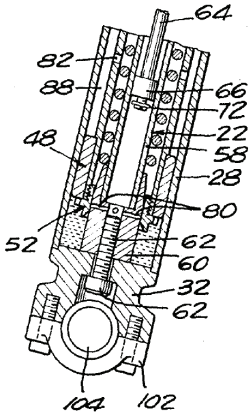

Figure 1.11: Telescoping, spring-loaded, hydraulically damped shock absorber, U.S. Patent, 3,447,797 inventor J. P. Roberts.

Since the seventies, such a cushioning device has been installed on almost every fork. As for the helical spring of increased length, it is conceived to allow for a greater stroke with respect to more classical designs. In fact, the spring lower end is sitting on the bottom of the outer tube, instead of on top of the tube 58, as it happened on previous products. In the meanwhile, suspension designers began to experiment more sophisticated springing and damping devices, in order to fulfill the demand for increased roadholding capabilities coming from sports motorbikes enthusiasts and from competitions. A good example [12] could be the fork patented in 1979 by the italian producer Arces S.r.l. (the acronym means Arturo Ceriani sospensioni). It is known that the great majority of motorbike forks are filled with hydraulic fluid up to a certain level inside the telescopic tubes. Above the hydraulic fluid there is air at ambient pressure. When a vehicle equipped with such a fork travels over a hard bump or clears a step, could happen that, due to the rapid movement, some air bubbles could be entrapped inside the hydraulic fluid. Therefore the fluid changes its behaviour, causing a degradation of the suspension performance. Moreover, motorbike forks usually have two independent hydraulic circuits (one each leg), therefore, since the alteration of the fluid behaviour could be asymmetric for the two circuits, the resulting dynamic behaviour of the fork could be unbalanced and eventually dangerous for the rider. The invention by Arces consists of a fork having each leg provided with a sort of bladder accumulator, housed into a recess realized in the fork stanchion, as shown on the left side sectional view of Fig. 1.12. In the same view, it can be seen that the hydraulic fluid is contained into the chamber 19 created between the stanchion 4, the tube 3 and the inner tube 15. As the tube dives into the stanchion (compression stroke), the oil flows through the check valve 27 and the flow regulator 32 to the accumulator chamber 26. The oil is pressurized by the action of the elastic bladder 29, inflated with compressed air via the check valve 31. During the rebound (or extension) stroke, the flow is inverted, then the fluid goes back to the chamber 15 by means

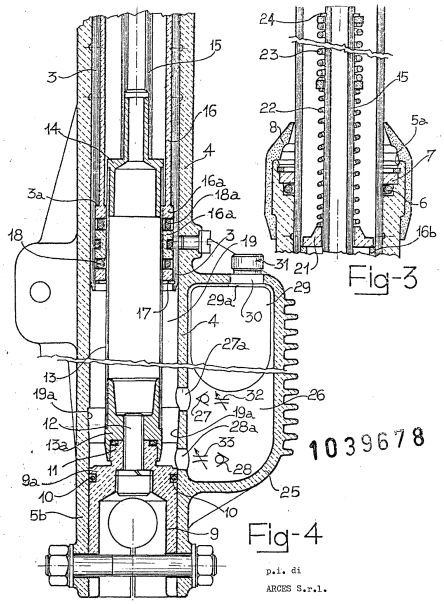

Figure 1.12: Improved hydraulic fork,Brevetto per invenzione industriale, 1,039,678, licensee Arces S.r.l.

of the check valve 28 and the flow regulator 33. Both the inflation pressure and the flow regulators can be easily adjusted by the rider via some external knobs. In this case, the fork has no compression spring: the elastic function is accomplished by the pressurized air. Therefore, the elastic characteristic of the suspension, in a displacement-force diagram, would be described by an hyperbola instead of a straight line. It is to be noted that a spring cushioning device is provided for the rebound stroke and a hydraulic one for the compression stroke. The advantage of the aforementioned architecture is that the hydraulic fluid does not come in contact with air, therefore the hydraulic characteristic of the suspension remains constant for long time intervals. The possibility of adjusting both the pressure level of the air (and therefore the elastic characteristic) and the damping level by means of dedicated knobs, was highly appreciated by off-road racers, among whom, in the seventies and in the eighties, such architecture became very popular. In 1981, Mitsuhiro Kashima of Kayaba Corp. Ltd. (a world renowned japanese fork producer), introduced the first anti-dive system [13]. Under the application of a braking force, the fork is urged to compress in response to inertial forces acting on the motorcycle. Such a phenomenon is known as "diving", and, if too much pronounced, it may lead to a considerable increase of the braking distance (i.e. the distance a vehicle will travel from the point where its brakes are fully applied to when it comes to a complete stop). Diving is directly proportional to the fork overall compressive compliance, but unluckily, increasing the spring stiffness would not be a good solution to the diving issue, because it would affect

the comfort characteristic of the fork. The solution put forward by Kashima

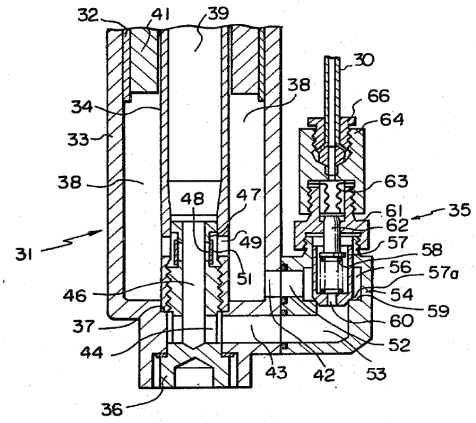

Figure 1.13: Anti dive mechanism for motorbike forks, U.S. Patent, 4,295,658, inventor Mitsuhiro Kashima.

and shown in the sectional view of Fig. 1.13 aims at limiting the natural diving tendency of the fork, without sacrificing its shock absorbing capabilities. The goal is achieved by implementing a hydraulic circuit which automatically switches between two different damping settings, one of which being used for the emergency brake condition and the other for the normal ride. The hydraulic circuit is made up of a first (38) and a second chamber (39). A normally closed check valve 57 divides the two chambers, and is forced to open by fluid pressure in the first chamber. As the fork is compressed, the hydraulic fluid flows from the first to the second chamber via said check valve. An actuator, responsive to the level of the braking force applied by the rider, increases the pressure required to open the check valve 57. This prevents the shock absorber from diving rapidly as a consequence of an emergency brake. As happens in any hydraulic circuit, shock absorbers comprise a great number of valves, working together to fulfil a precise function. In the case of vehicle suspensions, and especially those destined to motorbikes, a demanding task for a hydraulics engineer is managing to fit all the hydraulic functions in the smallest amount of space. An interesting solution pointing towards that direction, was presented, among others, by Gert Neupert and Heinz Sydekum of Fichtel & Sachs AG, as it appears in an italian patent specification dating back to 1986 [14]. Such a device, shown in Fig. 1.14 consists of a rigid piston with two series of concentric axial passages. Each passage is free at one extremity and closed at the other by means of an elastic element which can be deformed in one direction only. The elastic members have different stiffnesses, therefore determining different pressure drops depending on the flow direction. The piston can be fixed to the shaft 3 of a twin tube damper or to the inner tube of a fork. In a few words, the valve arrangement works as a flow regulator valve in one direction and as a check valve in the other direction. Pistons like that of Fig. 1.14 can be seen in a wide variety of motorbike forks as well as rear shock absorbers, because they are

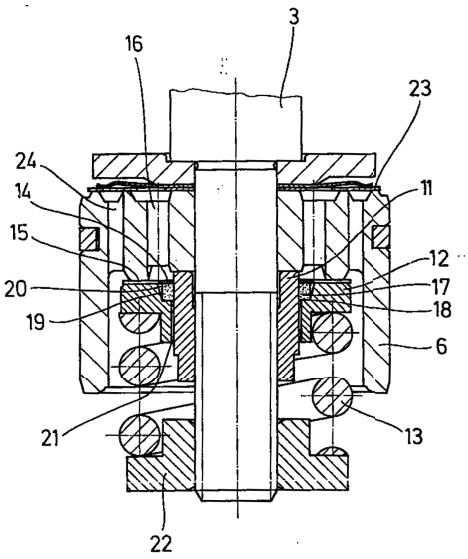

Figure 1.14: Unidirectional/Flow regulator valve for shock absorber, Brevetto per invenzione industriale, 1,145,747, inventors Gert Neupert and Heinz Sydekum.

compact, cheap to manufacture and characterized by a good reliability. Nowadays such system is used, in more sophisticated forks, in combination with adjustable orifices which work in parallel with the elastic elements of the piston. Usually, the adjustable orifices are sized in order to saturate above a certain oil flow value (and thereore above a certain compression/rebound speed). When the adjustable orifices saturate, the oil is forced to flow through the orifices on the piston. Such orifices are dimensioned in order to determine a higher pressure drop. Hence, it is possible to obtain a damping characteristic which depends on the travelling speed of the suspension reciprocating members. A device of the aforementioned kind can be found in the patent by Adrianus H. I. Verkuylen entitled "Hydraulic shock damper assembly for use in vehicles" [15]. Todays motorbike forks come in various forms, depending on their mission: the majority of small motorbikes and mopeds are equipped with simple traditional forks, whose basic characteristics do not differ too much from the design of Fig. 1.11. On the contrary, modern sports motorbikes (including off-road vehicles) usually adopt much more complicated architectures, most often in the up side-down configuration, in which the devices shown above combine to bring about accurate damping characteristics. Moreover, simpler forks usually have fixed damping and elastic settings while high performance forks allow the rider adjusting every single aspect of their dynamic behaviour. In order to give the reader an idea of what a modern high end fork looks like, it is reported in Fig. 1.15 a patent application of 1992, by Öhlins Racing AB. That is an up side-down fork in which are used a couple of piston valves like the one in Fig. 1.14, each working in one direction of the stroke. Moreover, in parallel with those valves,

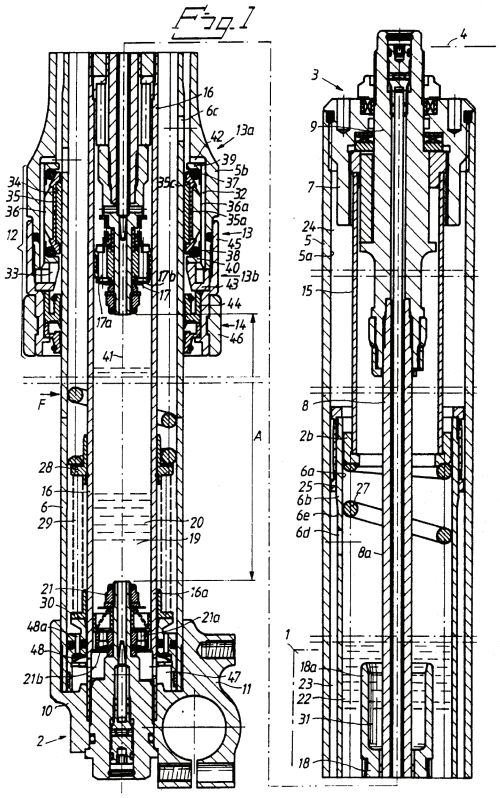

Figure 1.15: Modern up side-down fork, PCT Patent application, WO 92/16770, inventors Kent Öhlin and Mats Larsson.

two orifices work at low compression and rebound velocities. The settings of the two low velocity orifices are independent from each other, and adjustable from two socket head screws, the rebound one is housed in the cap of the stanchion (which means it is accessible from the steering clamp), while the compression one is placed on the bottom of the axle bracket. Although many improvements have been introduced in motorbike forks since the late 19^{th}, they can still be described as suspension members which includes a pair of telescoping tubes, one connected to the cycle frame by means of a triple clamp, and the other connected to the wheel axle. As the wheel receives a perturbation, the tubes are telescoped further within one another, which makes an enclosed hydraulic fluid flowing through one or more restricting orifices. At the same time, a coil spring is compressed. The two work together as a spring damper device, which serves to dampen shock and vibration effects received at the frame of the motorbike. In the next chapters, topics concerning the structural design of a motorbike fork will be treated more in detail.

Chapter 2

Structural analysis of motorbike forks

2.1 Experimental stress analysis

From a structural mechanics standpoint, the main frame of a motorbike fork consists of two telescopic legs, two fork clamps (or triple clamps) and a steering pin, put together by means of various joining techniques. The inner tube of each telescopic leg is generally referred to as "tube" while the other one is called "stanchion". Some nomenclature about the structural components of a motorbike fork is reported in Fig. 2.1 Whether the tubes or the stanchions are coupled with the

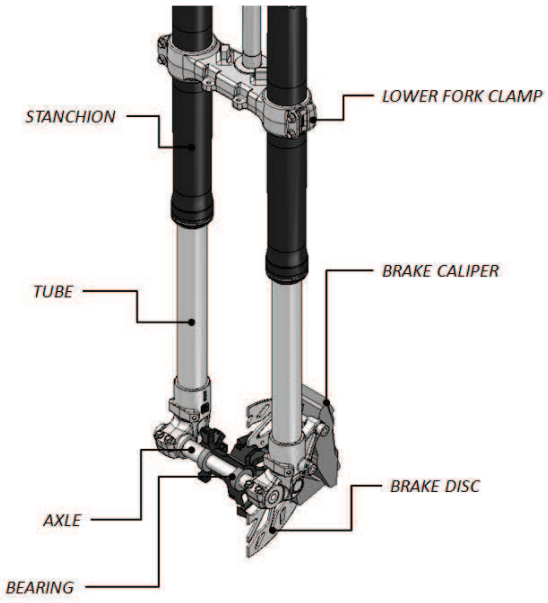

Figure 2.1: Essential structural components of a motorbike fork.

fork clamps, the fork architecture is named "standard", see Fig. 2.2 on the left , or "upside-down", see Fig. 2.2 on the right. Motorbike forks can be subdivided fur-

ther into single-disc and twindiscs architectures. In the past, single disc forks were the first choice for the great majority of motorbikes, but nowadays such devices will be reasonably found on low cost and small displacement motorbikes only, because the increase in performance and weight of sports motorbikes determined the success of twin discs architectures, which offer an increased braking power. A deep

Figure 2.2: Comparison between a standard fork (left) and an up side-down fork (right).

knowledge of the product lifecycle is the key for a correct design: for that reason, suspensions producers must carry out a number of road and bench tests in order to gather as much information as possible about their product. Several road tests carried out by the authors, led to defining the most severe loading conditions in terms of mechanical stress on the structural elements of the fork. In fact, the most part of field failures recorded on motorbike forks can be ascribed to bending loads on the legs, and happen in the vicinity of the lower fork clamp [16]: such a kind of failure is often tied to fatigue phenomena and/or impact loads. Fork producers are usually challenged by their customers to provide design proposals for a new product: this process must be completed in a short time, because the product development phase shortened appreciably in recent years. During that early phase, no CAD geometries of the fork are yet available so that the preliminary structural design cannot leverage FEA analyses. Up to few years ago, manufacturers used to develop a new fork based on the characteristic dimensions of a previous model. Then, by means of a trial and error process, they assessed the validity of a new design by means of experimental tests run on pre-series prototypes. Therefore, the aim of the present work is to provide an analytical model which, based on a few parameters of the fork and of the bike, can help engineers to assess in advance the structural behavior of the main components of the fork. In the past, such a methodology was applied by our research group at the University of Bologna, to

provide mathematical models describing the behavior of interference fitted connections between the steering pin and the fork clamps [17, 18, 19] and bolted connections between the fork clamps and the legs [20, 21, 22]. In order to assess the validity of the newly developed analytical model, it was compared with experimental data and with finite elements analyses (FEA). Extensive tests were carried out on an Enduro motorbike, equipped with the fork geometry shown in Figure 2.1, which will be referred to as Fork1. The Fork1 is produced by Paioli Meccanica: it belongs to the up side-down type and is comes with a single brake disc. The fork was instrumented with four HBM 1-LY43-3/120 strain gauges placed underneath the joint between the lower fork clamp and the stanchions. The strain gauges were glued to the external surface of the stanchions, with the main grid axis aligned with the tube axis (2.3). Each couple of strain gauges, half bridge configured [23],

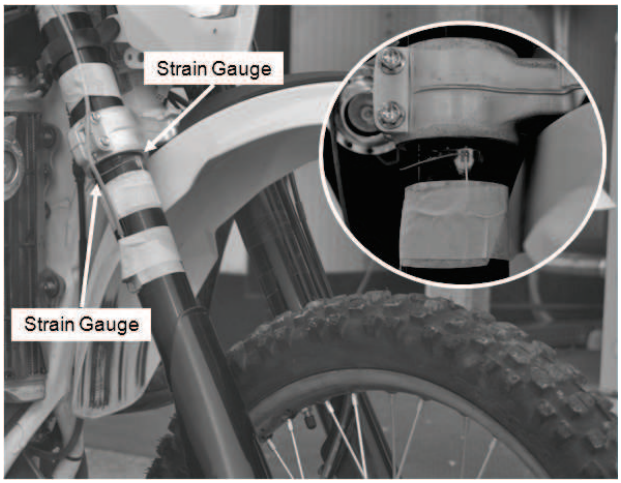

Figure 2.3: Strain gauges installation.

was connected to a NI 9237 C-DAQ module, plugged into a NI C-Rio 9014 real time portable controller. Such a real time portable controller has an an internal processor: the data sampling software runs on that dedicated hardware and the data are stored into the internal memory of the controller. Thanks to that, it was possible to carry out the data acquisition without any interruption, downloading the data to the hard drive of a common notebook at the end of the riding session. The software, written by the author in the Labview language, was used to manage all the data acquisition parameters: the sampling frequency was set at 100Hz. The bridge completion of the Wheatstone circuit is done by means of the C-DAQ module, which is provided with a reconfigurable internal circuit. Then, a professional rider performed a set of typical manoeuvres, including the emergency braking on dry asphalt, the clearing of a step (height 150mm) and a jump from a height of 1m. The stress values were sampled for both the legs and the relevant plots are reported in Figures 2.4, 2.5, 2.6 and 2.7.

The stress peaks, associated with each loading condition are summarized in

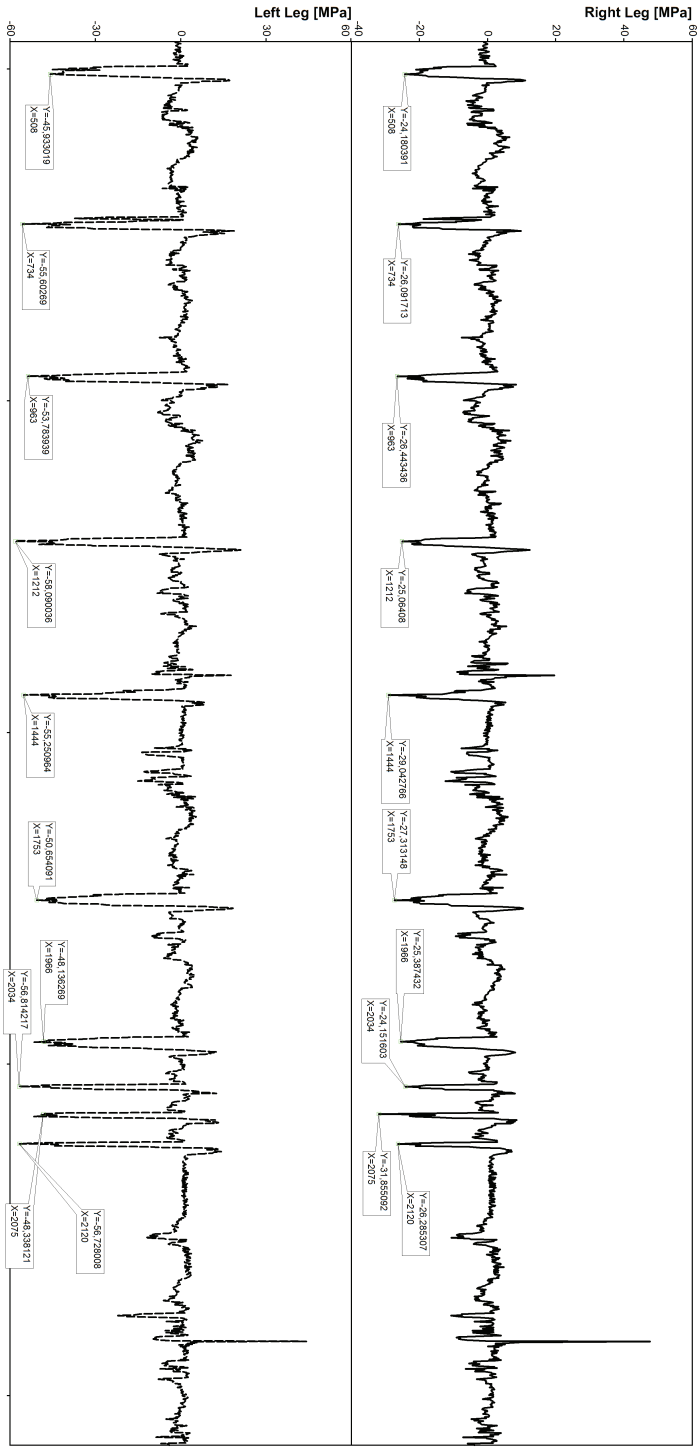

Figure 2.4: Series of ten emergency brakings: bending stress tracks for right leg (solid line) and left leg(dashed line).

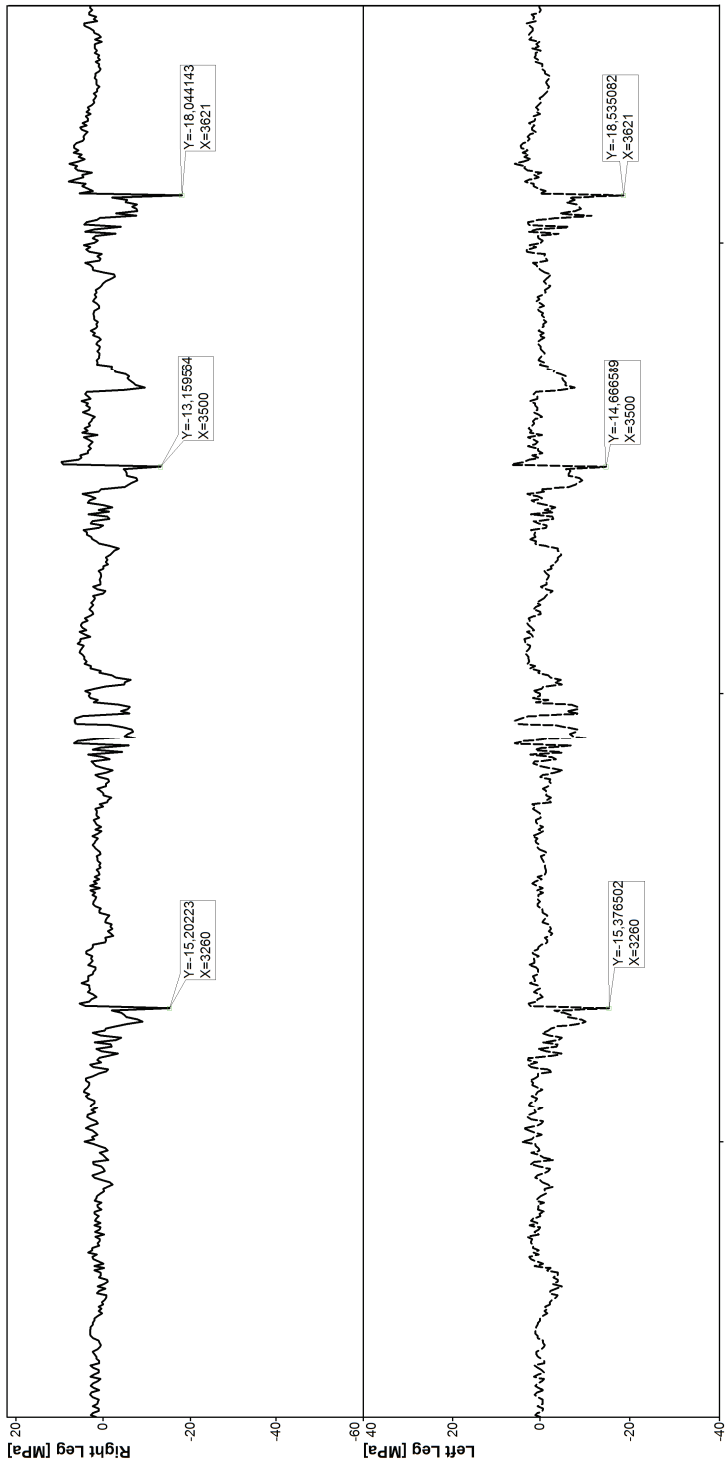

Figure 2.5: Three step clearing manoeuvres: bending stress tracks for right leg (solid line) and left leg(dashed line).

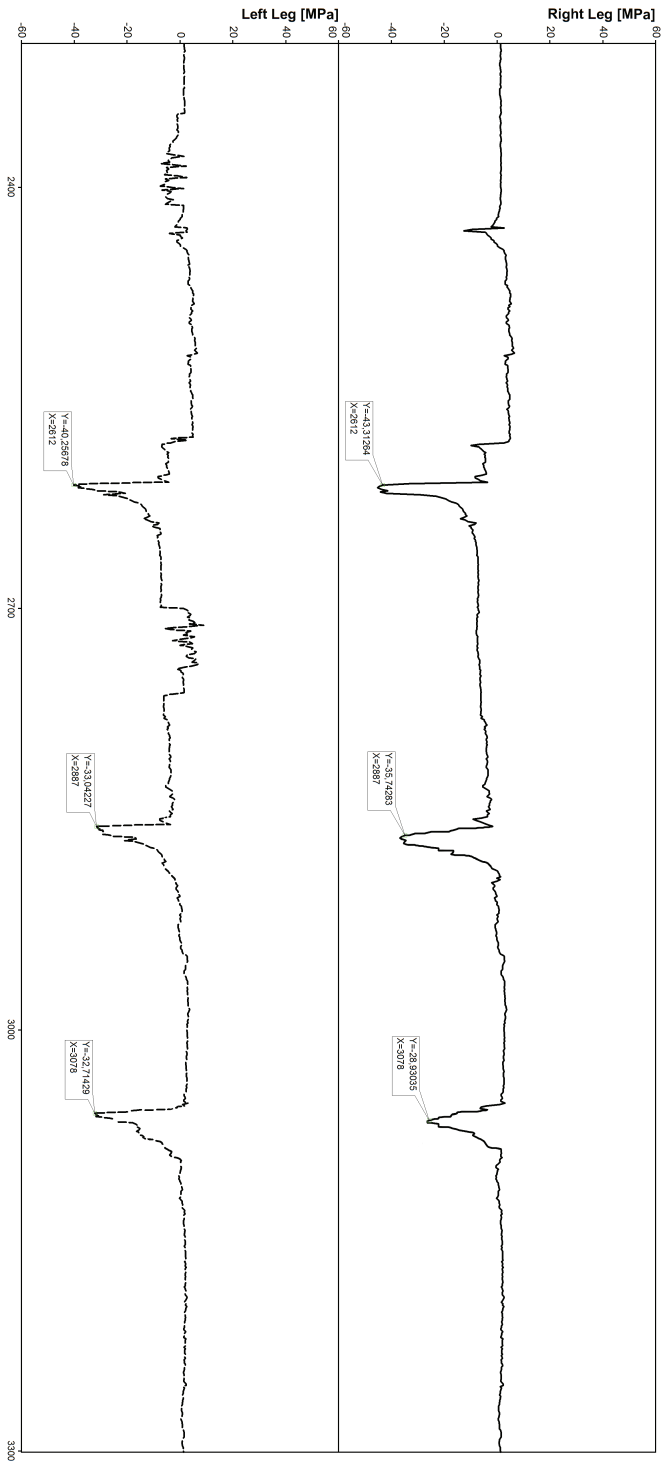

Figure 2.6: Jump: bending stress tracks for right leg (solid line) and left leg(dashed line).

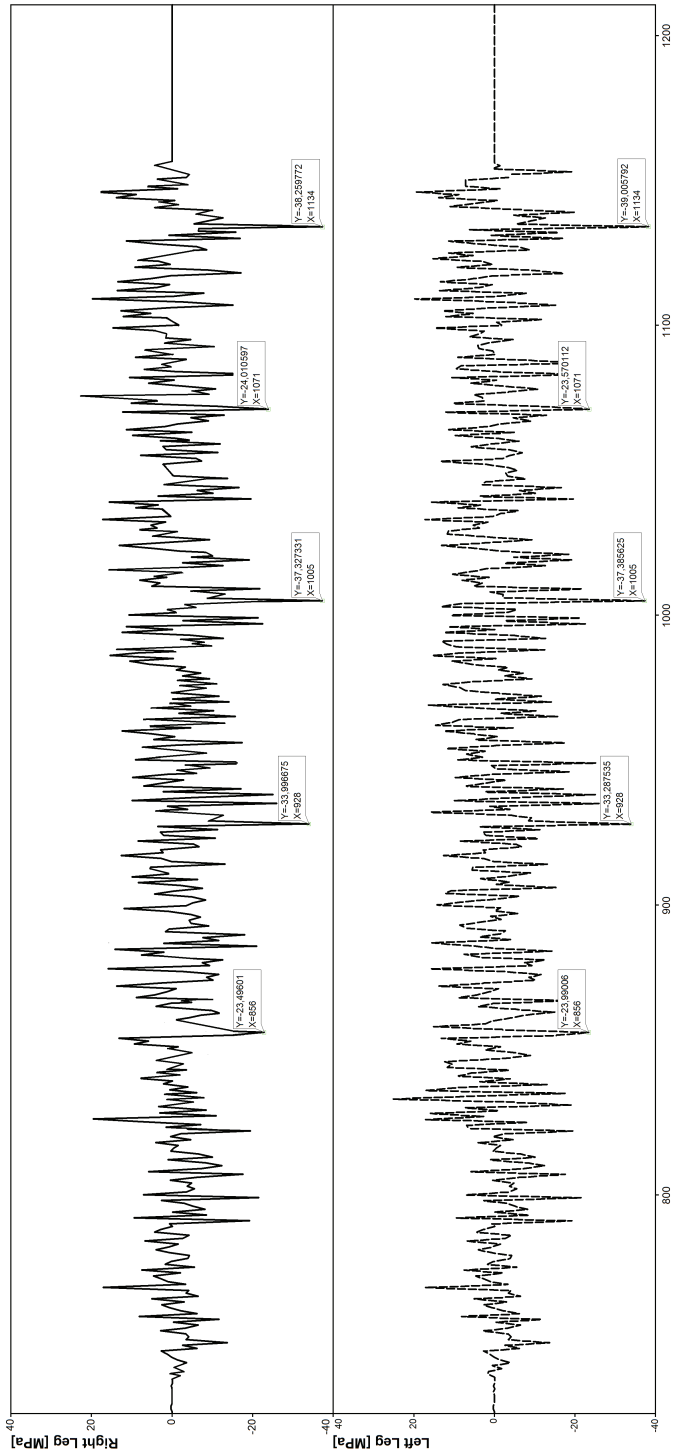

Figure 2.7: Cam drum: bending stress tracks for right leg (solid line) and left leg(dashed line).

Table 2.1: Average values for the maximum bending stresses.

	Emergency braking	Step clearing	Jump	Cam drum
σ_{C_x} $[MPa]$	53	16	35	31
σ_{D_x} $[MPa]$	23	15	36	31

Tab. 2.1; the cam drum column refers to a test bench, which fork producers commonly use as a means for replicating the stresses produced on the fork by a certain road profile. In such a test bench, the whole fork group, along with the wheel rim and the tire, is installed on a fixed support and then a rotating drum, to whose external circumference are applied obstacles of variable shape (cams), is put in contact with the tire. As the drum starts, the fork is subjected to a series of repeated stresses, whose intensity is a function of the obstacles shape and whose frequency is a function of the angular velocity of the drum. Therefore, a run during which the fork is subjected to several kinds of road irregularities is simulated. An attentive examination of Tab. 2.1 reveals that, only during the emergency braking, a considerable stress unbalance between the two legs exists. Since the cross sections of the two legs are identical, also the reaction moments in the vicinity of the joint between fork clamp and stanchions must be different between the two legs. Such a behaviour is peculiar to single disc forks and it is due to their asymmetric architecture: this implies that the dimensioning of the stanchions cross sections cannot be optimized and that, during the braking phase, the motorcycle tends to deviate from the correct trajectory because of the different deformation of the two legs. Since the average values for the peak bending stresses of each loading condition are reported in Tab. 2.1, it is possible to observe that the worst loading condition for the fork stanchions is the emergency braking. Therefore, the analytical model proposed takes into account the sole braking condition.

2.2 Basics of tire dynamics

In the light of the experimental analyses discussed in the previous section, there is evidence that a hard braking manoeuvre, during which the rear tyre looses contact with the ground, and the whole motorcycle weight is transferred to the front wheel, determines the highest bending stress values on the fork legs. In order to build an analytical model useful for the structural design of motorbike forks, such loading condition must be deeply understood and described. For example, the adherence characteristics of the tire-road system, as well as the mass geometry of the motorbike, play a significant role in defining the maximum bending loads due to a hard brake. Tires are flexible elements which provide shock absorption while keeping the wheel in close contact with the ground. Tires grip characteristics have a critical role in defining the overall traction, braking and cornering performance that a motorbike can deliver. Traction and braking forces arise during the ride, involving shear forces along the contact area between the tire and the ground. Such

forces make the rubber fibres of the tire outer circumference compress along the tangential direction during the traction phase and extend during the braking phase. Figure 2.8 shows a tire travelling with a velocity $V_0 = \omega r_0$, subject to a braking torque T_b which determines a braking force F_b at the interface between the tire and the ground. A vertical load N acts on the tire. Due to the longitudinal braking

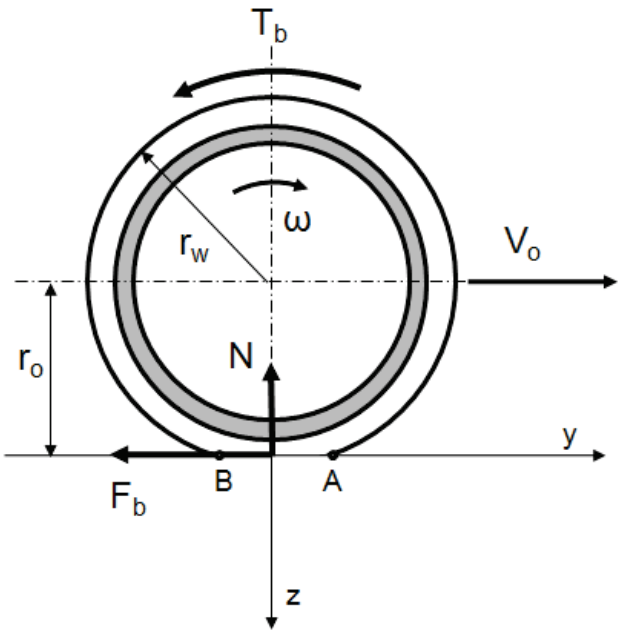

Figure 2.8: Tire subject to a brake.

force F_b, the rubber fibres on the running circumference elongate when passing through the tire-ground contact segment AB (Fig. 2.9). Hence, the circumferential velocity of a point fixed to the aforementioned fibres decreases as it travels from point A to point B: the circumferential velocity V of such a point is therefore lower than the travelling velocity V_0. Now, define the longitudinal slip, k as:

$$k = \frac{V - V_0}{V_0} \tag{2.1}$$

The longitudinal slip takes positive values for traction and negative values for braking. Over the years, tire manufacturers defined a variety of semi-empirical relationships expressing the longitudinal force F (and then the longitudinal friction coefficient $\mu\prime$) as a function of vertical load N and longitudinal slip values k. A widely known relationship of such nature is the so called "magic formula" due to H. B. Pacejka [24], a transcendental function generally expressed in the form:

$$F\langle k\rangle = D \cdot \sin\{C \cdot \arctan\left[B \cdot k - E \cdot (B \cdot k - \arctan(B \cdot k)\right]\} \tag{2.2}$$

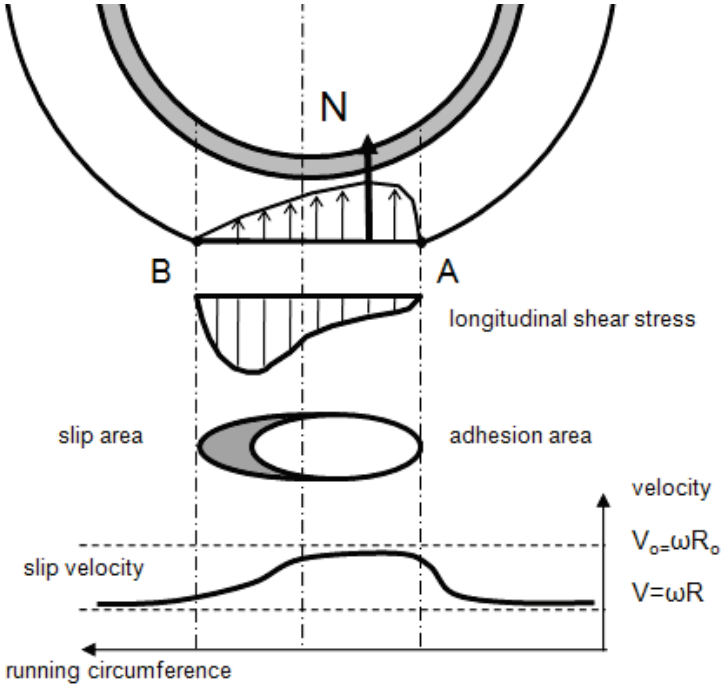

Figure 2.9: Slip velocity during a brake.

And the longitudinal friction coefficient $\mu\prime$:

$$\mu\prime = \frac{F}{N} \tag{2.3}$$

Being F the longitudinal force and k the longitudinal slip. B, C, D, and E are input coefficients which depend on several "static" parameters (tied to the geometrical and chemical characteristics of the tire) and on two "dynamic" parameters, namely the longitudinal slip k and the vertical load N. The "magic formula" 2.2 owes its name to the fact that there is no particular physical basis behind its mathematical form, but it fits a wide variety of tire constructions and operating conditions. The equation can be plotted as shown in Fig. 2.10, where $\mu\prime$ is reported as a function of k. Looking at Fig. 2.10 it could also be noticed that the curve $\mu\prime\langle k\rangle$ is characterized by a peak, which is typically found for values of k around $k = \pm 0.15$.

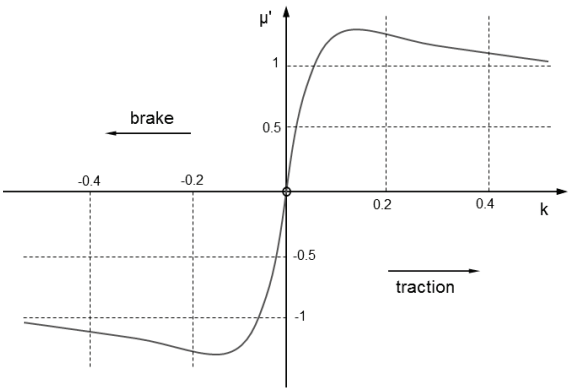

Figure 2.10: Longitudinal friction coefficient μ as a function of the longitudinal slip k.

2.3 The analytical model

Another element which influences the bending stress values on the fork legs is the amount of "diving" that the suspension exhibits under braking (see Introduction). In fact, the forces at the interface between road and tire increase while braking, taking peak values at the end of the brake. On the contrary, the fork length decreases to become minimum when the vehicle comes to a complete stop (it can be easily observed by means of a linear transducer installed on the fork). In order to account for that behaviour, the analytical model shall comprehend a parameter representing the fork length and finite elements analyses shall be carried out with the fork both at the fully extended and at the fully retracted positions. Referring to Fig. 2.11, define:

- m: bike + rider mass [kg];
- p: bike wheelbase [mm];
- b: bike + rider centre of mass to rear wheel axis distance [mm];
- h: bike + rider centre of mass to ground distance [mm];
- $h\prime$: centre of the aerodynamic pressure [mm];
- F_w: aerodynamic force [N];
- F_{bf},F_{br}: front wheel and rear wheel braking forces [N];
- N_f, N_r: weight on the front and on the rear axle [N].

When the motorbike stands on a flat surface, the vertical load acting on the rear wheel is:

$$N_r = m \cdot g \cdot \frac{p-b}{p} \tag{2.4}$$

Define now the amount of load transfer from the rear axle to the front axle as:

$$\triangle N = m \cdot d \cdot \frac{h}{p} \tag{2.5}$$

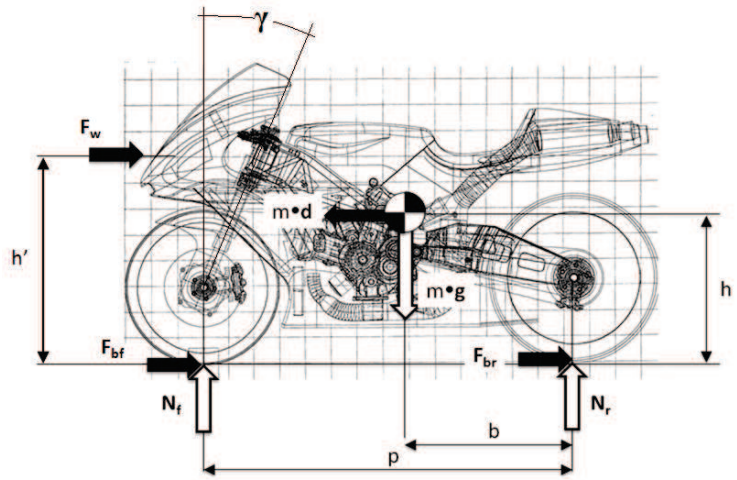

Figure 2.11: Equilibrium of the motorbike during the emergency braking.

When brakes are applied, the vertical loads on each wheel are then:

$$N_r\prime = N_r - m \cdot d \cdot \frac{h}{p} \tag{2.6}$$

$$N_f\prime = m \cdot g - N_r\prime \tag{2.7}$$

The governing relationships for the in-plane equilibrium of the motorbike during braking are:

$$\begin{cases} F_w + F_{bf} + F_{br} = m \cdot d \\ m \cdot d \cdot h = m \cdot g \cdot (p-b) + F_w \cdot h\prime \end{cases} \tag{2.8}$$

Where:

$$\begin{cases} F_{bf} = \mu\prime \cdot N_f\prime \\ F_{br} = \mu\prime \cdot N_r\prime \end{cases} \tag{2.9}$$

Here $\mu\prime$ is the longitudinal friction coefficient, as defined in Eq. 2.3. Therefore, a braking manoeuvre in which the rear tyre looses contact with the ground, and

the entire weight of the motorbike is transferred to the front wheel is characterized by $N_r\prime = 0$ [25] [26] [27]. In that case, 2.8 transforms as follows:

$$\begin{cases} F_{bf} = m \cdot d - F_w \\ m \cdot d \cdot h = m \cdot g \cdot \dfrac{(p-b)}{h} + F_w \cdot \dfrac{(h\prime - h)}{h} \end{cases} \tag{2.10}$$

Then, recalling 2.7 and 2.9 we obtain from 2.14 the maximum applicable braking force:

$$F_{bf\_max} = min\left[\mu\prime \cdot m \cdot g;\ m \cdot g \cdot \frac{(p-b)}{h} + F_w \cdot \frac{(h\prime - h)}{h}\right] \tag{2.11}$$

The first limiting condition is given by the adherence limit of the front tire and the second by the capsizing limit of the motorbike. It is commonly assumed that standard sport-touring tires for motorbikes can deliver a maximum longitudinal friction coefficient $\mu\prime \cong 1.5$ [26], on a dry clean asphalt surface. During a hard braking, a motorbike with comparatively long wheelbase and low center of mass (like, for example a "cruiser" type motorbike) would probably reach the skidding condition before capsizing, while a motorbike of the "hypersports" type would probably do the opposite. The maximum applicable braking force is a key parameter for fork manufacturers: in fact, it is strictly tied to the maximum bending loads the fork legs must withstand according to the product mission [28]. The

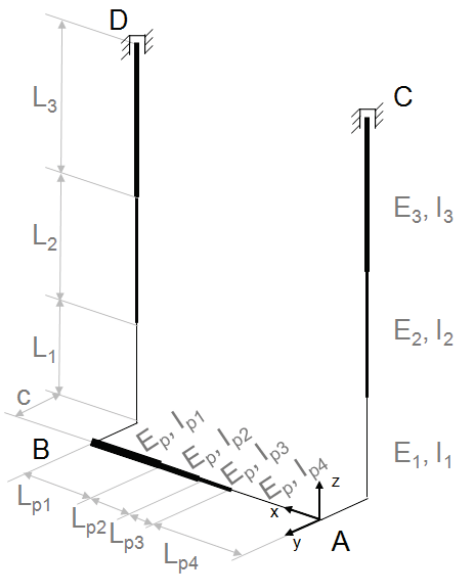

Figure 2.12: Line body scheme of a motorbike fork.

analytical model was developed referring to the line body scheme shown in Fig.

2.12; a portal frame [29] made up of three axisymmetric elements, the two pillars representing the legs and the transverse beam representing the axle. The relevant Cartesian coordinate system is set in accordance with Fig. 2.12. The offset along the y-axis, c, between the wheel axle and the leg axis is reported in Fig. 2.12 as well. The pillars are constrained in C and D by means of two hinges, which allow the sole rotation around the z-axis (as the two bearings, installed between the tube and the stanchion, do in the actual component). The beam and the pillars have material and inertia parameters variable along their axes, in order to achieve a reliable approximation of the mechanical properties of the actual components. Each leg has been subdivided into three segments: E_i and I_i being the Young's moduli and the x-axis moments of inertia of the leg segments, respectively. In order to clarify what was stated above, variable thickness lines represent the different properties of the portal frame elements in Fig. 2.12. This complication is due to the fact that the leg is made up of two elements, the tube and the stanchion, having variable materials and sections along their axes (Fig. 2.13) In order to achieve

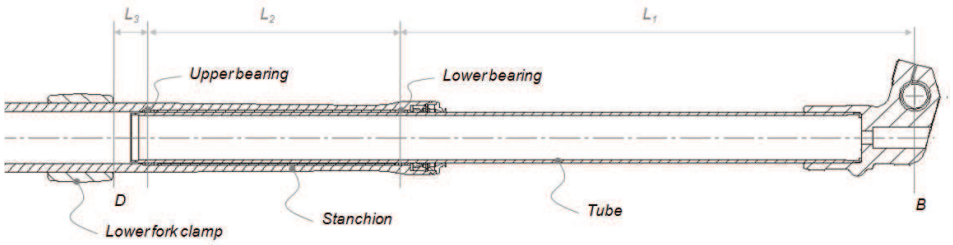

Figure 2.13: Sectional view of a motorbike fork leg.

a correct positioning of the wheel hub and the rolling bearings, the axle has a variable diameter along its symmetry axis; the portal beam was therefore subdivided into four sections with different moments of inertia (I_{pj}, J_{pj}). As shown in Fig. 2.13, the overall free length of the legs ($L = L1 + L2 + L3$) is the distance, measured along the z-axis, from the wheel axle to the lower edge of the lower fork clamp. When the brakes are activated, a load transfer from the rear wheel to the front wheel of the motorbike takes place. The amount of the load transfer depends on the center of mass position, on the motorbike wheelbase and on the deceleration value. Loads on the portal frame are defined as for the iso view of Fig. 2.14: there is represented the portal frame, loaded out of its plane, with all the forces shown in their actual positions. In Fig. 2.14 is reported also a side view of the portal, showing the disc force components along with some useful dimensions. Referring to Fig. 2.14, r_d is the mean disc radius and α the angle between the z-axis and the brake pads centre (brake caliper angle); γ is the caster angle (see also Fig. 2.11) and c is the offset between the axle and the leg axis. N and F_b forces are transmitted to the axle. In order to enforce the internal equilibrium, internal forces arise as well.

Define the braking torque on the disc:

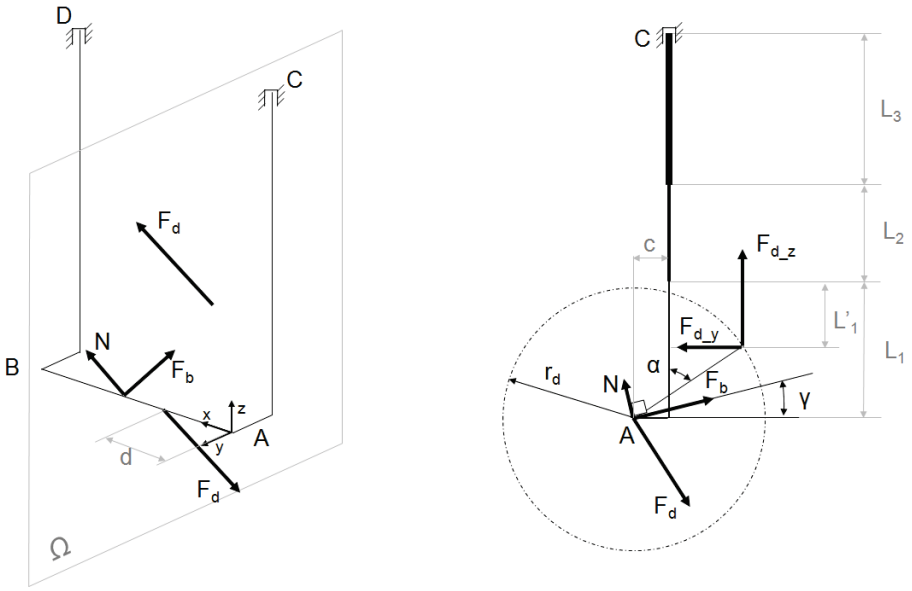

Figure 2.14: Forces (iso view) and force components (side view) on the portal frame.

$$T_b = F_{bf\_max} \cdot r_w \tag{2.12}$$

Where r_w is the front wheel rolling circumference radius. In order to deliver the braking torque T_b, the braking pads must provide a braking force on the disc:

$$F_d = \frac{F_b}{r_d} = F_d \cdot \frac{r_w}{r_d} \tag{2.13}$$

For equilibrium reasons, the same F_d force acts on the disc and on the brake caliper, from which it is transferred to the relevant leg. In order to transfer the F_d force components to the leg axis (refer to the right side of Fig. 2.14), three concentrated moments T_{d_x}, T_{d_y} and T_{d_z} have to be introduced. Referring to the notation in Fig. 2.14, define:

$$\begin{cases} F_{d\_y} = F_d \cdot \cos\alpha \\ F_{d\_z} = F_d \cdot \sin\alpha \end{cases} \tag{2.14}$$

T_{d_x} is due to the y-axis distance between the leg axis and the brake pads centre:

$$T_{d\_x} = F_{d\_z} \cdot (r_d \cdot \sin\alpha - c) \tag{2.15}$$

Whereas T_{d_y} can be written as:

$$T_{d\_y} = F_{d\_z} \cdot d \tag{2.16}$$

T_{d_y} will be neglected because it does not contribute to the legs deflection on yz-plane. Finally T_{d_z} is given by:

$$T_{d\_z} = F_{d\_y} \cdot d \tag{2.17}$$

The distance, measured along z-axis, between the F_d projection on y-axis, F_{d_y}, and the constraint C, is $L\prime = L_1\prime + L_2 + L_3$, where:

$$L_1\prime = L_1 - r_d \cdot \cos\alpha \tag{2.18}$$

In the following, force reactions will be represented by upper case letter R, while external moment reactions by upper case letter M. There are, therefore, six static equations and ten unknown force and moment reactions in C and D, leaving the system statically indeterminate. At the same time, it can be noticed that:

$$M_{C\_z} = M_{C\_z} = 0 \tag{2.19}$$

because the tube and the stanchion are free to rotate with respect to each other. R_{C_z} and R_{D_z} can be neglected because they are transmitted by the fork springs to the fork clamps, without affecting the flexural stress state of the legs. Moreover, the following external reaction components are null due to the loading condition:

$$\begin{cases} R_{C\_x} = R_{D\_x} = 0 \\ M_{C\_y} = M_{D\_y} = 0 \end{cases} \tag{2.20}$$

The structure remains, however, statically indeterminate: the well-known method of consistent deformations [30] can be applied to solve it. The reaction moment values along the x-axis (M_{C_x} and M_{D_x}) are computed. The different intensities of such reaction moments testify that an uneven stress distribution exists between the two legs, due to the loading asymmetry. The rotation angles around the x-axis of points A and B are defined by ϕ_A and ϕ_B respectively. The structure is uncoupled at points A and B and the consistent deformations equation is introduced:

$$\phi_A = \phi_B + \phi\prime \tag{2.21}$$

where $\phi\prime$ is the axle torsion angle between ends A and B. As formerly specified, a number of effects combine to bring about the overall M_{C_x} and M_{D_x} reaction moments; for instance F_b and N determine equal external reaction moments around the x-axis while F_d does not. Relying on the fact that the analysis is carried out in the elastic field, the aforementioned loads can be subdivided into four groups, applied to the structure separately, and eventually superimposed, in order to compute the overall M_{C_x} and M_{D_x} values. The first effect is due to the combined action of the disc force component F_{d_y} and of the concentrated moment T_{d_x}, both applied to the braking leg axis at $z = L_1 - L_1\prime$ (Fig. 2.15).

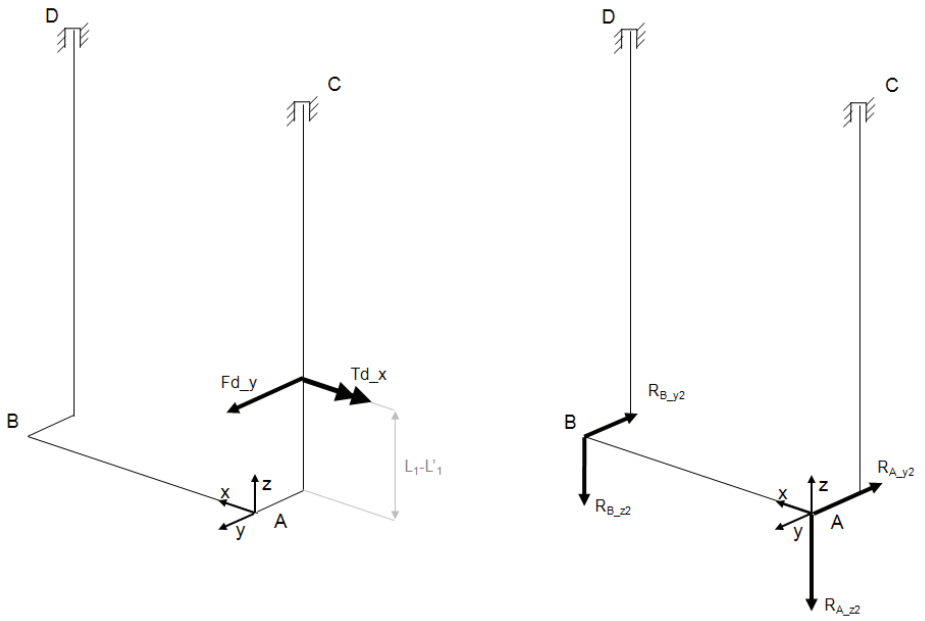

Figure 2.15: Force and torque components on the portal frame: first effect (left) and second effect (right).

In order to provide the expressions of the reaction moments in C and D, it is useful to define the following two groups of parameters:

$$\begin{cases} S_1 = \frac{{L_3}^2}{2 \cdot E_3 \cdot I_3} + \frac{(L_1 + L_2) \cdot L_3}{E_3 \cdot I_3} + \frac{{L_2}^2}{2 \cdot E_2 \cdot I_2} + \frac{L_1 \cdot L_2}{E_2 \cdot I_2} + \frac{{L_1}^2}{2 \cdot E_1 \cdot I_1} \\ S_2 = \frac{L_3}{E_3 \cdot I_3} + \frac{L_2}{E_2 \cdot I_2} + \frac{L_1}{E_1 \cdot I_1} \\ S_3 = \frac{L_p}{G_p \cdot J_p} \end{cases} \tag{2.22}$$

$$\begin{cases} S_{11} = \frac{{L_3}^2}{2 \cdot E_3 \cdot I_3} + \frac{(L_1\prime + L_2) \cdot L_3}{E_3 \cdot I_3} + \frac{{L_2}^2}{2 \cdot E_2 \cdot I_2} + \frac{L_1\prime \cdot L_2}{E_2 \cdot I_2} + \frac{({L_1\prime}^2)}{2 \cdot E_1 \cdot I_1} \\ S_{22} = \frac{L_3}{E_3 \cdot I_3} + \frac{L_2}{E_2 \cdot I_2} + \frac{L_1\prime}{E_1 \cdot I_1} \end{cases} \tag{2.23}$$

Then, the reaction moment due to the first effect in D can be expressed as follows:

$$\begin{cases} M_{D\_x1} = \frac{F_{d\_y} \cdot S_{11} + T_{d\_x} \cdot S_{22}}{2 \cdot S_2 + S_3} \; if \cos\alpha \geqslant 0 \\ M_{D\_x1} = \frac{F_{d\_y} \cdot S_{11} + T_{d\_x} \cdot S_{22} - \left[\frac{F_{d\_y} \cdot (L_1\prime - L_1)^2}{2 \cdot E_1 \cdot I_1} - \frac{T_{d\_x} \cdot (L_1\prime - L_1)}{E_1 \cdot I_1} \right]}{2 \cdot S_2 + S_3} \; if \cos\alpha < 0 \end{cases} \tag{2.24}$$

While the reaction moment in C is given by:

$$M_{C\_x1} = F_{d\_y} \cdot (L_1\prime + L_2 + L_3) + T_{d\_x} - M_{D\_x1} \tag{2.25}$$

F_d acts on the disc as well: then it is transmitted by the hub to the wheel axle and, finally, to the legs at points A and B (Fig. 2.15). The second effect is taken into account by means of the equations below, in which the principle of consistent deformations of Eq. 2.21 is applied again:

$$M_{D\_x2} = \left[\frac{(R_{A\_y2} - R_{B\_y2}) \cdot S_1 + (R_{A\_z2} - R_{B\_z2}) \cdot S_2 \cdot c}{2 \cdot S_2 + S_3}\right] + R_{B\_y2} \cdot (L_1 + L_2 + L_3) + R_{B\_z2} \cdot c \tag{2.26}$$

$$M_{C\_x2} = -\left[\frac{(R_{A\_y2} - R_{B\_y2}) \cdot S_1 + (R_{A\_z2} - R_{B\_z2}) \cdot S_2 \cdot c}{2 \cdot S_2 + S_3}\right] + R_{A\_y2} \cdot (L_1 + L_2 + L_3) + R_{A\_z2} \cdot c \tag{2.27}$$

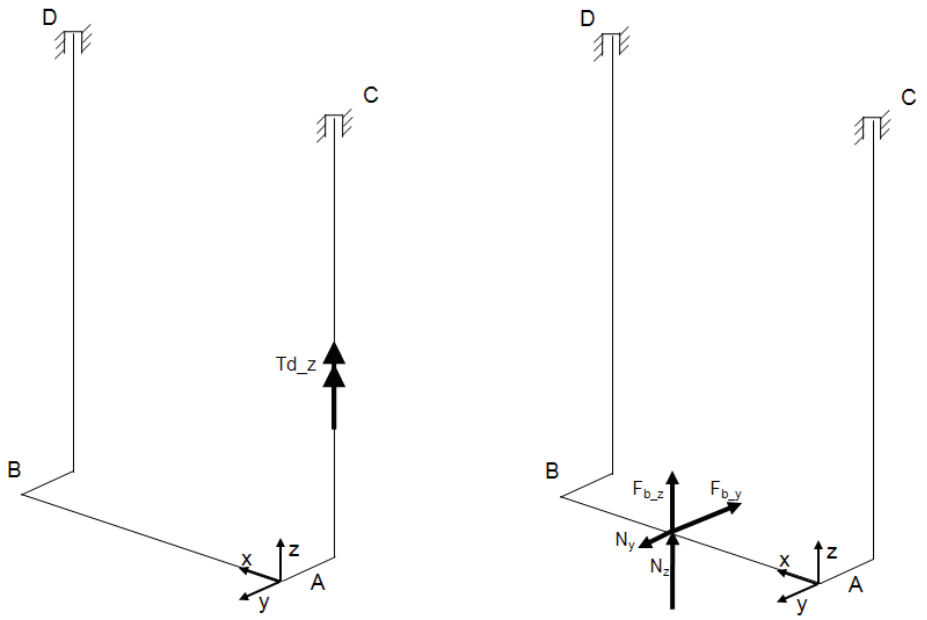

Figure 2.16: Force and torque components on the portal frame: third effect (left) and fourth effect (right).

R_{A_y2}, R_{A_z2}, R_{B_y2} and R_{B_z2} forces can be computed by solving the equilibrium of the wheel axle (treated as a beam, simply supported at its ends A and B) subjected to F_d, applied at a distance d from A (Fig. 2.14). Looking at Fig. 2.16 T_{d_z} torque brings about the last contribution to the overall x-axis moment reactions in C and D, due to the disc force. Since the legs are allowed to rotate along the z-axis, they behave as simple supports for the wheel axle on the xy-plane.

Hence, the concentrated torque can be considered as it was applied to the axle centre: the axle is treated, again, as a simply supported beam, now loaded by T_{d_z} (Fig. 2.17).

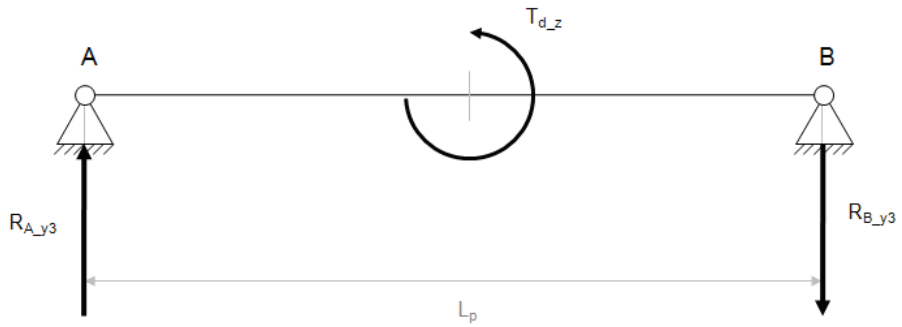

Figure 2.17: T_{d_z} torque applied to the front wheel axle: third effect.

The moment reactions in C and D due to the third effect can be written as:

$$M_{D\_x3} = \left[\frac{(R_{A\_y3} - R_{B\_y3}) \cdot S_1}{2 \cdot S_2 + S_3}\right] + R_{B\_y3} \cdot (L_1 + L_2 + L_3) \tag{2.28}$$

$$M_{C\_x3} = -M_{D\_x3} \tag{2.29}$$

Since the effects which determine the load unevenness between the legs have been examined, focus now on forces F_b and N (Fig. 2.16). Their effects are equally subdivided between the legs. Then, the moment reactions in C and D due to the vertical load N are defined as:

$$M_{C\_x41} = M_{D\_x41} = \frac{N}{2} \cdot [(L_1 + L_2 + L_3) \cdot \sin\gamma - c \cdot \cos\gamma] \tag{2.30}$$

While the moment reactions belonging to F_b are:

$$M_{C\_x42} = M_{D\_x42} = \frac{F_b}{2} \cdot [(L_1 + L_2 + L_3) \cdot \cos\gamma - c \cdot \sin\gamma] \tag{2.31}$$

Then, the contribution of the centered loads is:

$$\begin{cases} M_{C\_x4} = M_{C\_x41} + M_{C\_x42} \\ M_{D\_x4} = M_{D\_x41} + M_{D\_x42} \end{cases} \tag{2.32}$$

Superimposing the effects obtained in Equations 2.25, 2.27, 2.29 and 2.32, the overall reaction moments are expressed in the following Equation 2.33:

$$\begin{cases} M_{C\_x} = M_{C\_x1} + M_{C\_x2} + M_{C\_x3} + M_{C\_x4} \\ M_{D\_x} = M_{D\_x1} + M_{D\_x2} + M_{D\_x3} + M_{D\_x4} \end{cases} \tag{2.33}$$

Where the most important contribution to the overall moment reactions is given by the fourth effect.

2.4 Numerical validation of the analytical model

Once the formulae providing 2.33 are known, the stress values along the fork legs, or the moment reactions of the constraints C and D can be back-calculated. A comparison with the results given by Finite Elements Analyses (FEA) of two different fork geometries is provided, in order to validate the analytical model. The analyses were performed with the forks both in the extended and in the retracted configurations. If they were set up correctly, both the analytical model and the Finite Elements model, in the fully retracted configuration, should return the same z-axis normal stresses found on the outer tubes during the experimental tests.

Table 2.2: Fork1 parameters.

Parameter	Value	Unit
γ	26	deg
α	85	deg
c	34	mm
d	37	mm
$L_{1\_extended}$	397	mm
$L_{2\_extended}$	211	mm
$L_{3\_extended}$	24	mm
$L_{1\_retracted}$	137	mm
$L_{2\_retracted}$	211	mm
$L_{3\_retracted}$	24	mm
L_p	190	mm
I_1	56,261	mm^4
I_2	378,861	mm^4
I_3	322,600	mm^4
J_p	19,769	mm^4
E_1,E_p	206,000	MPa
E_3	71,000	MPa

The first geometry examined is shown in Fig. 2.1 (Fork1). It is an upside-down fork, which means that the outer tubes are joined with the steering plates, while the inner tubes are joined to the axle by means of axle brackets. This fork carries a single brake caliper and it is conceived to suit small-medium "Enduro" motorbikes (125cc - 250cc). All the Fork1 data are reported in Table 2.2. These data are used as inputs for the analytical model. Table 2.3 reports the data of the motorbike in which Fork1 was installed for experimental testing: these data are used to determine the force inputs for both the analytical and the numerical models.

Table 2.3: "Enduro" bike parameters.

Parameter	Value	Unit
m	195	kg
p	1,475	mm
b	650	mm
h	650	mm
r_w	300	mm
r_d	117.5	mm
F_b	2,104	N

FEA analyses were performed with the Ansys code, release 12.0: the model was meshed with tetrahedrons (Fig. 2.18) setting an element size of 3mm for the tubes and the axle, and an element size of 4mm for the stanchions, resulting into approximately 500,000 nodes. In order to implement finite elements analyses for both the extended and the retracted configurations, the pre-processing phase included developing two different CAD assemblies, one for each fork geometry. Then, F_d, N and F_b forces were applied to the structure conveniently, as shown in Fig. 2.19.

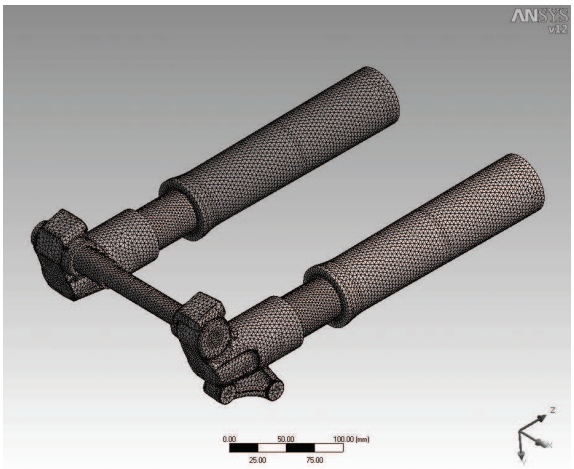

Figure 2.18: Mesh for Fork1 (shown retracted).

Two cylindrical supports, allowing the tubes to rotate around the z-axis, were applied, in C and D, to the stanchions (Fig. 2.19, left). F_d, the force acting on the axle, was subdivided into two components, which were each applied to a restricted surface of the axle corresponding to the contact area between the axle and the wheel bearing internal ring. Since all the geometries examined come from CAD

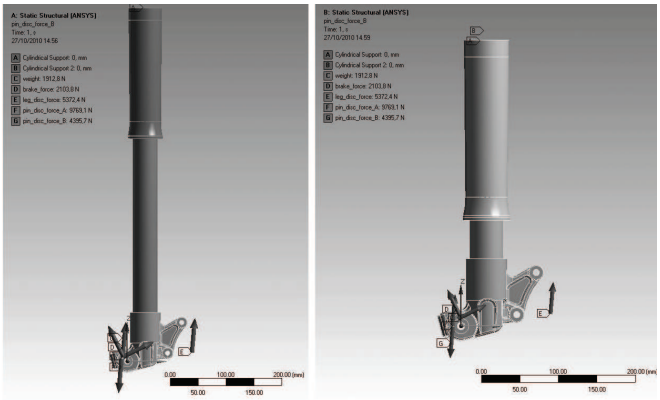

Figure 2.19: Fork1 FEA loads (a) extended, (b) retracted.

assemblies, contacts between the parts needed to be defined. Such contacts were modelled as pure penalty, surface to surface, bonded. For the sake of realizing a model representing the overall structural behaviour of the fork, these contact setting is considered to be correct; moreover, it promotes convergence. In the light of that, the structure is considered as a single body and the results of the FEA can be compared directly with those provided by the analytical model. Such comparison is done for moment reactions in C and D, and reported in Tab. 2.4, which suggests a satisfactory accordance between the two methods.

Table 2.4: Moment reactions for Fork1 - analytical versus FEA.

	FEA			Analytical				
	M_{C_x} (Nm)	M_{D_x}(Nm)	M_{C_x}+M_{D_x}(Nm)	M_{C_x}	ϵ(%)	M_{D_x}	ϵ(%)	M_{C_x}+M_{D_x}
Extended	769 (64%)	436 (36%)	1205 (100%)	772 (64%)	+0.4	435 (36%)	-0.2	1207 (100%)
Retracted	681(73%)	253 (27%)	934 (100%)	683 (73%)	+0.3	250 (27%)	-1.2	933 (100%)

Tab. 2.4 shows that the braking leg always bears most of the total bending load; from 64 per cent (when the fork is extended) to 72 per cent (when the fork is retracted). In order to compare both the analytical model and FEA with experimental analyses (emergency braking column in Tab. 2.1), results in terms of normal stresses were evaluated and reported in Tab. 2.5. In the analytical model, such values can be computed easily 2.34, once the overall reaction moments for the retracted configuration are known :

$$\begin{cases} \sigma_{C\_z} = \frac{M_{C\_x} \cdot D_{e\_3}}{2 \cdot I_3} \\ \sigma_{D\_z} = \frac{M_{D\_x} \cdot D_{e\_3}}{2 \cdot I_3} \end{cases} \tag{2.34}$$

It was examined a second fork model (Fork2); it is a standard fork, to be installed on "Trials" motorbikes up to 250cm^3. All the Fork2 data are reported in

Table 2.5: The z-axis normal stress values for Fork1 (retracted): analytical and FEA versus experimental.

Experimental		FEA				Analytical			
σ_{C_x} (MPa)	σ_{D_x} (MPa)	σ_{C_x} (MPa)	ϵ(%)	σ_{D_x} (MPa)	ϵ(%)	σ_{C_x} (MPa)	ϵ(%)	σ_{D_x} (MPa)	ϵ(%)
53	23	57	+7.5	21	-8.7	59	+11.3	22	-4.3

Tab. 2.6; these data are used as inputs for the analytical model. Tab. 2.7 reports the data of the motorbike for which Fork2 is designed.

Table 2.6: Fork2 parameters.

Parameter	Value	Unit
γ	22	deg
α	338	deg
c	29	mm
d	48	mm
$L_{1\_extended}$	213.5	mm
$L_{2\_extended}$	127	mm
$L_{3\_extended}$	228.7	mm
$L_{1\_retracted}$	31.5	mm
$L_{2\_retracted}$	309	mm
$L_{3\_retracted}$	46.7	mm
L_p	95	mm
I_1	135,157	mm^4
I_2	171,609	mm^4
I_3	36,452	mm^4
J_p	26,034	mm^4
E_1	71,000	MPa
E_3,E_p	206,000	MPa

The main differences between Fork1 and Fork2 can be summarized in: (i) Fork2 is a standard fork, in which the tubes are joined with the fork clamp and (ii) in the case of Fork2, the brake caliper is placed on the front side of the leg (Fig. 2.20). Such a peculiar placement of the brake caliper is quite common in "Trials" motorbikes, because it offers a superior protection to the caliper when the vehicle travels over rugged roads (which often means rocky and steep mountain tracks). In this case, no experimental data are available, so the comparison is presented between analytical and FEA results only, both in terms of moment reactions and normal stresses. The FEA were carried out both on the extended and retracted configurations, with the same settings described above for Fork1: the mesh obtained is shown in Fig. 2.20.

The FEA were carried out both on the extended and retracted configurations, with the same settings described above for Fork1. Two cylindrical supports, al-

Table 2.7: "Trials" bike parameters.

Parameter	Value	Unit
m	152	kg
p	1,305	mm
b	500	mm
h	750	mm
r_w	347	mm
r_d	82.5	mm
F_b	1,600	N

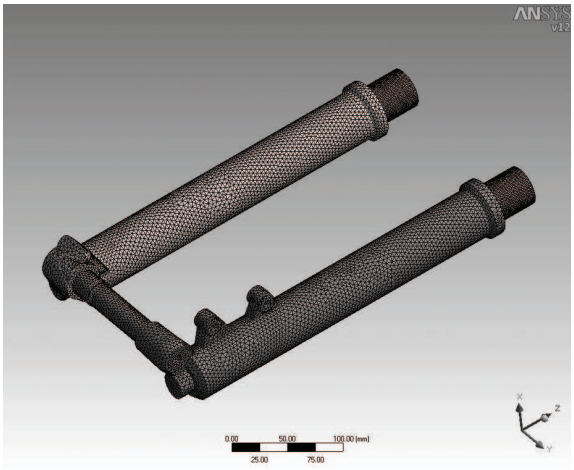

Figure 2.20: Mesh for Fork2 (shown retracted).

lowing the tubes to rotate around the z-axis, were applied in C and D: since we are dealing now with a standard fork, the constraints shall be applied to the tubes and not to the stanchions. Results obtained for moment reactions in C and D are compared, in Tab. 2.8, with those given by the analytical model. Attentive examination of such results confirms the validity of the analytical model and that, again, the braking leg bears most of the total bending load; from 59 per cent (when the fork is extended) to 67 per cent (when the fork is retracted). Errors are slightly higher than those observed for Fork1, but they can be still considered acceptable ($\epsilon\% \leq 10.2$).

Since no experimental data are available for Fork2, a comparison between the FEA and analytical results in terms of normal stresses is reported in Tab. 2.9. As for Fork1, such values can be computed by means of the analytical model, applying equation 2.34.

Looking at Tab. 2.9, the accuracy of the analytical model can still be considered

Table 2.8: Moment reactions for Fork2: analytical versus FEA.

	FEA			Analytical				
	M_{C_x} (Nm)	M_{D_x}(Nm)	M_{C_x}+M_{D_x}(Nm)	M_{C_x}	ϵ(%)	M_{D_x}	ϵ(%)	M_{C_x}+M_{D_x}
Extended	598 (59%)	421 (41%)	1019 (100%)	619 (60%)	+3.5	406 (40%)	-3.6	1025 (100%)
Retracted	569 (67%)	283 (33%)	852 (100%)	602 (73%)	+5.8	254 (30%)	-10.2	856 (100%)

Table 2.9: The z-axis normal stress values for Fork2 (retracted): analytical versus FEA.

Experimental		Analytical			
σ_{C_x} (MPa)	σ_{D_x} (MPa)	σ_{C_x} (MPa)	ϵ(%)	σ_{D_x} (MPa)	ϵ(%)
311	150	314	+1.0	132	-12.0

satisfactory. Fig. 2.21 is referred to one finite element analysis done on Fork2: the scale contours and the flags show normal stresses along the z-axis on both the legs, with the fork in the retracted configuration. As a general statement, the analytical model tends to slightly overestimate the loads on the braking leg while it underestimates the loads on the non braking leg. In this case, dealing with the z-axis normal stresses, values obtained in the vicinity of the constraints show much higher stresses with respect to Fork1: such behavior is acceptable because the tubes are realized in 39 NiCrMo3 steel ($S_Y \cong 680$MPa), while the stanchions are built in EN AW-6082-T6 aluminium alloy ($S_Y \cong 310$MPa).

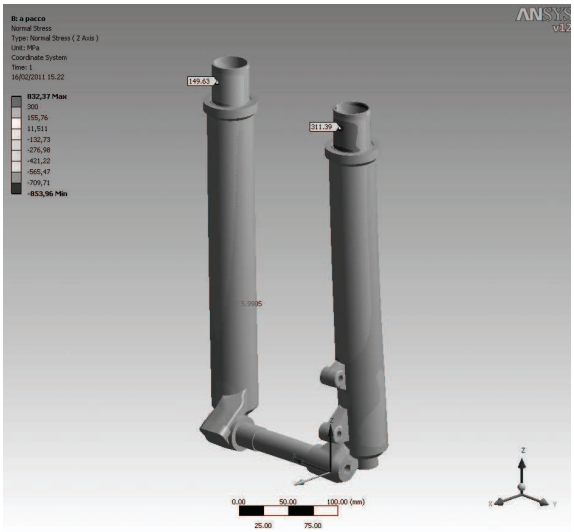

Figure 2.21: Fork2 (retracted) FEA z-axis normal stress values.

2.5 Structural optimization of single disc forks

Tests made on different geometries returned similar results, showing differences between analytical and FEA stress distributions within a few percentage points. Where experimental analyses could be performed (Fork1), the results in terms of normal stress along the z-axis confirmed those given by the analytical model. Moreover, the newly developed analytical method allows fork designers to estimate the impact on the fork stress state of any design change upfront. The imbalanced loads during braking, characteristic of single disc forks, are an undesired effect, which yields different deformations of the legs and therefore a rotation of the axle around the z-axis (see Fig. 2.22). Such a rotation introduces an undesired steering action to the front wheel: hence, the motorbike tends to deviate from the correct trajectory while braking.

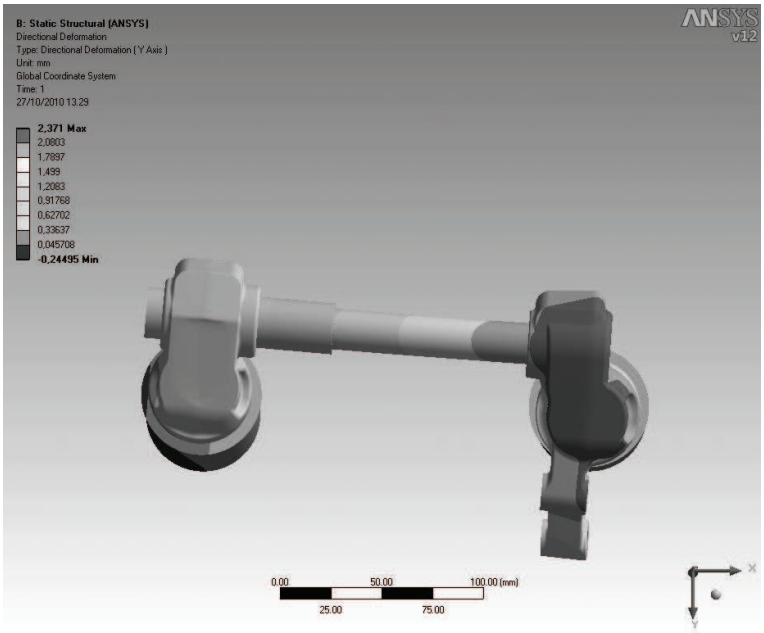

Figure 2.22: Fork1 (bottom view): wheel axle undesired rotation along z-axis, due to loads unbalance.

Thanks to the newly developed analytical model, overall moment reactions in C and D (or the relevant stress values) can be plotted as functions of a key design parameter of the fork. Therefore, design actions can be taken in order to minimize the load unbalance. Some screening tests were made in order to highlight which geometrical parameters affect the load unbalance significantly. In particular, the

effects of axle offset c, disc offset d, moment of inertia of the axle I_p, and brake caliper angle α were examined. The moment of inertia of the axle I_p and brake caliper angle α were demonstrated to be the most influential factors. Moreover, the choice of the axle offset c and the disc offset d is often restricted by vehicle dynamics considerations and by characteristic dimensions of the brake caliper. In fact, it is very uncommon that a motorbike forks producer is also a braking systems producer. Then, brake calipers and discs are most often bought from original equipment manufacturers, who hold the design control over the characteristic dimensions of these products. In order to evaluate the influence of the moment of inertia of the axle I_p and brake caliper angle α, the moment reactions for both the legs are plotted in Figs 10 and 11 for Fork1 (extended and retracted, respectively) and in Figs 12 and 13 for Fork2 (extended and retracted, respectively) as functions of the brake caliper angle α. Dashed lines refer to a fork equipped with a standard axle whereas thick lines refer to the same fork equipped with a stiffer axle (moment of inertia ten times greater). Grey shaded areas in Figs 10 to 13 indicate the ranges of acceptable values of α for each geometry. Such ranges are determined by manufacturability requirements as well as by product performance requirements. It should be appreciated that an even load distribution between the legs can never be reached, whatever the angular position of the brake caliper is (the curves never intersect). Moreover, the braking leg always bears higher loads than the non braking one. Nevertheless, the unbalance can be minimized by choosing $\alpha = 90\,\text{deg}$ and increasing the stiffness of the axle. Such a behaviour can be understood by looking at Eq. 2.13, in which F_{d_y} becomes null for $\alpha = 90\,\text{deg}$, and therefore T_{d_z} (Eq. 2.17) becomes null. In fact, the effect of T_{d_z} on the moment reactions is always equal in magnitude but with opposite directions on the two legs; when such an effect is null, the unbalance decreases. The effect of a stiffened axle is that of reducing the unbalance by transferring more load from the braking to the non braking leg. The aforementioned strategies for reducing the unbalance have similar effects whether the fork be examined in the extended or in the retracted configuration; such an aspect can be appreciated by comparing, for example, Figs. 2.23 and 2.24. As shown by the same figures, the brake caliper placement in Fork1 was chosen quite well ($\alpha = 85\,\text{deg}$; see Tab. 2.2). Conversely, for Fork2 ($\alpha = 338\,\text{deg}$; see Tab. 2.6) a placement around the optimized value of $\alpha = 90\,\text{deg}$ was not permitted (see the shaded areas in Figs. 2.25 and 2.26), because of the product requirements said above. In fact, "Trials" motorbikes are subject to an extreme off-road use, and the brake caliper, as well as other components, must be placed as far as possible from the ground. To summarize, from a structural standpoint, the emergency braking was found to be the most severe loading case for the bending stresses on the legs of motorbike forks. The novel analytical model here above described, allows calculations to be made of the stress field on the legs while braking, given a few geometric parameters of the motorbike and of the fork. The analytical model accounts for the unequal stress distribution on the two legs that arises from the geometrical asymmetry of single disc architectures. The model accuracy can be considered satisfactory, and was tested by comparison with the FEA and (if available) experimental stress analyses. The possibility of balancing the loads on the legs of single disc forks was examined as well.

The brake caliper angle α and the axle stiffness are demonstrated to be the most influential parameters with respect to load distribution between the legs. Since an even load distribution between the legs cannot be achieved, some structural optimization strategies, targeted towards a significant reduction of the unbalance, are herein proposed. In the following chapter, it will be examined the stress state of the leg in the vicinity of the lower fork clamp, taking into account both the dynamic loads due to braking and the static loads due to the characteristics of the joint between the two parts.

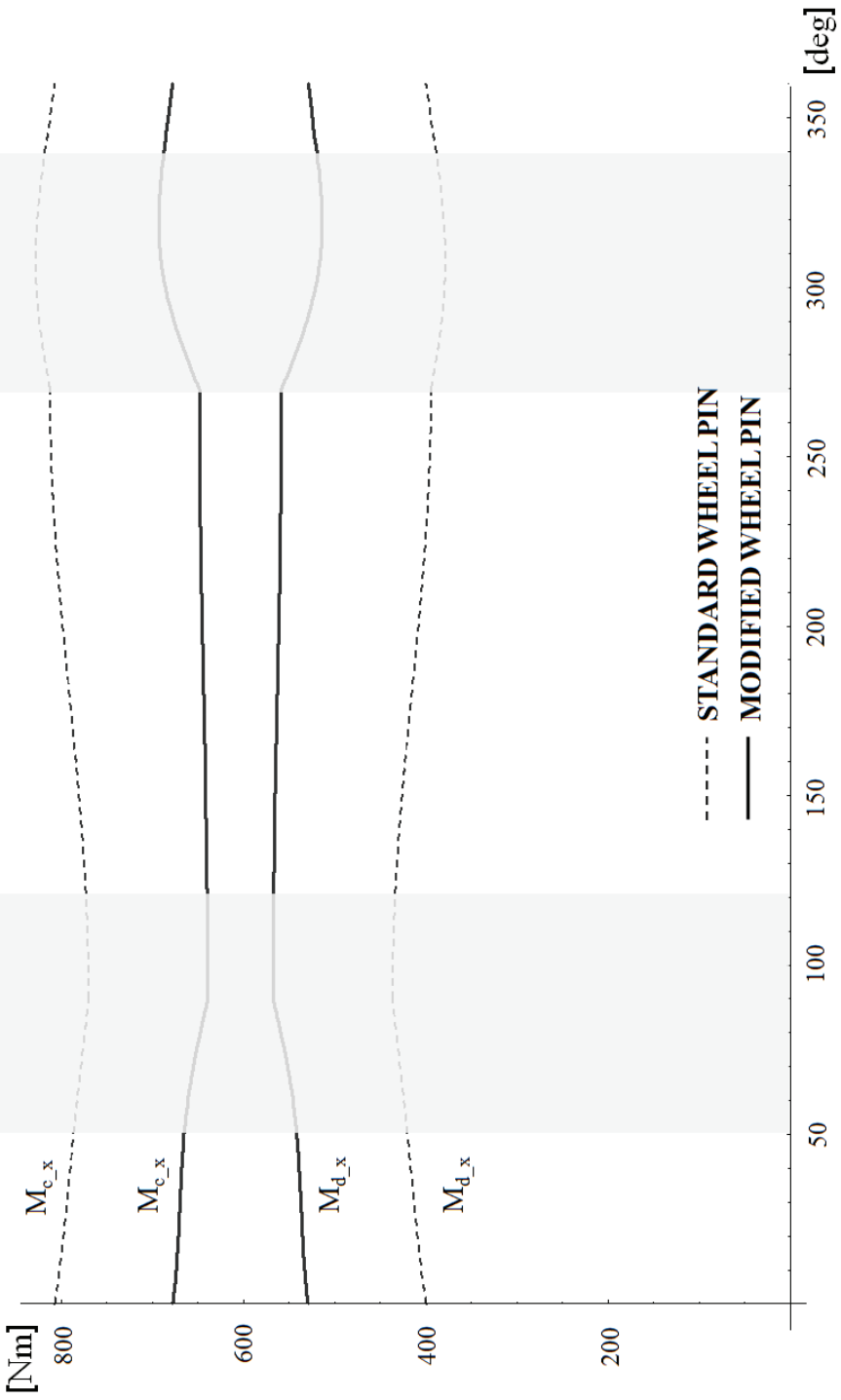

Figure 2.23: Fork1 (extended) moment reactions as functions of α.

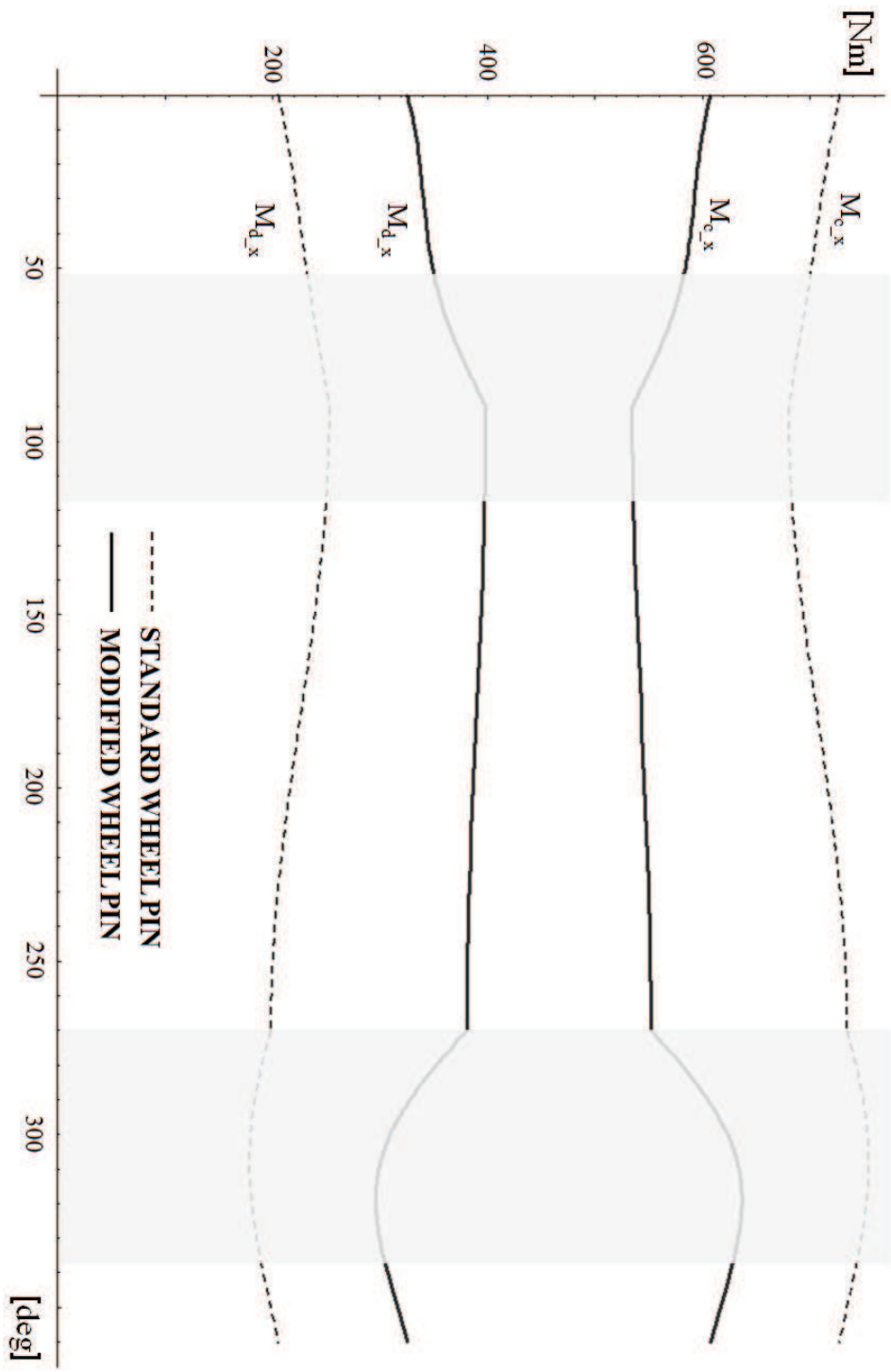

Figure 2.24: Fork1 (retracted) moment reactions as functions of α.

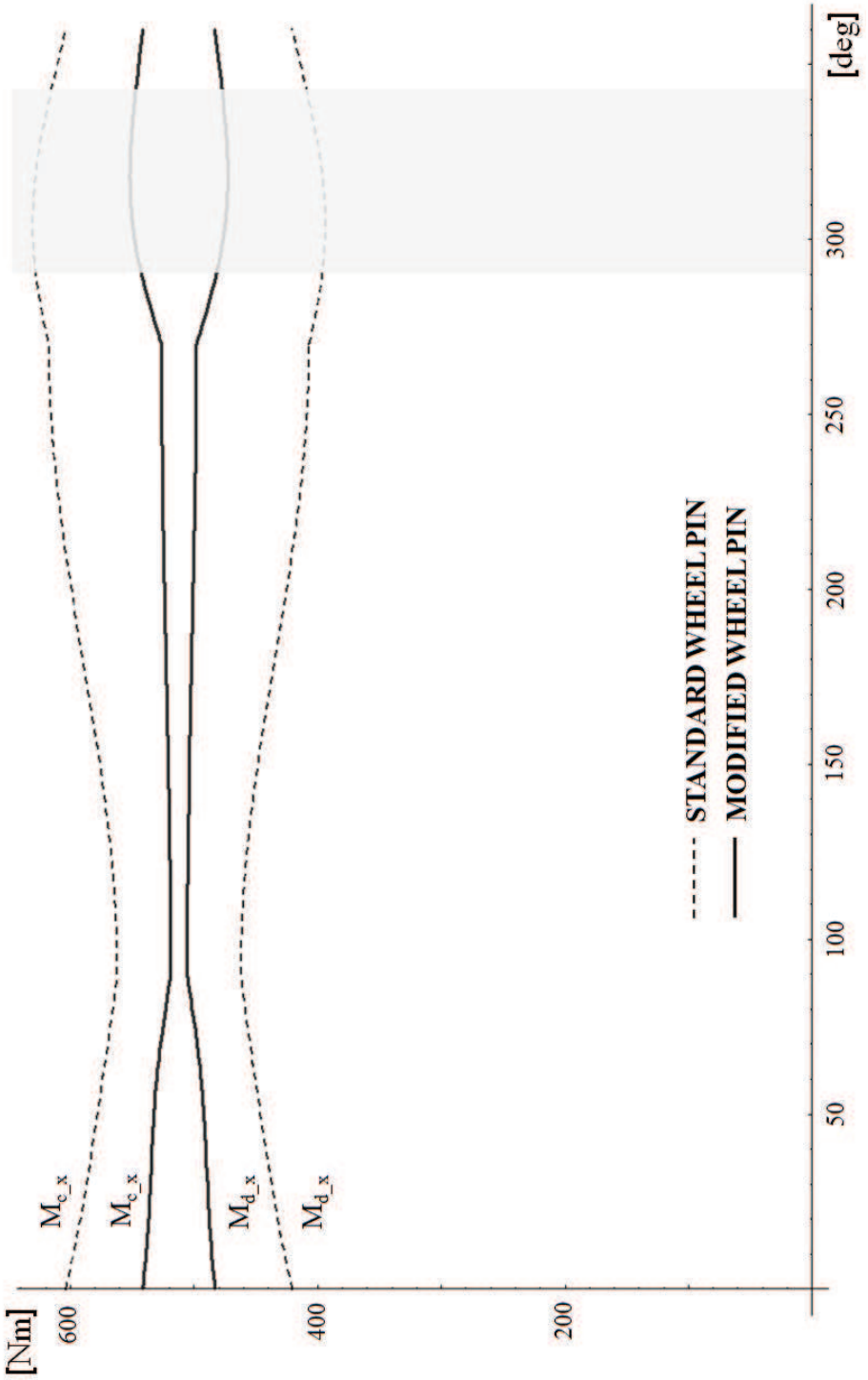

Figure 2.25: Fork2 (extended) moment reactions as functions of α.

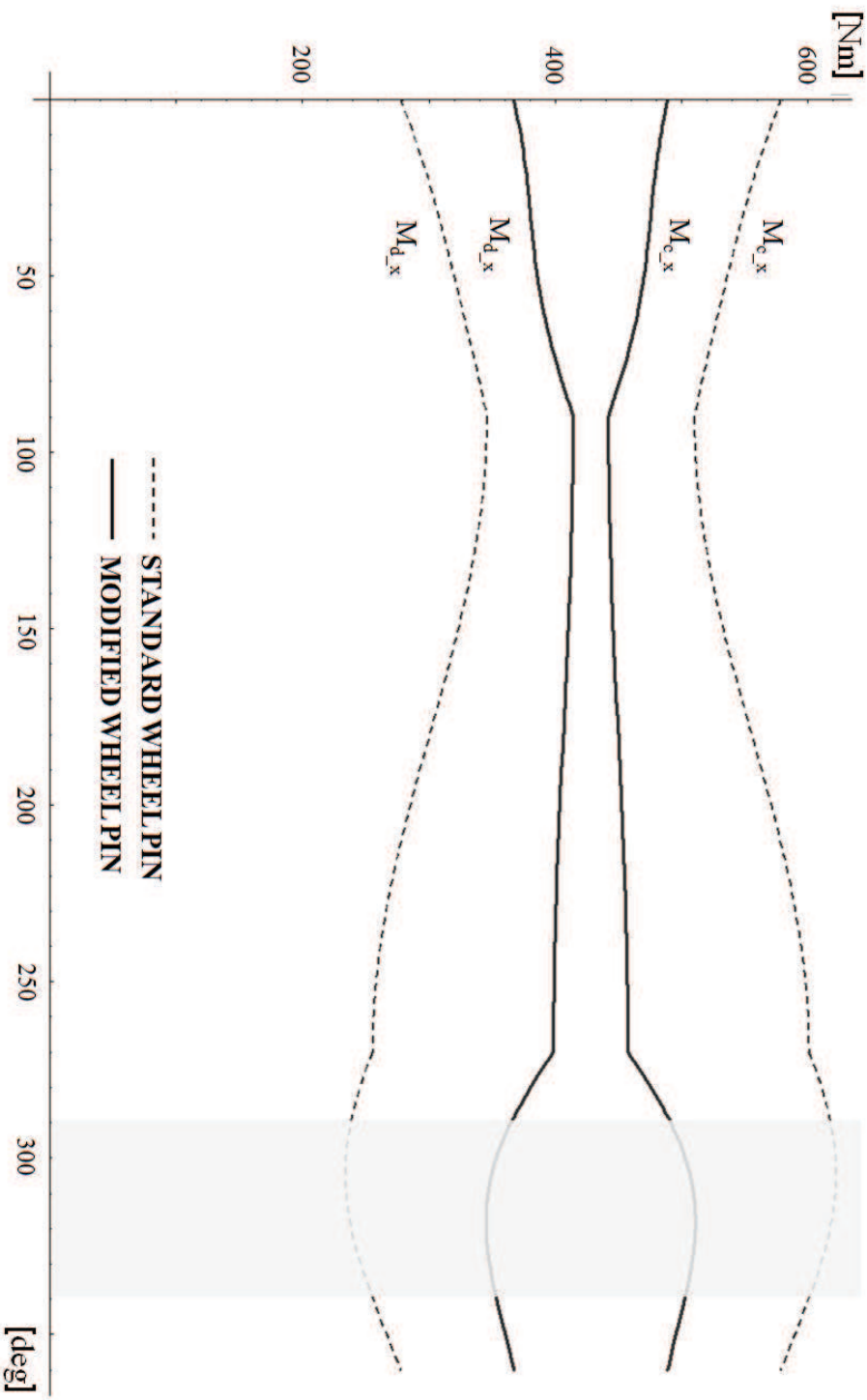

Figure 2.26: Fork2 (retracted) moment reactions as functions of α.

Chapter 3

Stress analysis of shaft-hub joints in motorbike forks

3.1 Field failures

The most part of structural failures recorded in the field for motorbike forks, can be ascribed to bending loads on the legs. These can be either static failures or fatigue failures. In the first case, failures are basically due to overloading of the legs with respect to the design specification. They are characterized by a certain amount of yielding, associated with a residual deformation of the tube or the stanchion. These failures can be associated with incorrect use of the vehicle, or, rarely, with major design flaws. In any case, such a failure mode is seldom identified as the root cause of severe rider's injuries. In the second case, as always happens when fatigue failures are involved, the fork will suddenly lose its load bearing capability, and the consequences can be much more severe.

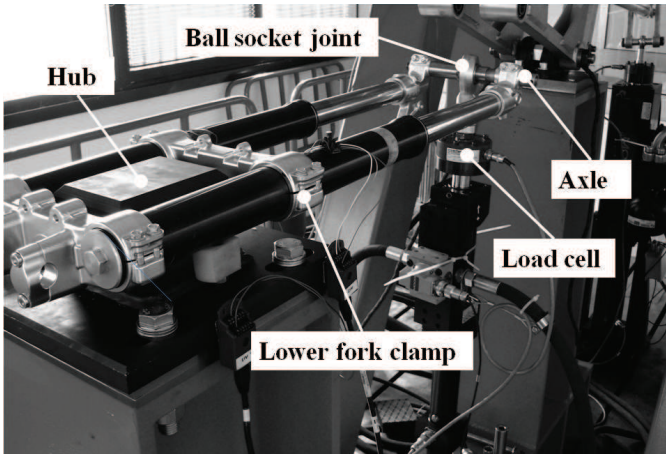

Figure 3.1: Bending fatigue test bench for motorbike forks.

At the beginning of this Ph.D. work, our research team, in collaboration with

Paioli Meccanica S.p.A., developed a test bench for evaluating the fatigue behaviour of motorbike forks under cyclic bending loads (Fig. 3.1). It comprises a fixed support, rigidly connected with the ground. On top of the support there is an adaptable hub which allows to secure the steering pin, locking the fork in the horizontal position. It is provided a force controlled hydraulic cylinder, whose shaft ends with a 10kN load cell, connected to the wheel axle by means of a ball and socket joint. With this layout, the bending loads are always centered, therefore no unbalance between the bending stresses of the two legs exists. It must be remarked that this kind of test is quite complex to put in place: in fact, (i) each repetition involves destroying a nearly complete fork assembly, (ii) the deformation of the fork under bending is noticeable, therefore the cylinder must cover a comparatively long stroke each cycle, which results into low operating frequencies (3Hz) of the test bench. The original test plan comprehended testing about twenty

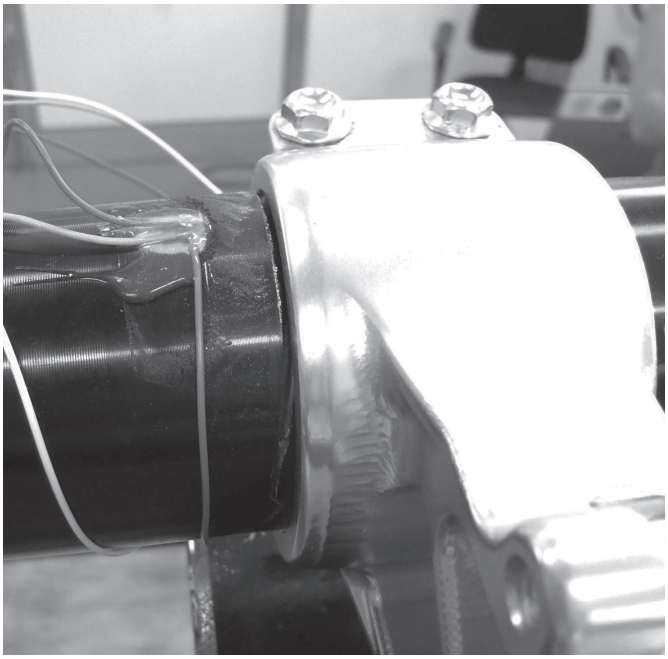

Figure 3.2: Fatigue failure on an EN AW-6082-T6 stanchion of an upside-down motorbike fork.

forks, in order to retrieve a sort of S-N curve of the finished component. By comparison with rotating bending fatigue tests executed on standard specimens, built with the same material of the stanchion (EN AW-6082-T6 aluminium alloy), it would have been possible to find out the fatigue stress concentration factor (K_f) of the actual component. Unluckily, the test bench remained in service for a few weeks, until Paioli Meccanica S.p.A. which was passing through financial troubles, stopped all the activities, preventing the experimental plan from being completed. Anyway, a total of three forks were tested, all of whom shown fatigue failures of

the stanchion underneath the joint with the lower fork clamp, as reported in Fig. 3.2. In spite of the relatively short operational life of the test bench, it allowed us to confirm that fatigue failures on these components are always located in the vicinity of the aforementioned joint. As a consequence of the impossibility to define a fatigue calculation framework for motorbike forks involving tests performed on the finished product, the author decided to pursue the objective of the research by means of both numerical methods and cheaper experimental tests which could be performed at the facilities of the University of Bologna.

3.2 The fork clamp - leg joint

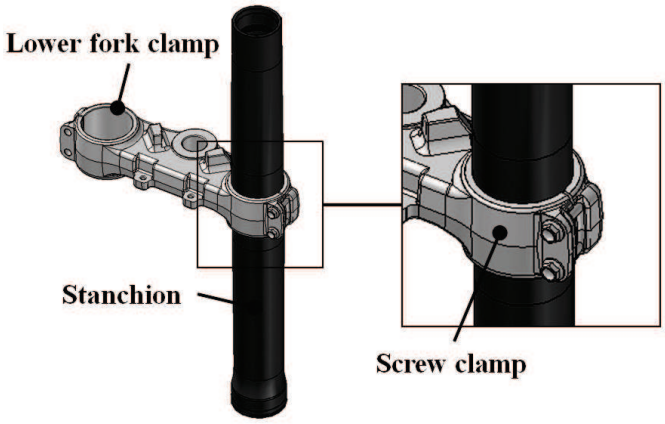

Figure 3.3: Joint under investigation (right) Enlargement of the screw clamp area (left).

The joint between the leg and the fork clamp is always realized by means of a screw clamp, comprising one or more screws. The screw clamp is a method to join a shaft and a hub, which leverages the combination of pressure and friction between the mating parts in order to achieve a certain retaining capability against axial forces and torques. The force required for developing the coupling pressure p_f at the interface is due to the axial preload of the bolts [31, 32]. In the following, we will refer to the screw clamp outline of Fig. 3.4, in accordance with [33]. That is the case of a single bolt clamp, provided with a radial slot which increases the compliance of the clamp itself improving contact with the shaft. Under such hypotesis, the part of the clamp comprised within the length l_2 can be treated as a simply supported beam, hence the concentrated contact force at the interface can be expressed as a function of the lengths l_1 and l_2 and of the actual bolt preload F_s :

$$F_n = F_s \cdot \frac{l_1}{l_2} \tag{3.1}$$

Therefore the coupling pressure p_f can be written as reported in the following Eq. 3.3

$$p_f = \frac{F_n}{D_f \cdot L_f} \tag{3.2}$$

Then, the breakaway torque of the joint is written as:

$$M_t = F = p_f \cdot {D_f}^2 \cdot L_f \cdot \mu_{lu} \tag{3.3}$$

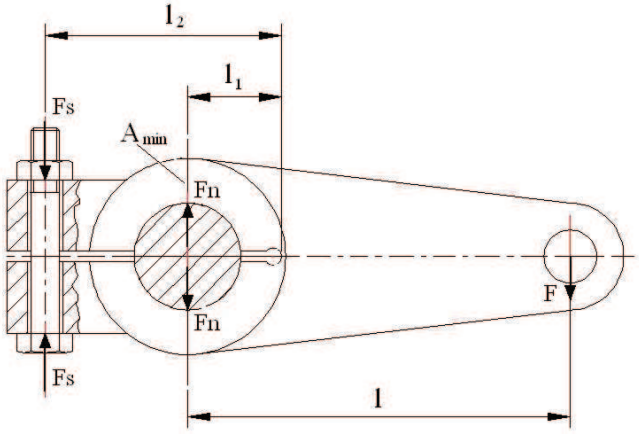

Figure 3.4: Screw clamp outline.

As specified in [34], screw clamps do not generate a constant pressure on the contact surface. Therefore, the problem is not axisymmetric in nature, and a number of parameters should be taken into account in order to evaluate the actual distribution of the contact pressure.

3.3 Stress analysis of the axisymmetric shaft hub joint

The aim of this work is to estimate the effect of the coupling pressure on the stress state and therefore on the fatigue life of the leg or stanchion. In order to symplify the problem, the joint between the fork clamp and the leg is treated as if it were an axisymmetric shaft-hub interference fit. Therefore, in the following part of this chapter, we will refer to the shaft-hub interference fit joint whose outline is given in Fig. 3.5. Under the hypotesis of plane stress (no edge effects), and limited to the case of isotropic materials for the shaft and the hub, it is possible to calculate the coupling pressure p_{0_th} by the well known Lame's solution for thick walled cylinders [35, 36, 37]:

$$p_{0\_th} = \frac{\frac{I}{D_f}}{\frac{1}{E_H} \cdot \left(\frac{1+Q_H^2}{1-Q_H^2} + \nu_H\right) + \frac{1}{E_S} \cdot \left(\frac{1+Q_S^2}{1-Q_S^2} - \nu_S\right)} \tag{3.4}$$

Where the interference I is calculated as the difference between the outer diameter of the shaft D_{Se} and the inner diameter of the hub D_{Hi}. The shaft and hub aspect ratios Q_S, Q_H are defined as the ratios between their internal and external diameters ($Q_S = \frac{D_{Si}}{D_{Se}}$, $Q_H = \frac{D_{Hi}}{D_{He}}$). E_S, E_H are the Young's moduli and ν_S, ν_H the Poisson's ratios of the shaft and the hub respectively. Under the aforementioned hypotheses, a large number of contributions can be found in the literature, dealing with the static optimization of the joint, which means maximizing the transmissible axial force or torque for a given target weight of the assembly. For example, in [38], the case of a solid shaft ($Q_S = 0$) is examined, and it is found that the maximum load capacity is achieved for an aspect ratio of the hub Q_H between 0.5 to 0.7, regardless of the frictional coefficient, of the kind of loading and of the material response (brittle or ductile). In [39] optimization is extended to interference fitted and adhesively bonded shaft-hub couplings, introducing two normalizing parameters which take into account the simultaneous effect of the materials density, the shaft aspect ratio, the hub yield strength, the coefficient of friction between the mating parts and the adhesive mean strength. In [40] is presented a design method which accounts for elastic-plastic material behaviour, limited to the case of static loads.

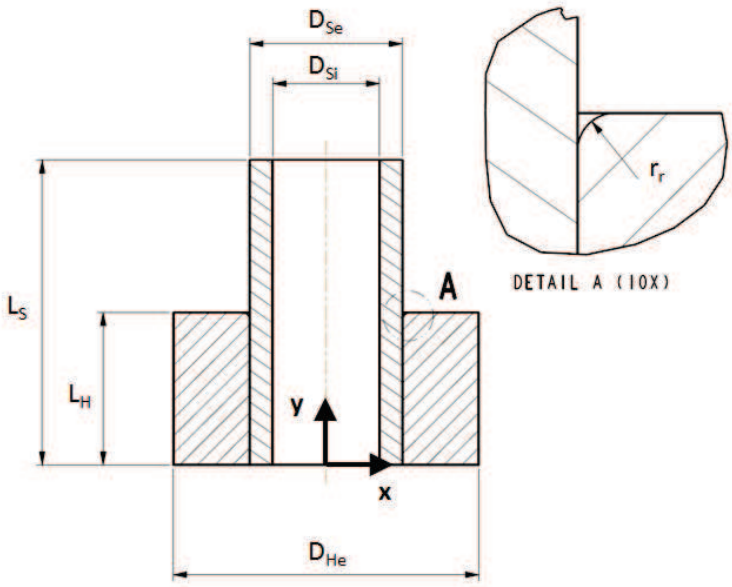

Figure 3.5: Shaft-hub interference fit joint.

Nonetheless, it is well known from the literature [36, 37, 41, 42, 43, 44] that the radial pressure at the contact extremities deviates substantially from that calculated as for 3.4. Therefore, when dealing with brittle materials or fatigue problems, the plane stress assumption is no longer applicable. In the following

is considered an infinitely long, cylindrical shaft, press-fitted into a cylindrical hub whose bore edges are rounded (see Fig. 3.5). The hub bore is assumed to be radiused because: (i) no actual hub has a perfect sharp edge (ii) the radius eliminates the stress singularity at the contact edge [45], even if the analysis is performed in the linear elastic field. The algebraic complexity of the analytical formulae currently available for the evaluation of such localised stress peaks limits their applicability in the design practice. However, retrieving the stress peaks by means of FEA, and then reporting such peaks as functions of the contact pressure calculated according to 3.4, it could be possible to provide a tool useful for designing the joint. Unfortunately, it is difficult to retrieve widely applicable stress forecasts by FEA, since the level of the contact pressure peaks depends on a number of factors such as the shaft radius, the hub outer radius, the fillet radius, the level of interference and the elastic properties of the materials in contact. In reference [46] is presented a normalizing parameter which allows the stress concentration factor at the small-end bore sides of connecting rods to be expressed as a function of a conveniently defined set of parameters (initial assembly clearance, applied load, Young's modulus) of the connecting rod - pin assembly. Based on the same idea of a normalising parameter, Strozzi et al. [47], have recently addressed the issue of preparing design charts for the stress concentration factors at the rounded edges of shaft-hub interference fits. Under the hypothesis of a shaft aspect ratio $Q_S = 0$ (solid shaft) and for a prescribed hub aspect ratio Q_H, Strozzi et al. provided a normalizing parameter ϕ (Eq. 3.5) which, given two connected members made of the same material, summarises the simultaneous effects of the reference radius for the shaft-hub joint ($r_{Se} = \frac{D_{Se}}{2}$ is the external radius of the shaft), of the fillet radius r_r and of the interference level I (difference between the external shaft diameter D_{Se} and the internal hub diameter D_{Hi}).

$$\phi = \frac{r_r \cdot I}{{r_{Se}}^2} \tag{3.5}$$

Then, using FEA, Strozzi et al. prepared design diagrams (see Fig. 7 at page 487 of Ref. [47]), which report the stress concentration factor K_t, evaluated as the ratio between the maximum von Mises equivalent stress (via FEA) and the theoretical coupling pressure 3.4 as a function of said normalizing parameter and for a selection of hub aspect ratios (Q_H values between 0.3 and 0.7).

$$K_t = \frac{\sigma_{eq\_max\_FEA}}{p_{0\_th}} \tag{3.6}$$

What follows is an extension to the case of hollow shaft ($Q_S \neq 0$) [48] of the results presented in [47]. After that, the applicability of the normalizing parameter 3.5 will be examined for the cases of: (i) different materials for the shaft and the hub and (ii) frictional contact. It must be highlighted that the following part of this paragraph is not intended to provide stress concentration factors K_t to be directly applied in fatigue calculations. In fact, according to [47], the maximum von Mises stress is evaluated on the hub, and not on the shaft, which is always the first component to undergo fatigue failure in practical applications. Moreover, no load other than that due to interference is applied to the joint, while in actual

components there is an external bending moment applied to the shaft, as detailed in Chapter 2. Anyway, the modelization technique shown here below, will serve as a benchmark for more sophisticated FEA models that will be introduced in the following part.

3.3.1 Hollow shaft

In order to carry out a comparison with the results obtained in [47] for the case of solid shaft, the model is defined under the same general hypotheses. The coordinate system is set down as shown in Fig. 3.5: the model is axisymmetric with respect to the y-axis and symmetric with respect to the x-axis. The shaft is as long as twice the length of the hub: according to [47, 49] and to preliminary tests made by the authors, such aspect ratio provides the same results, in terms of contact stresses, as if an infinitely long shaft was considered. In order to get contact pressures invariant with y in the central part of the coupling length, a hub with axial length equal to twice the shaft external diameter is chosen: $L_H = D_{Se}$ [50, 51]. In fact, as indicated in [52], the axial extension of the pressure bumps occurring at the rounded edges of the hub is of the order of twice the fillet radius r_r. According to Lamé's solution for thick walled cylinders, the contact pressure calculation for a solid shaft is still sufficiently accurate (5% error) even if the shaft is hollow, provided that $Q_S \leq 0.25$ [47]. Since the aforementioned range is covered by [47], shaft aspect ratios Q_S between 0.3 and 0.9 were examined in the present work, whereas hub aspect ratios Q_H of 0.3, 0.5 and 0.7 were considered (these values cover the practical design interest). In accordance with [47], the shaft and the hub are assumed to share the same material characteristics (steel with Young's modulus E=210GPa and Poisson's ratio ν=0.3) and the analysis was conducted in the linear elastic field. As demonstrated in [47], the material type does not affect Kt, provided that it is common to the shaft and the hub. Another simplifying hypothesis adopted here, is to model the contact as frictionless ($\mu = 0$). The reasons behind this assumption are widely discussed in [47]. Define the hub bore radius Q_r as:

$$Q_r = \frac{2r_r}{D_{Se}} \tag{3.7}$$

Varying the aspect ratio of the hub bore radius 3.7 within its practical range (from 0.01 to 0.1), the variations of K_t (see Figure 7in [47]) are within 12% to 20%, if all the other parameters are constant. Therefore, in order to minimize the modelling time, a value of $Q_r = 0.05$ (the average value in the indicated range) was adopted for the present study. For the same purpose, a fixed value was assigned to D_{Se}, whereas the variation of the normalizing parameter ϕ, in the range (from 10^5 to $5 \cdot 10^3$), was achieved by changing the diametral interference level I between different analyses. The numerical analyses were run in the Ansys Workbench R.12 code, modelling the problem as axisymmetric with respect to the y-axis. The finite element used was a 6-noded triangular, isoparametric one, named Plane183 in the Ansys nomenclature. In order to achieve the accuracy required for catching the pressure bumps profile, and therefore finding a correct value of K_t, a substantial

mesh refinement was nonetheless required in the hub bore radius area. After some preliminary tests, the authors found out that the characteristic dimension of the elements should be around $d_ref \leq 0.05$, in a circular area centred into the hub bore radius initial point, and having a radius in the order of magnitude of hundredths of millimeter (Fig. 3.6).

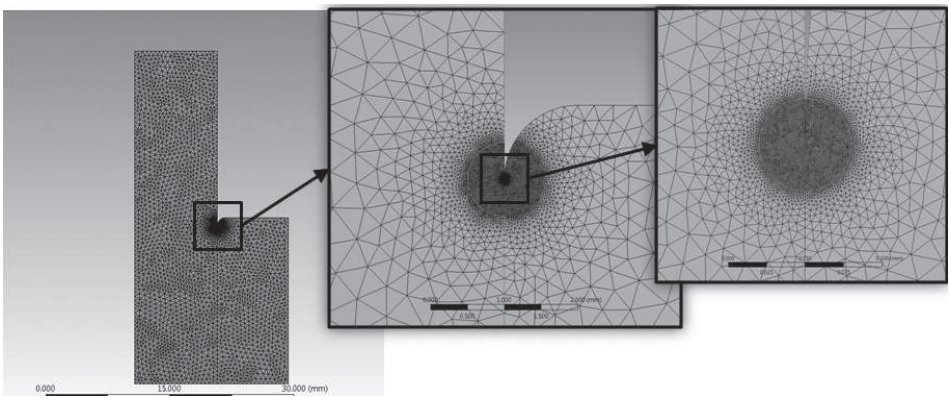

Figure 3.6: Detail of the mesh progressive refinement.

Such settings resulted into models having up to 350,000 nodes, depending on the interference level. The choice of the mesh dimensions around the radiused contact zone is supported by the findings by Olukoko et.al. [53], who demonstrated that the number of nodes in the progressive contact zone, under the imposed interference, must be higher than ten.

Pure penalty contact elements were assigned to the mating lines: the desired interference was assigned by means of the "offset" command incorporated into the Ansys Workbench contact tool [54, 55]. About one hundred analyses were run, tracking, for the hub, both the normal (compressive) stress in the radial direction and the maximum von Mises stress. The radial stress values were recorded either in the refinement zone (maximum compressive stresses) and at about half the length of the hub: the latter being recorded for the sake of comparison with the contact pressure calculated as for Lamé's formula. The typical "pressure bumps" described in [47] for the case of solid shaft are still clearly visible when a hollow shaft is analysed , as documented by stress plots of Fig. 3.7, referred to the case of $Q_S = 0.5$, $Q_H = 0.7$, $I = 0.04mm$, $r_r = 1mm$ and $D_{Se} = 40mm$.

A stress distribution similar to the case of solid shaft can be better seen looking at Figs. 3.8 and 3.9, which represent progressive enlargements of the von Mises stress plots. Since the diametral interference I is in this case equal to 0.04mm, the characteristic dimension of the elements shown in Fig. 3.9 must follow the empirical rule discussed above ($d_{ref} \leq 0.05 \cdot 0.04 = 0.002mm$) in order to obtain the convergence to correct stress values: in fact, the characteristic dimension of the elements inside the refinement circle is in the order of magnitude of $1\mu m$. The maximum stress location, as highlighted in [47] and in accordance to Hertz's theory, is still underneath the contact surface. It is important to note that, if the

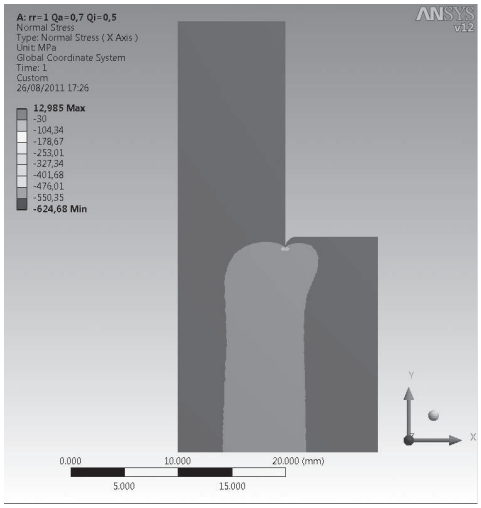

Figure 3.7: Plot of the normal stress σ_x along the x-axis, "pressure bump" in the vicinity of the radiused edge.

finite element model is set up correctly, the dark area of Fig. 3.9 comprised within the refinement circle (on the right hand side of the image, i.e. on the hub), always contains the maximum von Mises stress value. According to [47], K_t was defined in Eq. 3.6, whereas the maximum von Mises stress value comes from FEA and the coupling pressure p_{0_th} is calculated by Eq. 3.4, in which D_f is the coupling diameter, $\nu_H = \nu_S$ and $E_H = E_S = E = 200,000MPa$. Although a different FEA software (Ansys Workbench vs. Marc) was used and some minor changes regarding the mesh refinement were implemented, the results in terms of K_t for the case of solid shaft are in good accordance with those provided by [47]. The interpolating polynomial reported in Eq. 3.8 allows K_{t_S} to be calculated, for any values of $\phi \in [1.0E-05; 1.0E-03]$ and $Q_H \in]0; 0.7]$ This polynomial has been

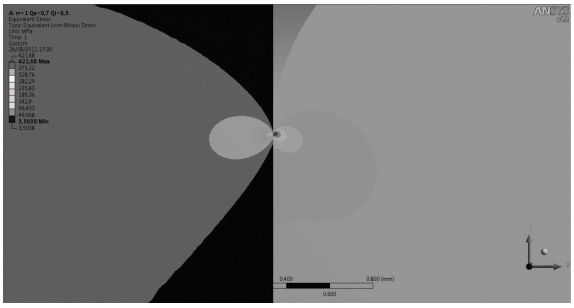

Figure 3.8: Plot of the von Mises equivalent stress, "pressure bump" in the vicinity of the radiused edge.

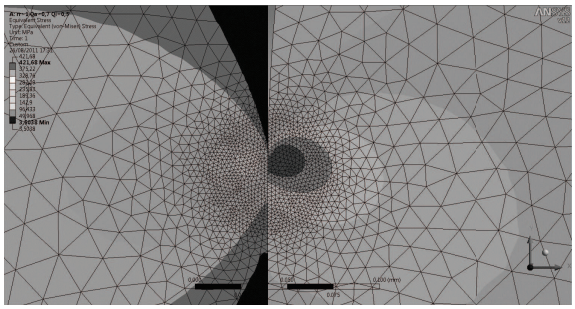

Figure 3.9: Plot of the von Mises equivalent stress, "pressure bump" in the vicinity of the radiused edge, elements shown.

retrieved by the authors by means of the FEA models described above.

$$\begin{aligned} K_{t\_S} = 9.7701 - 64094 \cdot \phi + 3.4221 \cdot 10^8 \cdot \phi^2 - 4.0031 \cdot 10^1 1 \cdot \phi^3 \\ -1.9707 \cdot 10^1 4 \cdot \phi^4 + 8.0047 \cdot 10^1 5 \cdot \phi^5 + 1.2324 \cdot 10^2 0 \cdot \phi^6 \\ +1.8223 \cdot 10^2 3 \cdot \phi^7 + 0.6088 \cdot Q_H - 32668 \cdot {Q_H}^2 + 8.9279 \cdot {Q_H}^3 \end{aligned} \tag{3.8}$$

In the following, some charts (Figs. 3.11, 3.12, 3.13) reporting the stress concentration factor K_t as a function of ϕ for different levels of Q_H and Q_S will be presented. Each diagram is referred to a value of hub aspect ratio Q_H, while each different line within the diagram relates to a specific shaft aspect ratio Q_S, and describes the trend of K_t 3.6 as a function of ϕ. It can be noticed that the value of K_t in case of hollow shaft (K_{t_H}) is always greater than K_t in case of solid shaft (K_{t_S}), for each value of ϕ and regardless of Q_H values.

In order to assess whether the parameter ϕ could still be used for evaluating K_{t_H}, diagrams similar to that of Fig. 3.14 were prepared. Here, curves representing $f = \frac{K_{t\_H}}{K_{t\_S}}$ are shown as functions of Q_S: in other words, the stress concentration factor in the case of hollow shaft was related to the stress concentration factor in the case of solid shaft. Only the two curves referring to the extreme values of ϕ (ϕ=1.0E-05 and ϕ=1.0E-03 respectively) were reported since all the others lie between them. A strong dependence of f upon Q_S can be appreciated, whereas a much weaker dependence of f upon ϕ is highlighted. In fact, the curves related to ϕ=1.0E-05 and ϕ=1.0E-03 are very close to each other, at least in the interval $Q_S \in [0.3; 0.7]$; a more pronounced dependence of f upon ϕ was noticed for $Q_S = 0.9$ (see Fig. 3.14). The diagram reported in said figure is drawn for $Q_H = 0.3$. Similar diagrams were prepared for the cases $Q_H = 0.5$ and $Q_H = 0.9$; since their actual trend is quite similar to that of Fig. 3.14 and a slight dependence of f upon Q_H was noticed, they will not be presented here. Referring to the case of $Q_H = 0.3$, shown in Fig. 3.14, the mean values of f were calculated for each Q_S. Then the polynomial function reported in Eq. 3.9 was obtained, by means of a mathematical manipulator.

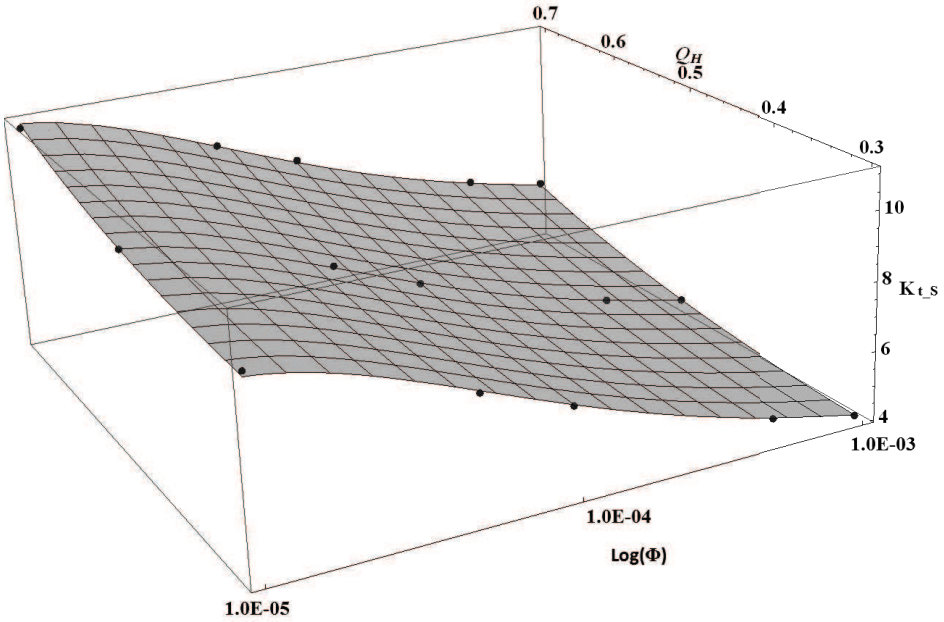

Figure 3.10: K_{t_S} versus ϕ and hub aspect ratio Q_H.

$$f\,|_{Q_H=0.3} = 1 - 0.2645 \cdot Q_S + 1.6335 \cdot {Q_S}^2 + 0.1064 \cdot {Q_S}^3 - 1.2077 \cdot {Q_S}^4 \\ -0.9426 \cdot {Q_S}^5 + 0.9200 \cdot {Q_S}^6 + 3.9880 \cdot {Q_S}^7 \tag{3.9}$$

Values of f provided by Equation 3.9 show maximum errors with respect to the actual f curves lower than 6%, whatever is the value of ϕ. Analogously, interpolating polynomials were retrieved for the case of $Q_H = 0.5$ and $Q_H = 0.7$ and reported, respectively, in Eq.3.10 and in Eq. 3.11. By applying Eq. 3.11, a maximum error of about 13% can be obtained when Q_S gets close to 0.9.

$$f\,|_{Q_H=0.5} = 1 - 0.2943 \cdot Q_S + 1.7901 \cdot {Q_S}^2 + 0.0213 \cdot {Q_S}^3 - 1.4904 \cdot {Q_S}^4 \\ -1.2071 \cdot {Q_S}^5 + 0.8870 \cdot {Q_S}^6 + 4.3459 \cdot {Q_S}^7 \tag{3.10}$$

$$f\,|_{Q_H=0.7} = 1 - 0.3738 \cdot Q_S + 1.6664 \cdot {Q_S}^2 + 0.1156 \cdot {Q_S}^3 - 1.6163 \cdot {Q_S}^4 \\ -1.3068 \cdot {Q_S}^5 + 0.8220 \cdot {Q_S}^6 + 4.3200 \cdot {Q_S}^7 \tag{3.11}$$

The K_{t_H} value of a shaft press fitted into a hub with aspect ratios Q_S between 0 and 0.9 and Q_H equal to 0.3 , 0.5 or 0.7 ($Q_S \in [0; 0.9]$ and $Q_H = 0.3; 0.5; 0.7$)

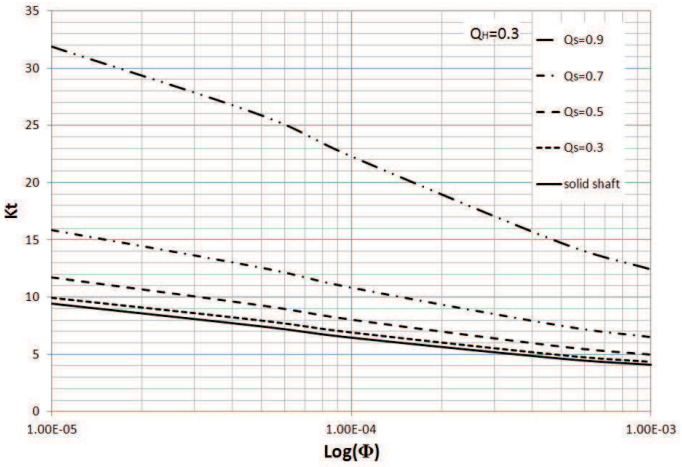

Figure 3.11: K_t versus ϕ for a hub aspect ratio $Q_H = 0.3$.

can be, therefore, calculated by means of Equations 3.9, 3.10, 3.11 and 3.12, once the K_{t_S} value provided by Eq. 3.8 is known.

$$K_{t\_H}\left\langle \phi, Q_S, Q_H \right\rangle = K_{t\_S}\left\langle \phi, Q_H \right\rangle \cdot f\,|_{Q_H}\left\langle Q_S \right\rangle \tag{3.12}$$

In order to merge Equations 3.9, 3.10, 3.11 into a unique formula to be applied for any arbitrary value of Q_S between 0 and 0.9 and Q_H between 0 and 0.7, the interpolating polynomial of Eq.3.15 is proposed, to be used together with Eq. 3.14 for calculating K_{t_H}. The surface described by Eq. 3.13 is shown in Fig. 3.15 the maximum error is always within 15%, expressed with respect to FEA.

$$\begin{aligned} g\left\langle Q_S, Q_H \right\rangle = {} & 1.0028 - 0.2810 \cdot Q_S + 1.6105 \cdot {Q_S}^2 - 0.0067 \cdot {Q_S}^3 \\ & -1.3690 \cdot {Q_S}^4 - 1.0721 \cdot {Q_S}^5 + 0.8921 \cdot {Q_S}^6 + 4.1120 \cdot {Q_S}^7 \\ & +0.4416 \cdot Q_H - 0.3434 \cdot {Q_H}^2 - 0.7794 \cdot {Q_H}^3 \end{aligned} \tag{3.13}$$

$$K_{t\_H}\left\langle \phi, Q_S, Q_H \right\rangle = K_{t\_S}\left\langle \phi, Q_H \right\rangle \cdot g\left\langle Q_S, Q_H \right\rangle \tag{3.14}$$

It must be stressed out that K_{t_H} (hollow shaft) is always greater than K_{t_S} (solid shaft), for each value of ϕ and regardless of the value of Q_H, whereas the contrary may be expected. Even if more compliant, the hollow shaft shows a higher stress increase, at the contact extremities, than the solid one. Such counter-intuitive finding, may be physically explained by observing that: (i) the K_t formula given in Eq. 3.6 has Lame's coupling pressure at denominator, which accounts for the reduced pressure due to a more compliant shaft, (ii) the higher compliance of the shaft makes it deflect more in the central part (i.e. for low values of y coordinate in Fig. 3.5) under the contact pressure. Such occurrence results into a coupling pressure distribution characterised by more pronounced peaks at the

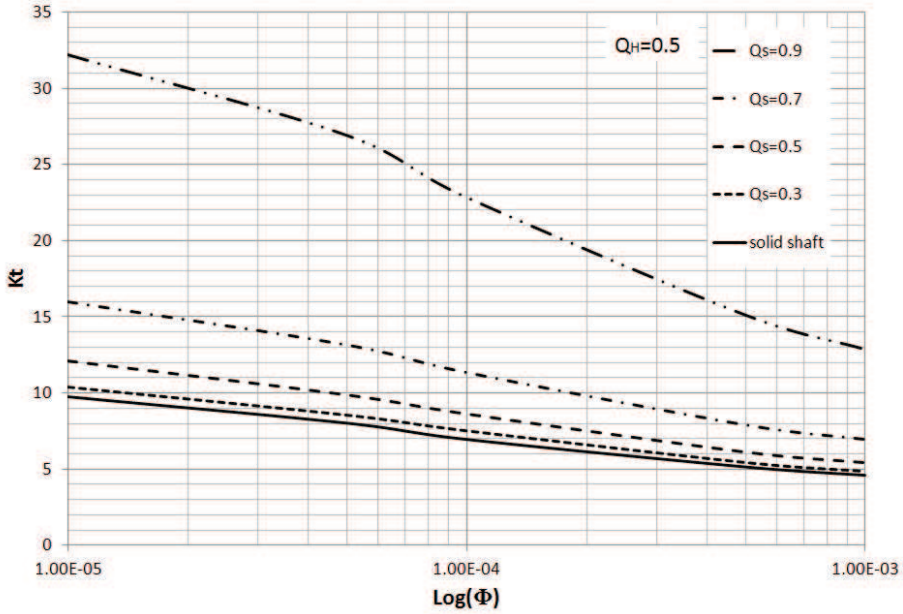

Figure 3.12: K_t versus ϕ for a hub aspect ratio $Q_H = 0.5$.

free extremity (radiused corner). In order to support the previous statement, the authors report in Fig. 3.16 a plot of the contact pressure (p) normalized over the coupling pressure (p_{0_TH} calculated according to Lame's formula) for two joints sharing all the geometrical parameters but the shaft aspect ratio; the curves refer to $\phi = 1.0E-05$. The ratio $\frac{y}{L_H}$ between the axial coordinate y and the half the length of the hub (L_H, see Fig.3.5) is reported in abscissa. It can be seen how the normalized pressure in the case of heavily hollowed shaft (thin line, $Q_S = 0.9$) becomes much greater than that relevant to the solid shaft (thick line, $Q_S = 0$) as the axial coordinate approaches the free extremity ($\frac{y}{L_H} \to 1$). Obviously, the two curves tend to $\frac{p}{p_{0\_th}} = 1$ when ($\frac{y}{L_H} \to 0$) (see also Ref. [56]). Looking at the peak values highlighted by the two markers in Fig. 3.16 (60.9 and 16.7 in the case of hollowed shaft and solid shaft respectively) it is interesting to observe that the ratio between the two values ($\frac{60.9}{16.7} = 3.65$) is close to the ratio $\frac{K_{t\_H}}{K_{t\_S}} = 3.3$ which can be calculated by means of Eq. 3.13 in the case of $Q_S = 0.9$, $Q_H = 0.5$ and $\phi = 1.0E-05$. This suggests that the radial pressure governs the stress concentration at the contact extremities, even if K_t is defined by means of the maximum von Mises stress. Lastly, it must be remarked that the values of K_t presented here refer to a given Q_r ratio. In fact the impact on K_t of a simultaneous variation of Q_r and Q_S has not been investigated.

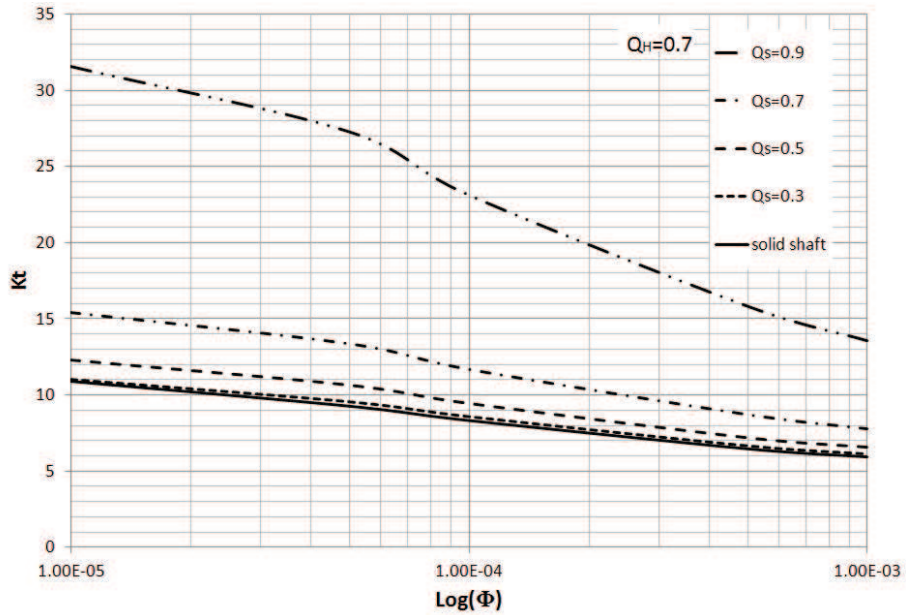

Figure 3.13: K_t versus ϕ for a hub aspect ratio $Q_H = 0.7$.

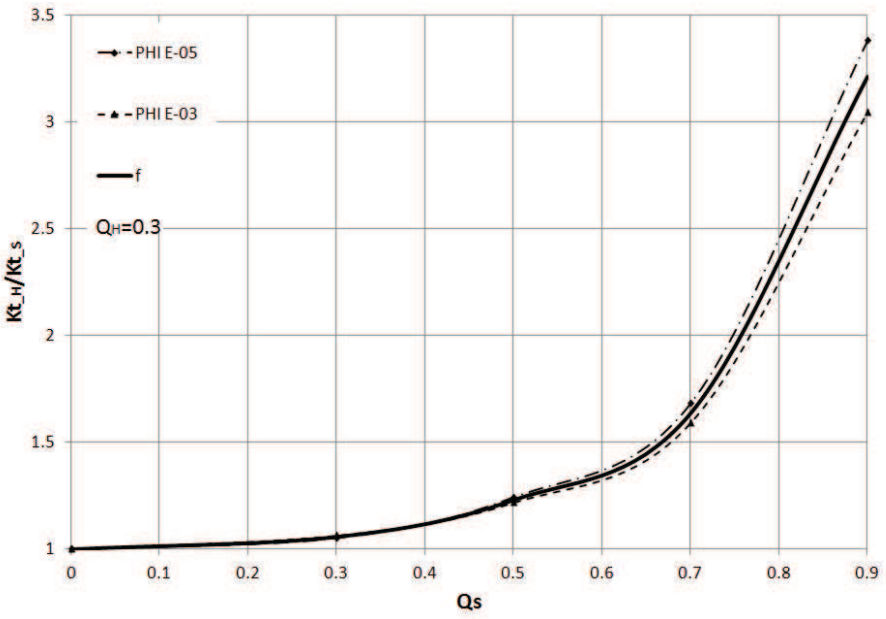

Figure 3.14: f versus Q_S for a hub aspect ratio $Q_H = 0.3$.

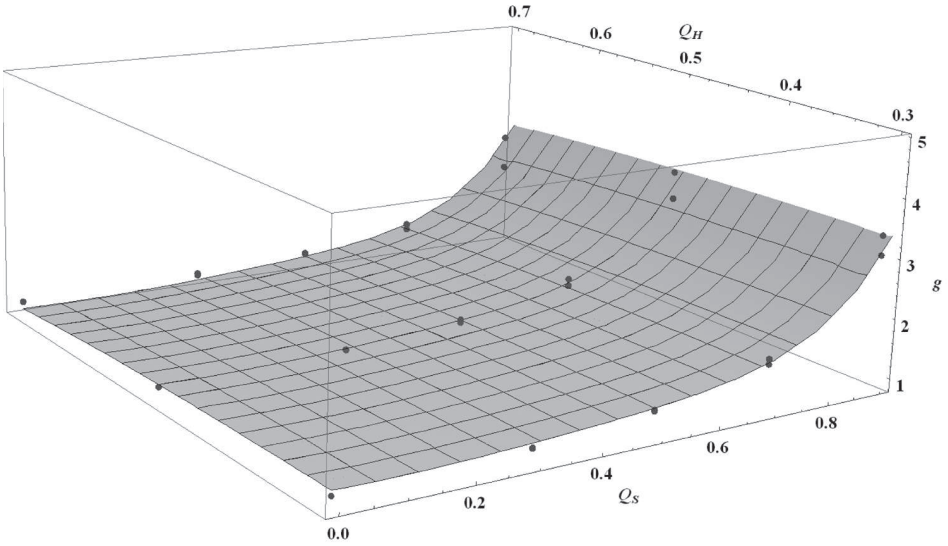

Figure 3.15: Plot of g function versus Q_S and Q_H.

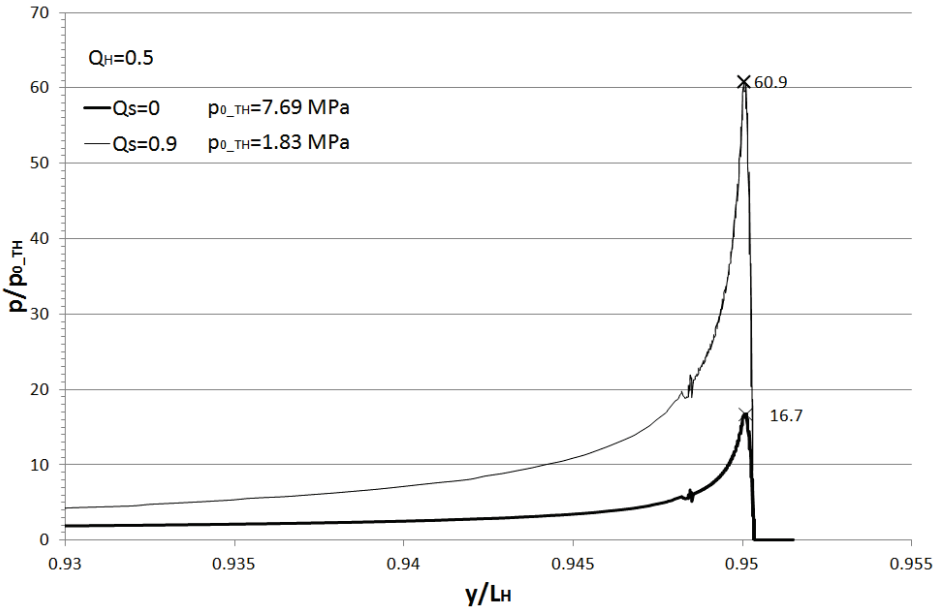

Figure 3.16: Normalized contact pressure vs. $\frac{y}{L_H}$ for two different shaft aspect ratios.

3.3.2 Numerical example - hollow shaft

Hereafter is considered an axisymmetric shaft (S) - hub (H) joint, whose members are both made of structural steel ($E = 210GPa$, $\nu = 0.3$) and whose geometrical dimensions are given in Tab. 3.1. The diagrams and the formulae illustrated above are used in order to find out the stress concentration factor K_{t_H}, therefore to calculate the maximum von Mises stress $\sigma_{eq\_max\_TH}$.

Table 3.1: Joint dimensions.

Parameter	Value	Unit
D_{S_i}	45.50	mm
D_{S_e}	70.07	mm
D_{H_i}	70.00	mm
D_{H_e}	234.0	mm
r_r	1.750	mm

For such purpose, the dimensionless ratios Q_H, Q_S, and Q_r are calculated and reported in Tab.3.2. Then, ϕ is found by means of Eq. 3.5, while the nominal coupling pressure (p_{0_th}) is computed according to Lamé's formula of Eq. 3.4.

Table 3.2: Calculated parameters of the joint.

Parameter	Value	Unit
Q_H	0.300	-
Q_S	0.650	-
Q_r	0.050	-
ϕ	1.0E-4	-
$I = D_{S\_e} - D_{H\_i}$	0.070	mm
p_{0_th}	56.00	MPa
K_{t_S}	6.493	-
g	1.479	-
K_{t_H}	9.603	-
$\sigma_{eq\_max\_th}$	537.8	MPa

Once Q_S, Q_H and ϕ are known, K_{t_S} can be calculated by Eq. 3.8 or, alternatively, retrieved by means of the diagram of Fig. 3.10 ($K_{t\_S} = 6.493$). The local value of $g = 1.479$ is calculated by means of Eq. 3.13 then, it is possible to define $K_{t\_H} = 9.603$ by applying Eq. 3.14. Therefore, the maximum von Mises stress on the hub is $\sigma_{eq\_max\_th} = p_0 \cdot K_{t\_H} = 56.00 \cdot 9.603 = 537.8MPa$. The same coupling was analyzed via FEA and the von Mises stress $\sigma_{eq\_max\_FEA}$ was read in order to compare it with the theoretical results. The FEA values are reported

in Figs. 3.17 and 3.18, the former representing the radial stress contour plot applied to the whole geometry, the latter an enlargement in the stress concentration area, which shows the peak value of the von Mises stress. The coupling pressure, retrieved from Fig. 3.17, is equal to $p_{0\_FEA} = 55.55MPa$, which is very close to $p_{0\_th} = 56.00MPa$ calculated theoretically: in Fig. 3.17 deformations were amplified by a factor of 10. The maximum von Mises stress value given by the FEA is $\sigma_{eq\_max\_FEA} = 485.7MPa$, whereas the analytical model overestimates it of about 11%.

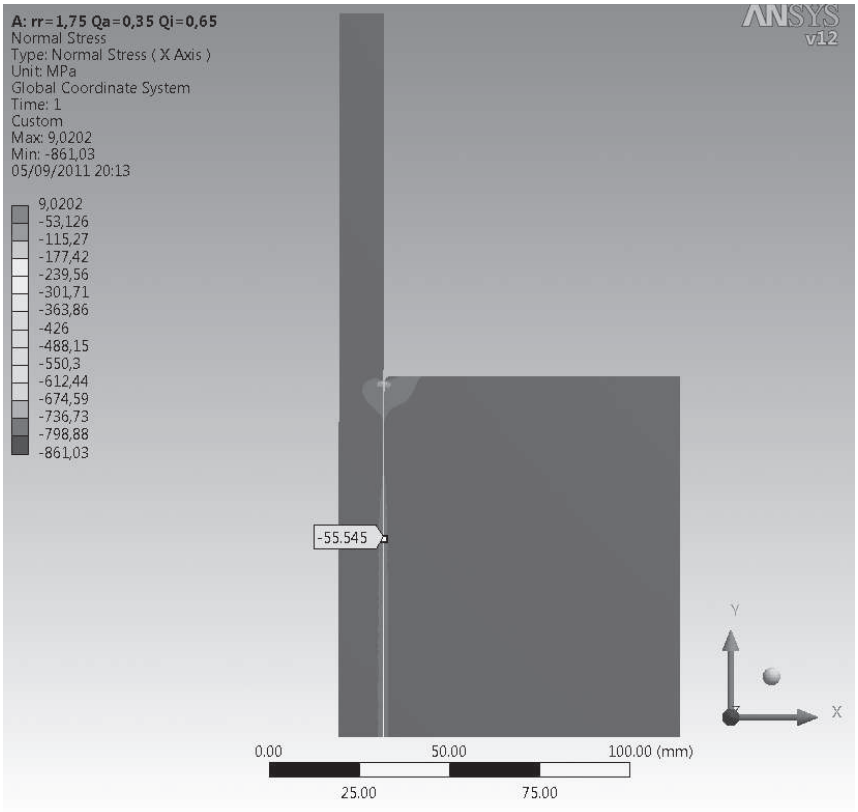

Figure 3.17: Radial stress plot: flag showing the coupling pressure.

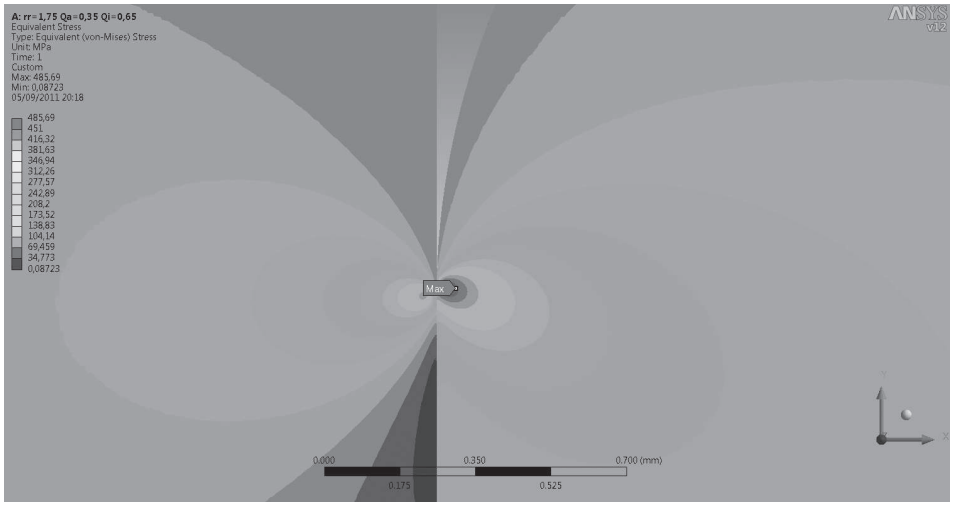

Figure 3.18: Von Mises stress plot: flag showing the peak value.

3.3.3 Mixed materials

So far, the shaft and the hub have been supposed to be made with the same material. In the practice of motorbike forks, it is indeed very common to find mixed materials in contact, as for example a fork clamp made of aluminium alloy and a stanchion made of steel. Therefore, the influence on K_t of different material elastic properties of shaft and hub, will be analysed in the following. In Tab. 3.3 the fundamental characteristics of the most common structural materials are reported.

Table 3.3: Material properties.

Material		Density ρ ($\frac{kg}{mm^3}$)	Young's modulus E (MPa)	Poisson's ratio ν	Yield limit $S_y(MPa)$
Magnesium alloy	ZM21	1.74E-6	41,000	0.35	195
Aluminium alloy	EN-AW6082	2.75E-6	69,000	0.33	304
Titanium alloy	Ti6Al4V	4.54E-6	106,000	0.34	830
Steel	39NiCrMo3	7.87E-6	200,000	0.29	910

In order to have an understanding of the influence of the material combination, in Fig. 3.19 are drawn three curves, each referred to a material combination. The solid line refers to the case of same material for shaft and hub, the dash-dot line refers to the case of magnesium alloy shaft on steel hub and the dashed line refers to the case of steel shaft on magnesium alloy hub. These are the extreme cases, and since all the other materials combinations have stress concentration factors within the range comprised between the dashed line and the dash-dot line, they are not reported in the chart. It can be noticed that, provided that ϕ be the same, the highest stress concentration factor is found for the combination in which the

shaft is more compliant than the hub. This resembles what happens in the case of hollowed shaft, in which the compliance of the shaft increases with respect to the case of solid shaft and so does the stress concentration factor.

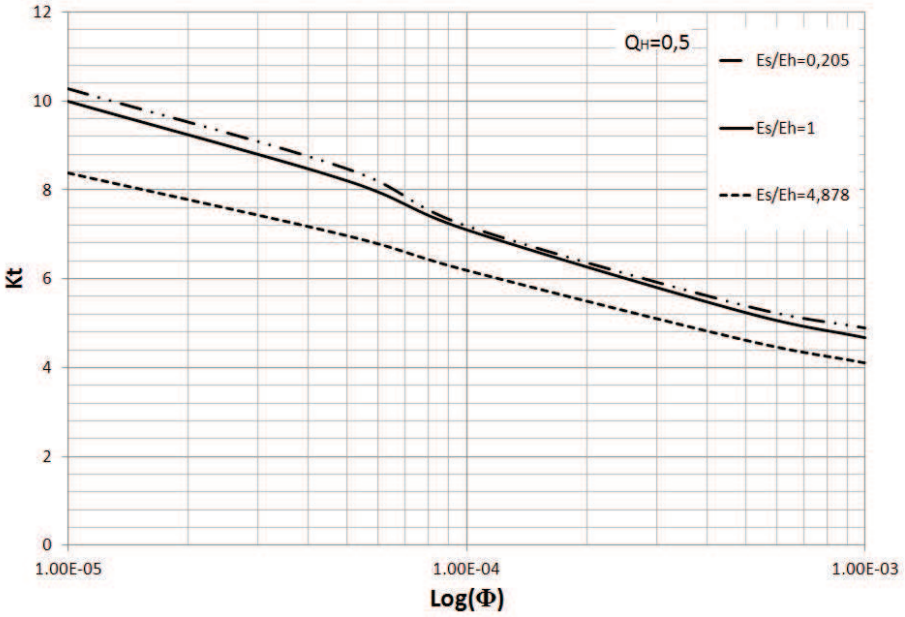

Figure 3.19: K_t versus ϕ for different material combinations.

3.3.4 Frictional contact

If friction is present in the contact between shaft and hub, a shearing stress appears on plane-xy of Fig 3.5. Such a shearing stress is limited above by the product between the coefficient of friction μ and the normal-x stress σ_X at the contact surface (Ref. [57]), as reported in Eq. 3.15:

$$\tau_{xy} \leq \sigma_x \cdot \mu \tag{3.15}$$

Depending on the value of the coefficient of friction μ and on the geometrical and elastic parameters of the joint, some areas of the contact will be sticking while some others slipping, as shown in Fig. 3.20 for a joint having $\phi = 1.0E-4$, $Q_S = 0$, $Q_H = 0.5$ and a friction coefficient $\mu = 0.3$.

Such a behaviour can make the peak value of the von Mises stress move to the contact surface, as shown in Fig. 3.21: the image is relevant to the same case shown in Fig. 3.20. As a consequence of that, K_t varies as a function of μ, even if all the other parameters are constant, as shown in Fig. 3.22. Here $K_t = K_{t\_S}$ was calculated for a joint having $\phi \in [1.0E-5, 1.0E-3]$, $Q_S = 0$, $Q_H = 0.5$ and for various values of the friction coefficient μ. The solid line represents K_t in

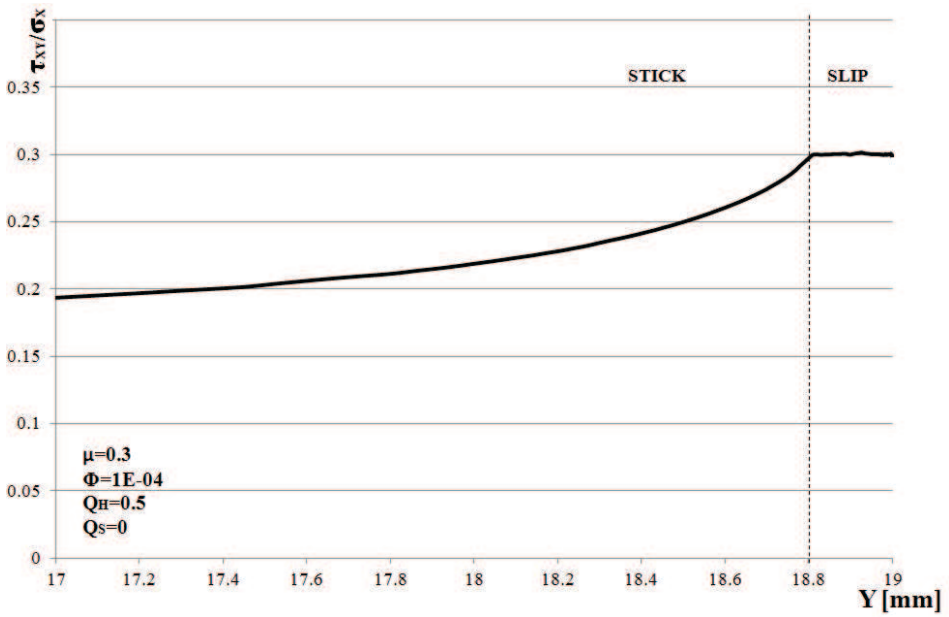

Figure 3.20: τ_{xy} versus σ_x at the contact surface, stick and slip zones.

the case of frictionless contact, whereas the dashed lines refer to frictional contact cases. Lines in Fig. 3.22 were obtained for a numerical model with the nominal dimensions reported in Tab. 3.4. Different values of ϕ were obtained by adjusting the interference level.

Table 3.4: Joint dimensions: friction.

Parameter	Value	Unit
D_{S_i}	0	mm
$D_{S\_e} = D_{H\_i}$	20	mm
D_{H_e}	40	mm
r_r	1	mm
L_S	40	mm
L_H	20	mm

In order to assess the validity of ϕ in the case of frictional contact, two tests were done: (i) three different geometries, sharing the same values of ϕ, Q_r, and $Q_L = \frac{L_H}{D_{Hi}}$ (length aspect ratio of the hub) were analysed, each at three different levels of μ and the relevant K_t values were compared (see Tab. 3.5); (ii) three identical geometries, with different Q_L were analysed, each at three different levels of μ and the relevant K_t values were compared (see Tab. 3.6). As illustrated in [47]

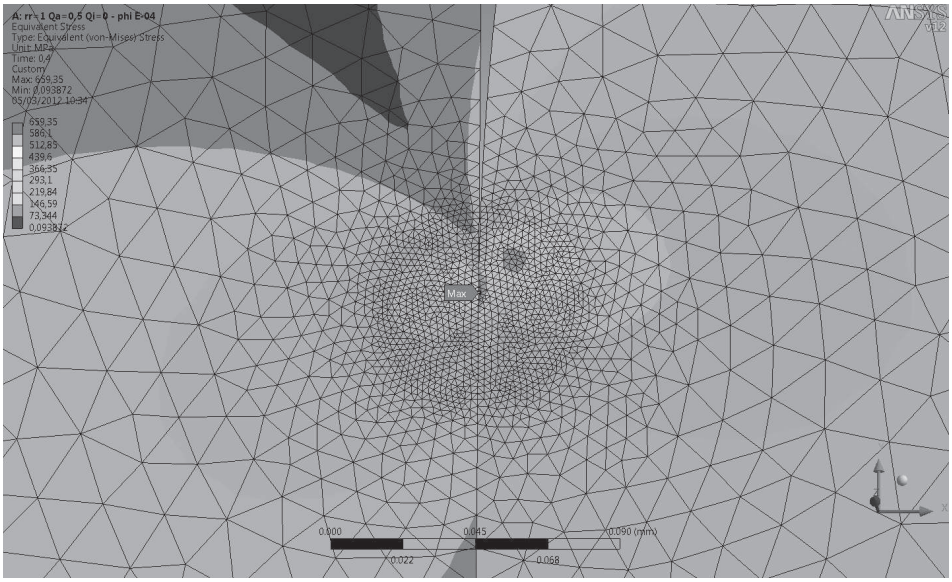

Figure 3.21: Plot of the von Mises equivalent stress at the radius edge of a joint with frictional contact.

and at the beginning of this chapter, provided that Q_r falls within the practical range $Q_r \in [0.01, 0.1]$, differences in K_t remain under 20%. In order to screen out the Q_r variable, the following comparisons will be carried out without varying said parameter. Looking at data in Tab. 3.5, it can be appreciated how geometries which, in the case of frictionless contact, would have shared the same K_t [47], now do have different K_t values. It may be argued that, under the hypothesis of frictional contact, a certain scale effect appears which influences K_t. Errors with respect to the initial geometry (Geometry 1) increase as the value of μ grows up. Similarly, as reported in Tab. 3.6, it can be seen how differences in length aspect ratio Q_L can influence K_t in the case of frictional contact. It must be noticed that Q_L would not affect K_t at all, if the contact were frictional. Again, error with respect to the reference geometry increases as the friction coefficient increases. Looking at Tab. 3.7, if the two effects are combined (which means joints with different scale and different Q_L values) errors with respect to the reference geometry will increase up to 16% in the case of Geometry 6 and $\mu = 0.5$. In the light of what shown above, it can be concluded that the normalizing capability of ϕ is hampered if friction is considered. Such an outcome is, to some extent, expected, since the mathematical formulation of ϕ is developed under the hypothesis of frictionless contact. Anyway, since comparatively small errors (maximum 4%) are found for $\mu \leq 0.1$, it can be concluded that the normalizing parameter could still be effectively used in that case without appreciable loss of accuracy.

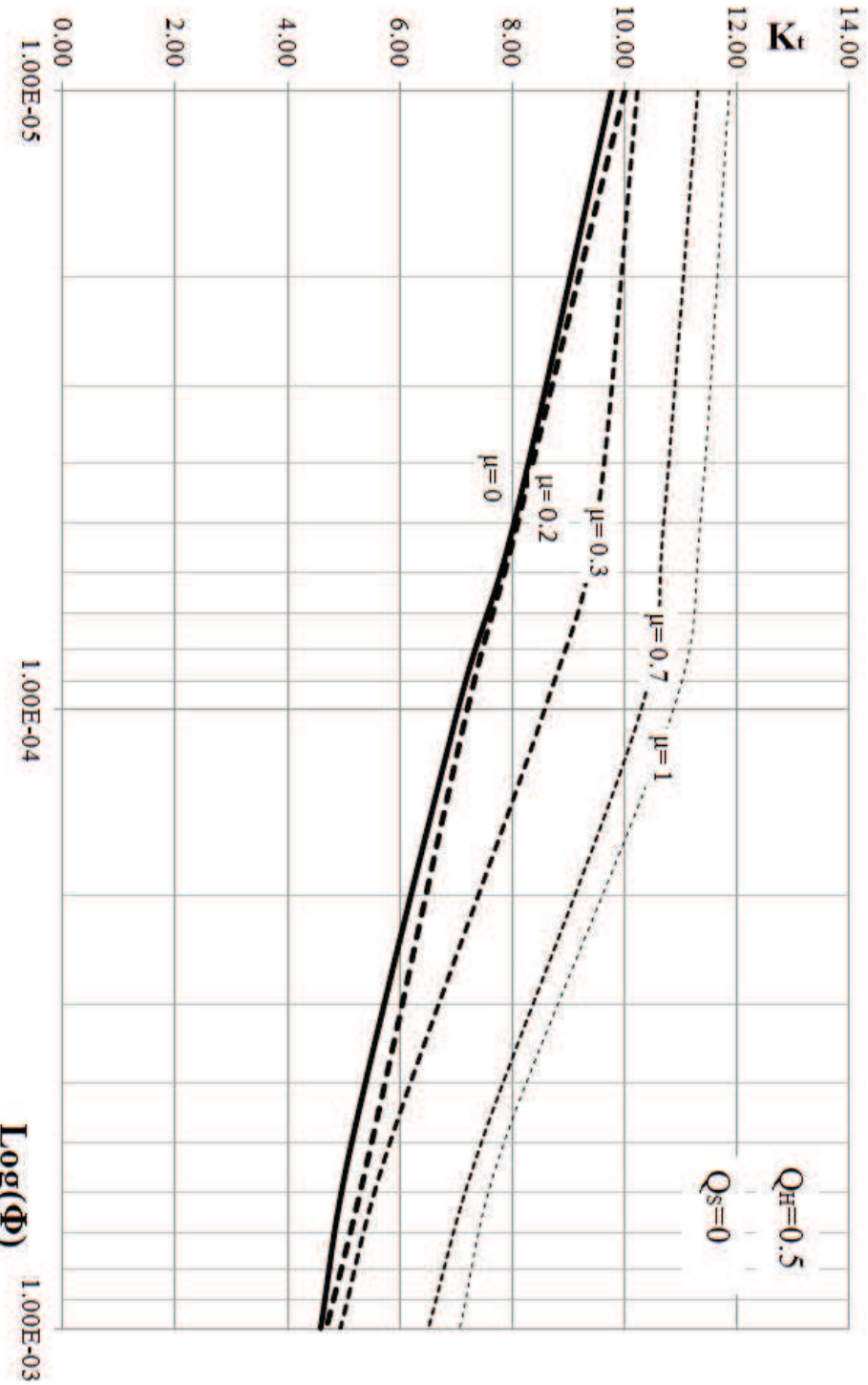

Figure 3.22: K_t as a function of ϕ and μ for a joint with solid shaft $Q_S = 0$.

Table 3.5: Comparison between different geometries with the same ϕ, Q_r, Q_L.

	Geometry 1	Geometry 2	Geometry 3	
ϕ	1.00E-04	1.00E-04	1.00E-04	-
Q_H	0.5	0.5	0.5	-
Q_S	0	0	0	-
Q_r	0.05	0.05	0.05	-
Q_L	1	1	1	-
D_{S_e}	20	50	5	mm
r_r	1	2.5	0.25	mm
I	4.00E-02	1.00E-01	1.00E-02	mm
p_{0_th}	76.81	76.81	76.81	MPa
μ 0.1				
$\sigma_{eq\_max\_fea}$	519.27	498.75	523.27	MPa
K_t	6.76	6.49	6.81	-
$e\%$	-	-4%	1%	-
μ 0.5				
$\sigma_{eq\_max\_fea}$	751.81	658.12	694.10	MPa
K_t	9.79	8.57	9.04	-
$e\%$	-	-12%	-8%	-
μ 0.7				
$\sigma_{eq\_max\_fea}$	784.25	693.15	737.61	MPa
K_t	10.21	9.02	9.60	-
$e\%$	-	-12%	-6%	-

Table 3.6: Comparison between different geometries with the same ϕ, Q_r and diameters, but different Q_L.

	Geometry 1	Geometry 4	Geometry 5	
ϕ	1.00E-04	1.00E-04	1.00E-04	-
Q_H	0.5	0.5	0.5	-
Q_S	0	0	0	-
Q_r	0.05	0.05	0.05	-
Q_L	1	1.5	0.5	-
D_{S_e}	20	20	20	mm
r_r	1	1	1	mm
I	4.00E-02	4.00E-02	4.00E-02	mm
p_{0_th}	76.81	76.81	76.81	MPa
μ 0.1				
$\sigma_{eq\_max\_fea}$	519.27	504.69	539.55	MPa
K_t	6.76	6.57	7.02	-
$e\%$	-	-3%	4%	-
μ 0.5				
$\sigma_{eq\_max\_fea}$	751.81	743.84	657.04	MPa
K_t	9.79	9.68	8.55	-
$e\%$	-	-1%	-13%	-
μ 0.7				
$\sigma_{eq\_max\_fea}$	784.25	775.70	688.70	MPa
K_t	10.21	10.10	9.11	-
$e\%$	-	-1%	-11%	-

Table 3.7: Comparison between different geometries with the same ϕ, Q_r combined effect of scale factor and different Q_L.

	Geometry 1	Geometry 6	
ϕ	1.00E-04	1.00E-04	-
Q_H	0.5	0.5	-
Q_S	0	0	-
Q_r	0.05	0.05	-
Q_L	1	0.5	-
D_{S_e}	20	50	mm
r_r	1	2.5	mm
I	4.00E-02	1.00E-01	mm
p_{0_th}	76.81	76.81	MPa
μ 0.1			
$\sigma_{eq\_max\_fea}$	519.27	525.47	MPa
K_t	6.76	6.84	-
$e\%$	-	1%	-
μ 0.5			
$\sigma_{eq\_max\_fea}$	751.81	629.24	MPa
K_t	9.79	8.19	-
$e\%$	-	-16%	-
μ 0.7			
$\sigma_{eq\_max\_fea}$	784.25	671.14	MPa
K_t	10.21	8.74	-
$e\%$	-	-14%	-

3.3.5 External loads

As detailed above, K_t defined as for Eq. 3.6 refers to the maximum von Mises stress found on the hub at the contact surface (if $\mu \neq 0$) or slightly beneath it (if $\mu = 0$). This formulation is aimed at providing a tool for quickly evaluating the static stresses in the hub due to the assembly operation. It must be highlighted that the von Mises stress peak which is taken for the evaluation of K_t, even if much higher than the normal contact pressure (p_0_th), takes place in a very small area. In fact, steep stress gradients make the von Mises stress decrease to become much smaller just a few hundredths of millimetre away from the peak location (Fig. 3.18). Such occurrence means that, if the material of the hub has an elastic-plastic behaviour, such stress peak would determine yielding of a limited volume of material, hence a re-distribution of stresses would take place. In the practice, the formulation given in Eq. 3.6 for K_t could be useful when brittle materials are joined together by interference fitting. As the most part of interference fitted joints is externally loaded in tension, bending, torsion or a combination of the three, a modelling technique for the evaluation of stress concentration factors accounting for the external loading is needed. In order to fill the gap, the author started examining some alternative FEA models which could be able to consider such requirement. The loading conditions of axial tension and bending moment will be considered in the following. If an axial tension is applied, the model would remain axisymmetric. Therefore, such loading condition can be examined by means of a two dimensional numerical model, like that shown above. On the contrary, in the case of an external bending moment, which is anti-symmetric in nature, a three dimensional model must be introduced. In the following, some preliminary FEA models will be presented. It must be highlighted that contact between the parts will always be assumed as frictionless and only the case of solid shaft will be considered.

Axial force - two dimensional model

The analysis is subdivided into two steps: a first step in which interference is created and a second one in which the axial load is applied to the shaft. In the first step, due to interference fitting, the shaft achieves a deformed shape like that shown in Fig. 3.23, relevant to the case of a steel-steel coupling with $D_{S\_e} = 30mm$, $Q_H = 0.5$, $Q_r = 0.05$, $I = 0.05mm$. The curve of Fig. 3.23 is centred in $y = 28.50mm$ which is the axial coordinate of the lower end of the hub radius. It can be appreciated how the deformed shape of the hub is characterized by an inflection point placed a few hundredths of millimetre away from the lower end of the hub radius $y_{inf} \simeq 28.51mm$. Due to stress concentrations, also axial stress σ_y will not be null at every section of the hub. Anyway, as long as no axial load is applied, expression 3.16 must hold true at any cross section of the shaft [58].

$$\int_A \sigma_y \, dA = 0 \tag{3.16}$$

As shown in Fig. 3.24, the shaft was subdivided into five sections, and a

qualitative σ_y curve was reported at each section. High stress peaks can be found both at the radius end ($\sigma_y < 0$) and at the end of the hub ($\sigma_y > 0$); as expected, the shaft free end has $\sigma_y = 0$.

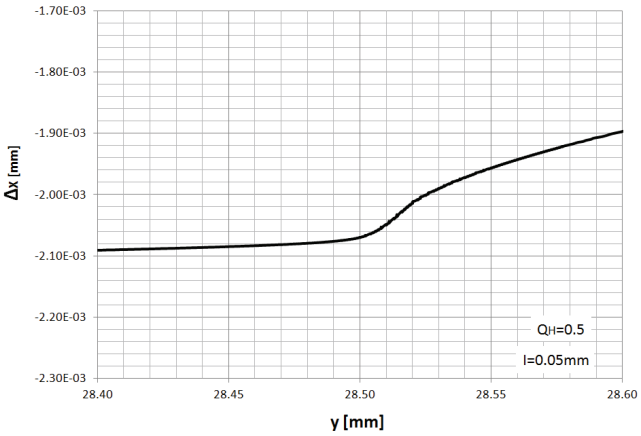

Figure 3.23: Deformation of the shaft without remote stress ($R_S = 0$) in the vicinity of the hub radiused edge.

Axial load along y-axis is applied to the shaft at its top horizontal edge, as shown in Fig. 3.25: such loading will be referred to as "remote stress" or "RS" ([59, 60]). Referring to Fig. 3.25, the model is still axisymmetric with respect to y-axis and symmetric with respect to zx-plane as well. Fig. 3.26 reports plots of σ_y, in the case of interference only (left) and in the case of axial load "RS" applied (right). In order to illustrate the position of the stress peaks with respect to the geometry, the origin of σ_y axis is coincident with the external diameter of the shaft. Positive stress peaks are indicated by means of a triangle marker, while negative ones are indicated by a cross marker. As it can be seen on the left side of Fig. 3.26, σ_y takes its maximum slightly above the radius end and its minimum at the radius end: at the top edge of the shaft, $\sigma_y = 0$. When an external load is applied, $\sigma_y = RS$ at the top edge of the shaft, while the curve is quite similar in shape to that at $RS = 0$. It is expected that the stress peaks σ_{y_max} or σ_{y_min} will promote fatigue crack propagation. In the presence of external loads, the stress concentration factor may be defined as:

$$K_{t\_max} = \frac{\sigma_{y\_max}}{RS} \tag{3.17}$$

Or:

$$K_{t\_min} = \frac{|\sigma_{y\_min}|}{RS} \tag{3.18}$$

Regardless of which definition 3.17 or 3.18 is chosen, ϕ defined as for 3.5 does not work any more, because different geometries sharing the same value of ϕ exhibit different values of the stress concentration factor.

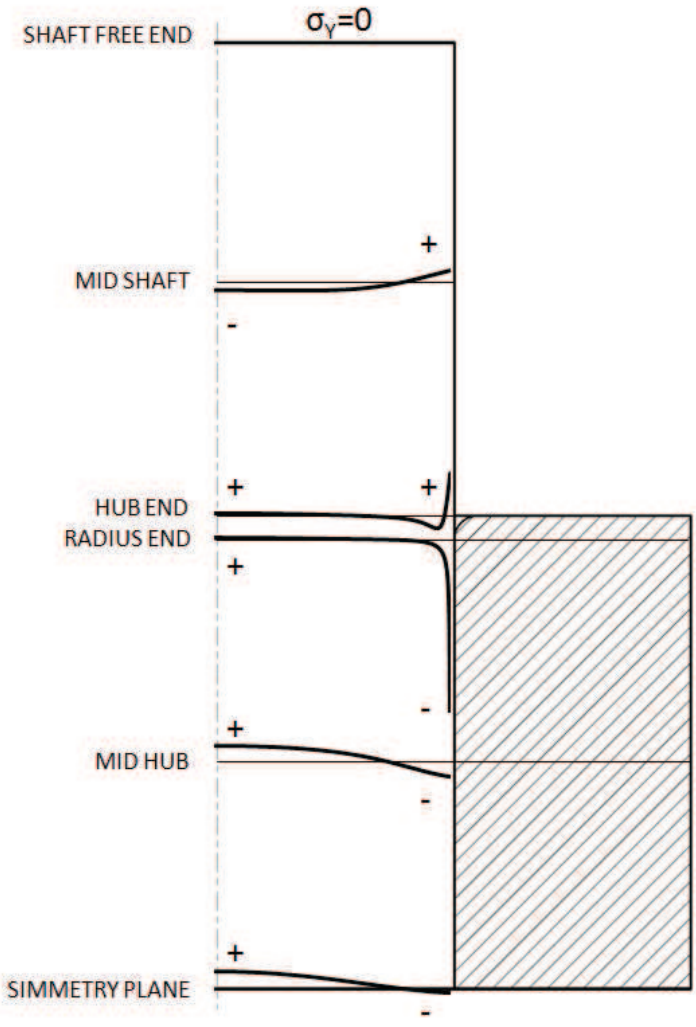

Figure 3.24: Axial stress σ_y at various cross sections of the shaft.

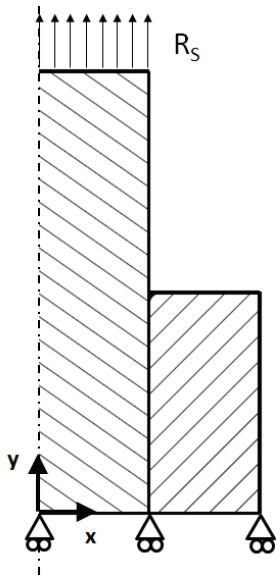

Figure 3.25: Two dimensional model with applied axial remote stress R_S.

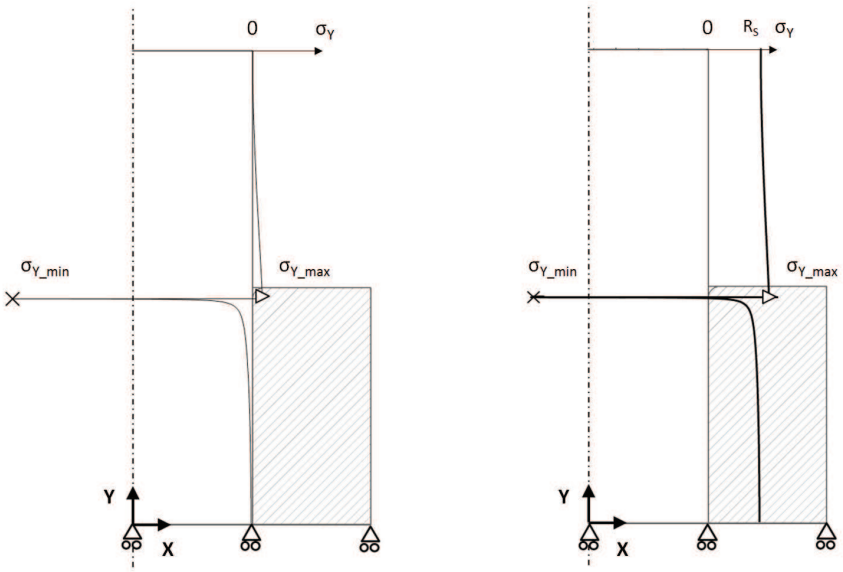

Figure 3.26: σ_y at the external diameter of the shaft, for $RS = 0$ (left) and for $RS \neq 0$ (right).

Bending moment - three dimensional model

Under the hypothesis of external bending moment acting on the shaft, a three dimensional model must be used. The model, shown in Fig. 3.27, is symmetric with respect to xy-plane and to zx-plane. The analysis is subdivided into two steps, as discussed above for the case of axial loading. Bending load M_b is applied along z-axis in Fig. 3.27. In order to reduce the computational effort, some simplifications were introduced in the present model. First of all, due to the stress distribution associated with bending, yz-plane is the neutral plane with respect to the bending moment along z-axis. Then, the most stressed areas will be those at the outer radius of the shaft and at the farthest distance from said plane. In the light of that, the shaft and the hub were subdivided into three slices each, by means of two section planes passing through y-axis and set 15° apart from xy-plane. Doing that, it was possible to assign a finer mesh dimension to the outer slices and a coarser one to the central slice. The three shaft and hub slices are joined together by means of bonded contact elements characterized by a pure penalty formulation. The two external slices are thick enough to avoid any perturbation of the bonded contact zone on the stresses in the area of interest. As for the contact formulation used at the shaft-hub contact surface, it is identical to that of two dimensional models shown above. The most part of the resulting three dimensional geometry is sweepable, which means that the body can be meshed with hexahedral and wedge elements. This is helpful, because the number of nodes and elements required for meshing a a swept body is usually much smaller than that needed for meshing the same body with the free mesher. In addition, the time to create these elements is much smaller. For that reason, 20-noded hexahedral elements were used for the whole model. Even if higher order elements are used in the three dimensional model, their characteristic dimension is quite bigger than that of the axisymmetric model. Therefore, a comparison with results of an equivalent two dimensional model is needed. A tree dimensional model whose dimensions are reported in Tab. 3.8 will be examined below.

Table 3.8: Three dimensional model dimensions.

Parameter	Value	Unit
D_{S_i}	0.00	mm
D_{S_e}	11.014	mm
D_{H_i}	11.00	mm
D_{H_e}	16.00	mm
r_r	0.50	mm
L_S	44	mm
L_H	22	mm

In order to assess the quality of the three dimensional model, it was compared with the two dimensional model shown in the previous section. The comparison was carried out on the same geometry (same dimensions and interference) and

under the same loading condition (axial force on the shaft). Since the radial deformation Δ_x seems to influence the stress concentration factor greatly, results in terms of σ_y and in terms of Δ_x were compared.

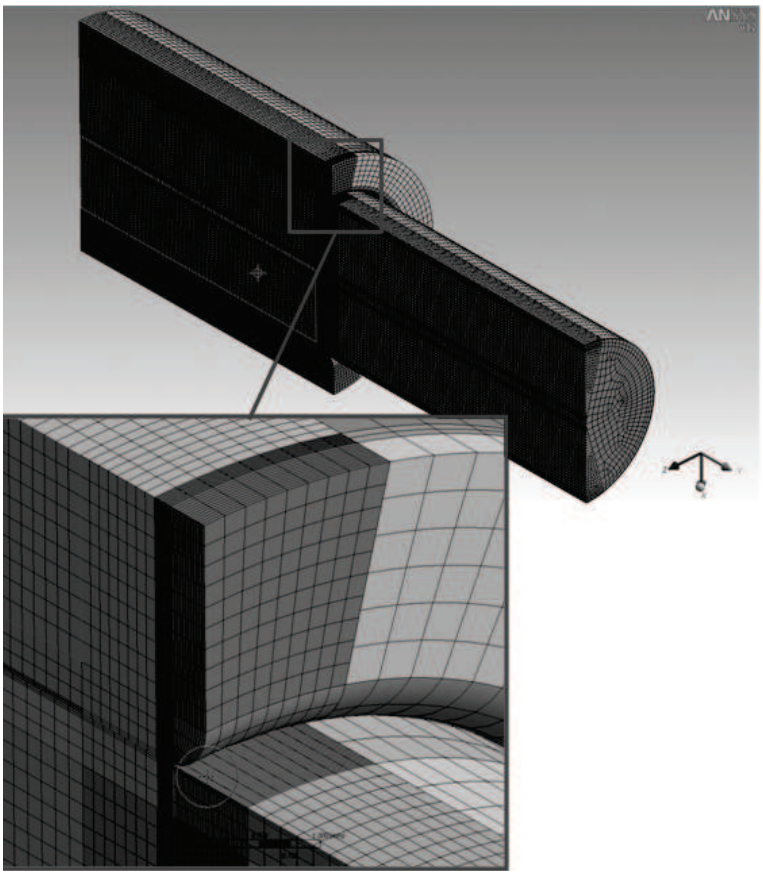

Figure 3.27: Three dimensional FEA model with a detail view of the hub bore radius zone.

Fig. 3.28 reports in abscissa the axial coordinate y and in ordinate the radial deformation Δ_x. The thin solid line refers to deformation of the two dimensional model whereas the thick dashed line refers to the radial deformation of the three dimensional model. As it can be appreciated from the plot, deformations in the vicinity of the hub bore radius are similar, with no appreciable discrepancies between the two. The characteristic inflection point is still clearly visible in the three dimensional model as well (compare Fig. 3.23 with Fig. 3.28). In terms of stresses (Fig. 3.29) the three dimensional model performs slightly worse, since a difference of about 15% between the two negative stress peaks (cross markers in figure) is recorded. Such aspect should be improved in the future, perhaps increasing the number of elements at the radius end or leveraging more complex sub-modelling

techniques. Conversely, the positive stress peak $\sigma_{y\_max} = 146MPa$ is quite the same for the two models.

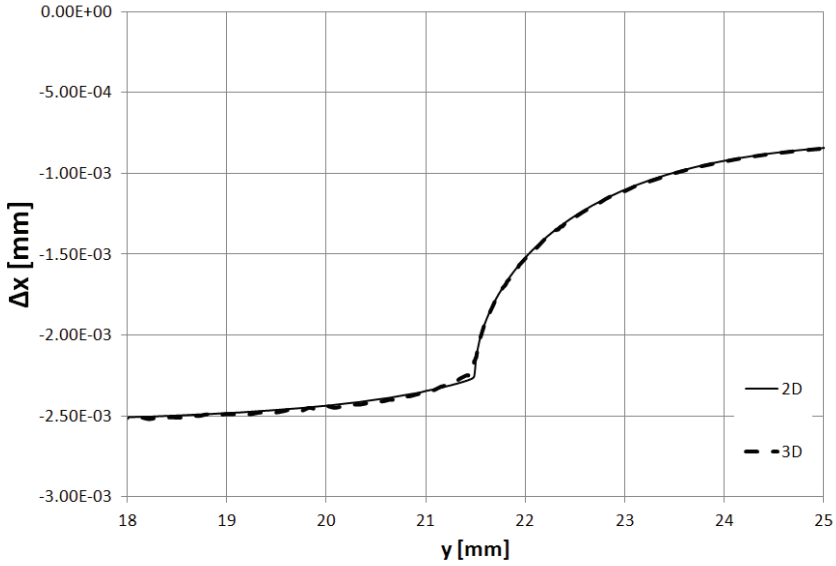

Figure 3.28: 3D model versus 2D model, radial deformation Δ_x.

While the application of axial stress would produce symmetrical effects on the two sides of the shaft, bending determines different σ_y values on the two sides. In Fig. 3.30 are reported two curves: the solid one relevant to the axial stress at the compression side of the shaft and the dashed one referring to the opposite side of the shaft, which is in tension. The geometrical data of the joint considered in Fig. 3.30 are those reported in Tab 3.8: a bending moment of $20,000Nmm$ is applied along z-axis at the shaft free end. It can be clearly seen that residual axial stresses due to interference fitting add to those due to bending moment M_b. At the point of maximum tension, stress increases in magnitude when the relevant side of the shaft is in tension. On the contrary, stress at the point of minimum (negative peak) increases in magnitude when the relevant side of the shaft is compressed. Obviously, far away from the stress concentration, on the right side of the plot in Fig. 3.30, axial stresses tend to:

$$\sigma_{y\_shaft} = \frac{M_b \cdot D_{S\_e}}{2 \cdot I_{zz\_S}} \simeq 153MPa \tag{3.19}$$

while on the left side of the same figure, the shaft and the hub work as parallel connected elements, then the maximum bending stress on the shaft can be written as:

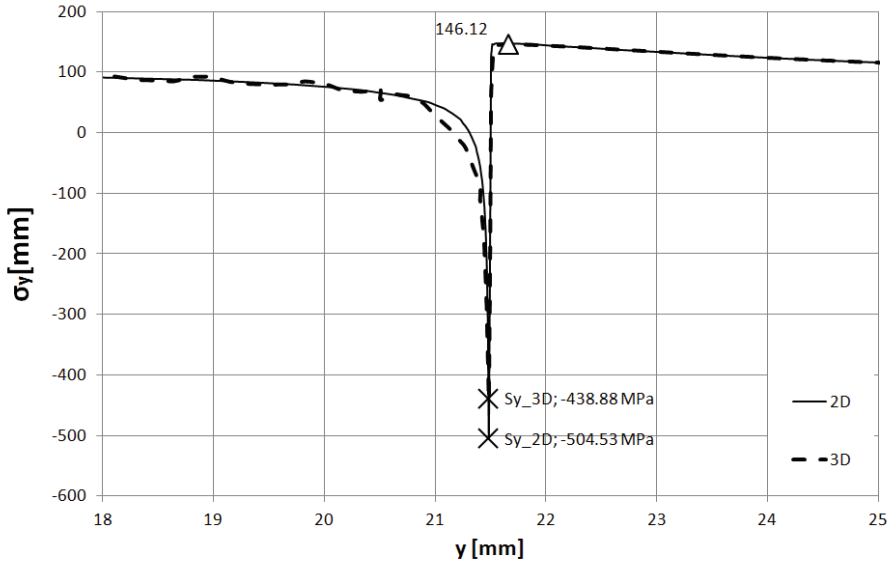

Figure 3.29: 3D model versus 2D model, axial stress σ_y.

$$\sigma_{y\_shaft\_hub} = \frac{M_b \cdot D_{S\_e}}{2 \cdot I_{zz\_S} + I_{zz\_H}} \simeq 36MPa \tag{3.20}$$

It is worth highlighting that the negative stress peak always takes place at end of the radius, while the positive stress peak is slightly shifted towards higher values of the axial coordinate. Tests made on different geometries and different interference levels shown how the positive stress peak magnitude is influenced by interference while its axial coordinate is not: see Fig. 3.31.

Eq. 3.21 is a good approximation of the curves shown in Fig. 3.32:

$$\Delta_{x\_int} = a + \frac{b}{1 + c \cdot \exp(-d \cdot y + h \cdot y^2 + l \cdot y^3 + m \cdot y^4)} \tag{3.21}$$

Where b, c, d, h, l, m are constants and y is the axial coordinate. By adjusting the six constants, it is possible to fit the curve to each interference level. Then, nullifying the second derivative of each curve:

$$\frac{\partial^2 \Delta_{x\_int}}{\partial y^2} = 0 \tag{3.22}$$

it can be calculated the axial coordinate of the inflection point of each curve. Therefore it can be seen that the axial stress positive peak is always located at the same coordinate of the inflection point of the deformed shape of the shaft (Fig. 3.32). So far, the author prepared a preliminary diagram of K_t, expressed

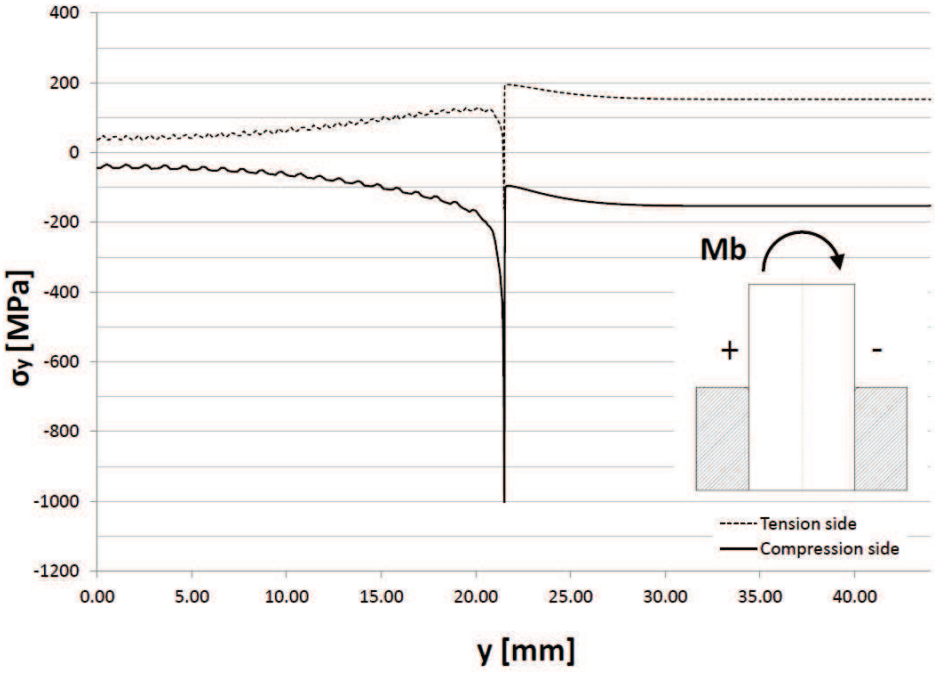

Figure 3.30: Axial stress σ_y on the tension and compression sides of a shaft hub joint subject to bending moment M_b.

according to 3.17, for different levels of interference and three different values of the hub bore radius. The result is plotted in Fig. 3.33. Such curves are obtained on the geometry reported in Tab. 3.8, by modifying the interference level and the hub bore radius. Even if the result has to be confirmed on different geometries, and provided that the radius is comprised in the practical range suggested in [48], the stress concentration factor as above defined seems to be scarcely influenced by the radius dimension and to be proportional to interference. Since the model is yet considered not sufficiently accurate in predicting the axial stresses at the end of the hub radius, K_t defined as for Eq. 3.18 is not provided here. Future developments of the numerical part of the work will deal with improving the accuracy of the three dimensional model. Since the joint is characterised by a complex three dimensional stress state with steep gradients, a failure criterium like those presented in [61, 62, 63, 64, 65] shall be introduced. The FEA models developed so far will serve as a tool for future investigations based on such criteria.

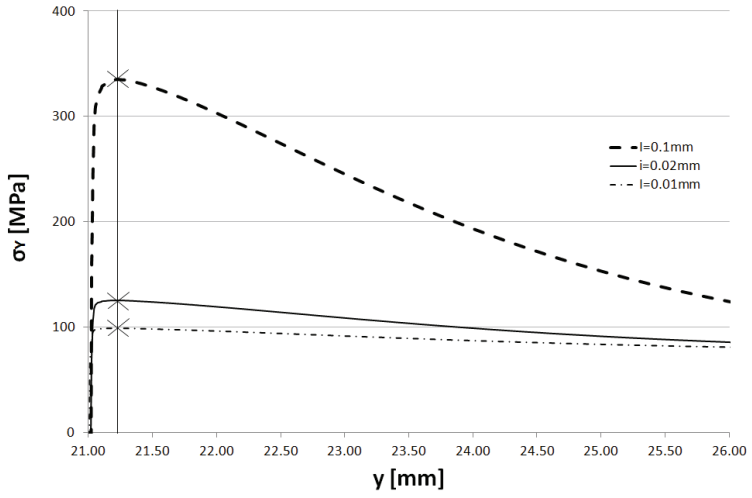

Figure 3.31: Axial stress σ_y on the tension side of a shaft hub joint subject to bending moment M_b, for three different interference levels.

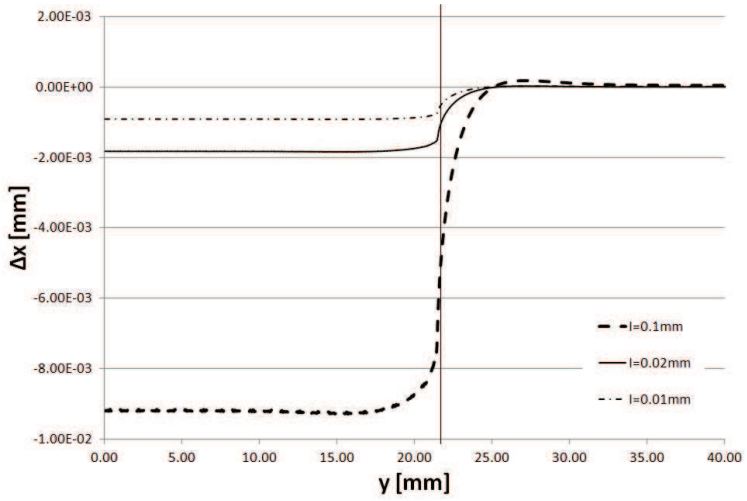

Figure 3.32: Radial deformation Δ_x on the tension side of a shaft hub joint subject to bending moment M_b, for three different interference levels.

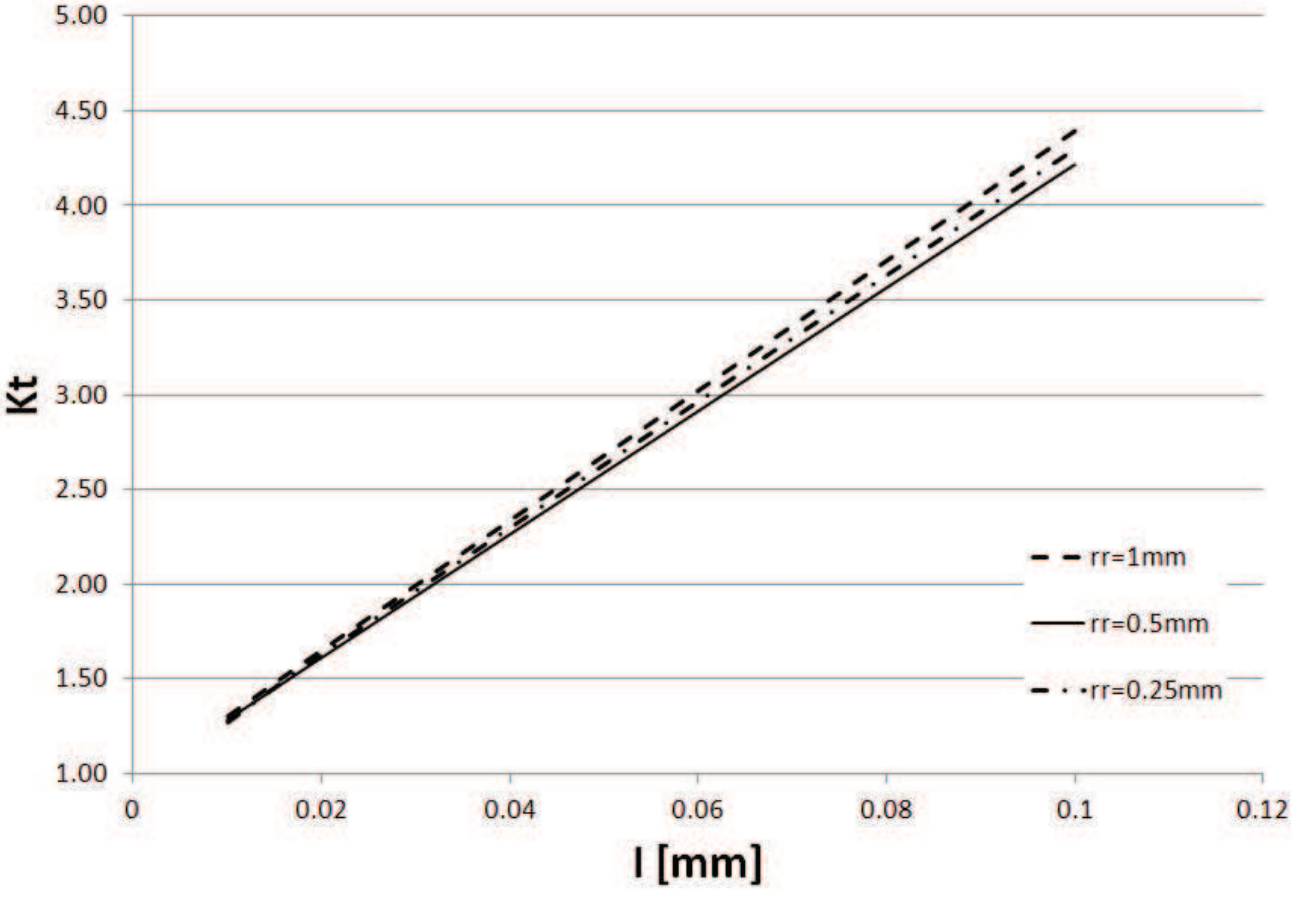

Figure 3.33: Stress concentration factor (calculated according to Eq. 3.17) for different levels of interference and hub bore radius.

Chapter 4

Fatigue tests

4.1 Materials and methods

As explained in Chapter 3, experimental tests aimed at evaluating the fatigue life of actual components comprising interference fitted joints are very complex to set up as well as very expensive to carry out, due to materials cost and to comparatively low achievable testing frequencies. Therefore, assessing the fatigue performance of interference fitted shaft-hub couplings would be easier if the effect of interference could be replicated on a scaled model, which could fit on fatigue testing equipment available in the laboratories of the University of Bologna. In the light of that, the author designed a new specimen for rotating bending fatigue testing which will be described in the following. The rationale of the experimentation is retrieving the fatigue stress concentration factor K_f of a certain kind of interference fitted joint by comparing the result in terms of endurance limit at $2 \cdot 10^6$ cycles of the newly designed ("notched") specimen with those of a plain specimen realized according to [66] and provided that all the other parameters be constant. Results were analysed according to [67]. The first experimentation began in the last months of 2012 and the first results will be illustrated below.

4.1.1 Design of the specimens

The rotating bending test bench available at our laboratories is manufactured by Italsigma S.r.l. of Forlí, Italy (Fig. 4.1). It is capable of performing four points bending tests according to the diagram reported at page 13 of [66]. There is a drive mandrel, actuated by an electric motor whose speed can be continuously adjusted up to a maximum of $n = 3600 rpm$. Supporting the specimen at the opposite side there is a free mandrel. Both the mandrels are hinged at the main frame of the bench, and by application of a mass, they are capable of transmitting a certain bending moment to the specimen. Number of cycles to failure are recorded by means of a counter, which stops when the specimen fails. Each of the two mandrels has a threaded nut which preloads a tapered split collet whose internal diameter bears one end of the specimen.

Split collets are interchangeable, in order to adapt to different specimen sizes. The biggest collet available for our test bench has an internal diameter $D_{SC\_i} =$

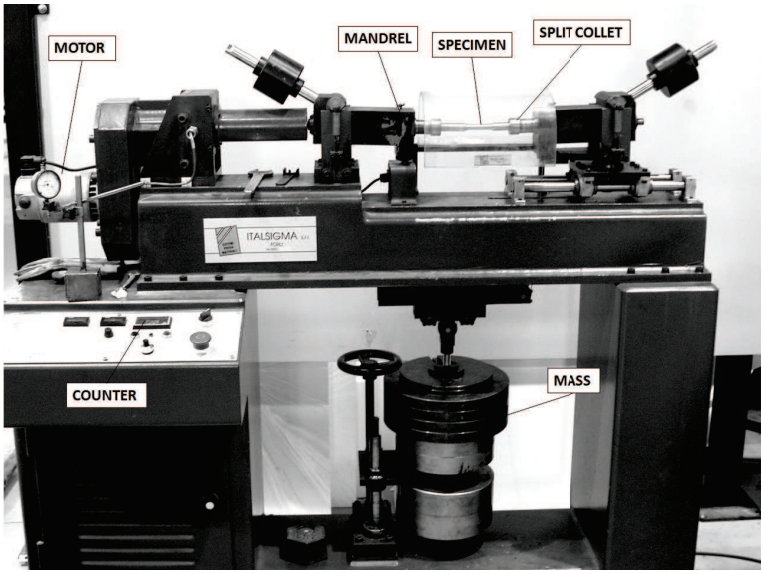

Figure 4.1: Rotating bending fatigue test bench.

$16mm$, while the maximum allowable specimen length is $250mm$.

Plain specimen

The plain specimen was designed according to [66], with dimensions shown in Fig. 4.9 of 4.3. The cylindrical extremities of the specimen have a diameter of 16mm, which fits the aforementioned collets. A total of twenty plain specimens were prepared.

Shaft-hub specimen

As reported in [66], fatigue tests on "notched" specimens are not covered by such standard, since the shape and size of notched specimens have not been standardized. However, fatigue test procedures described in [66] may be applied to fatigue tests of "notched" specimens. A drawing of the "notched", or shaft hub, specimen is reported in 4.3. When dealing with shaft hub couplings, the most important parameters to control are D_{S_e} and D_{H_i}: in fact, the difference between the two gives the diametral interference, which is proportional to the coupling pressure (Eq. 3.4). Define the specific interference as follows:

$$I\% = \frac{I}{D_C} \cdot 100 \tag{4.1}$$

where I is the diametral interference and D_C is the coupling diameter. Since $I\%$ is directly proportional to coupling pressure, as the mating parts become smaller, and assuming that the coupling pressure must be such that the equivalent stress at

the inner radius of the hub does not overcome yielding, interference must decrease as well. If a solid steel shaft is joined with a steel hub having a $Q_H = 0.5$ with a specific interference $I\% = 0.1\%$, the mean coupling pressure, calculated according to (Eq. 3.4) is $p_{0\_th} \simeq 77MPa$. For instance, referring to a coupling diameter $D_C = 10mm$, $I\% = 0.1\%$ means that the diametral interference I is equal to $0.01mm$. Diametral interferences smaller than that are hardly feasible in the practice, due to manufacturing limits and to control issues. Moreover, in order to obtain consistent results in the experimentation, the coupling pressure should vary in a narrow range across the entire batch of "notched" specimens. In the present case, the maximum allowable external diameter of the hub is $D_{H\_e} = 16mm$, which means that comparatively higher values of Q_H shall be preferred, in order to work with greater coupling diameters and therefore with practical interference ranges. Hence, a nominal external diameter $D_{S\_e} = 11mm$ was selected for the hub, which means that a $Q_H = 0.688$ is realized. Such hub aspect ratio is comprised within the range described in Chapter 3. In order to realize a specimen whose stress state could be effectively evaluated by means of numerical models like those reported in Chapter 3, the hub bore was rounded with a radius equal to $r_r = 0.5mm$. The radius aspect ratio is therefore $Q_r = 0.09$, which falls within the range discussed above. Coupling pressure is expected to be the most important parameter in defining the fatigue life of "notched" specimens. Then, in addition to what said above, particular care had to be taken in assessing possible influences of the test bench fixtures on the actual coupling pressure between specimen shaft and hub.

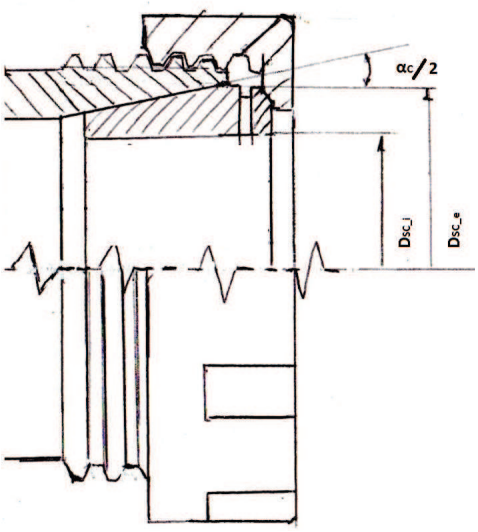

Figure 4.2: Split collet of Italsigma rotating bending test bench.

In fact, split collets like that shown in Fig.4.2 create a certain coupling pressure as a device for securing the specimen. Since accurate control of the coupling pressure between the shaft and the hub of the "notched" specimen is needed for

achieving consistency of the experimental results, pressure due to split collets on the external surface of the hub was evaluated upfront. The easiest way to do that, is tightening a split collet on a specimen with $D_{H\_e} = 16mm$ at the maximum preload value indicated by the manufacturer of the test bench and then measuring the axial displacement of the nut. Doing this way, it is possible to evaluate the actual interference realized between the hub external surface and the collet internal surface. Provided that material and geometrical data are known for both the specimen and the collet, it is possible to calculate back the coupling pressure, as shown in Tab. 4.1.

Table 4.1: Split collet: specimen coupling pressure.

Parameter	Description	Value	Unit
a	Nut axial displacement	0.05	mm
D_{SC_e}	Split collet external diameter	25.55	mm
D_{SC_i}	Split collet internal diameter	16	mm
l_{SC}	Split collet cone length	26	mm
α_{SC}	Cone angle	0.352	rad
E	Young's modulus (collet and specimen)	210,000	MPa
Q_{SC}	Split collet aspect ratio	0.63	-
D_f	Coupling diameter	16.009	mm
I_{SC}	Interference	0.018	mm
p_{SC}	Split collet pressure	73.2	MPa

Once p_{SC} is known, it is possible to numerically evaluate its influence on the coupling pressure between shaft and hub. A two dimensional axisymmetric numerical model like that shown in Fig. 4.3 was developed for such purpose.

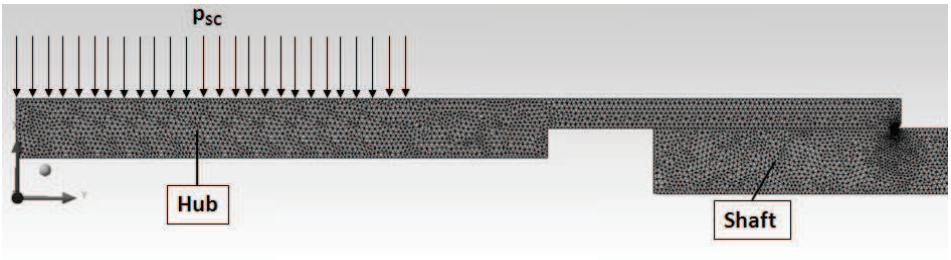

Figure 4.3: FEA model for evaluating the influence of external pressure due to split collet p_{SC} on the coupling pressure σ_x of the shaft hub specimen.

Results in terms of stresses are reported in Fig.4.4. There are two curves: the thin solid curve refers to coupling pressure of the specimen without any external pressure applied $p_{SC} = 0$, while the thick dashed curve represents the coupling pressure of the specimen when the collet is preloaded and the maximum value

$p_{SC} = 73MPa$ is achieved. As it can be seen in the chart of Fig. 4.4, the split collet pressure p_{SC} yields no appreciable effect on the coupling pressure of the shaft hub specimen. An attentive examination of the pressure peak abscissa reveals that such peak moves slightly to the right: this is related to axial elongation of the specimen hub, due to Poisson's effect, under the action of p_{SC}. In any case, this would not affect the experimentation as well as the correlation with numerical models.

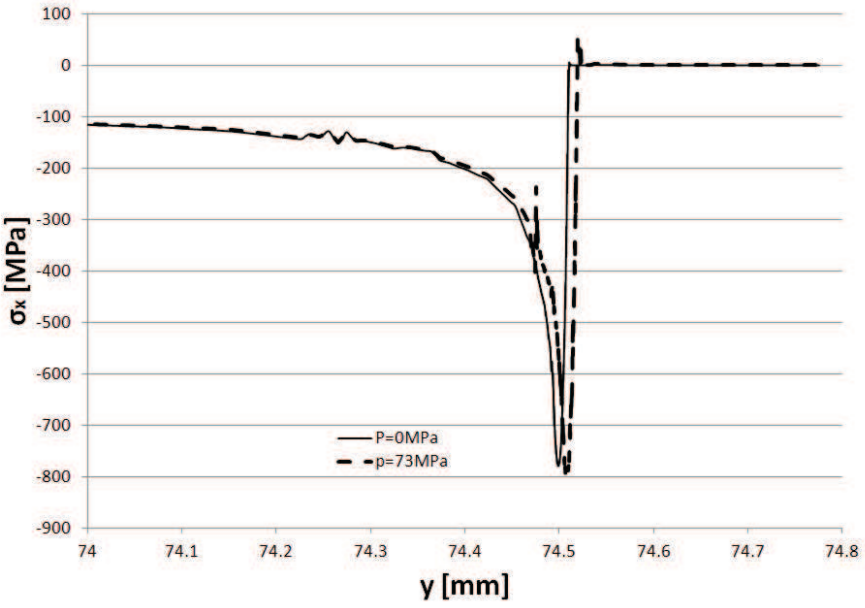

Figure 4.4: Coupling pressure σ_x of the shaft hub specimen with split collet pressure applied (thick dashed line) and without split collet pressure (thin solid line).

It is known that excessive eccentricity of the specimen could negatively affect the results of rotating bending tests [66]. In the case of a plain specimen, such issue is easily solved by accurate machining. For the shaft hub specimen, achieving a satisfactory eccentricity is not quite obvious. There are two aspects to consider: (i) the specimen is made up of two pieces, (ii) pieces must be joined together. As for the first aspect, it is obvious that the total circumferential runout of a two pieces specimen would be the sum of the runout of its shaft and hub. Therefore, a narrower tolerance range shall be defined for each single part, with respect to the total circumferential runout of the plain specimen. As for the second issue, it must be taken into account that, ideally, it should be avoided an assembly procedure comprising press fitting. In fact, rotating bending specimens are comparatively slender objects, therefore press fitting, which is performed in compression, could imply some residual curvature of the parts after assembly, due to buckling. Moreover, it must be considered that joining two components made of the same material

and without any surface treatment, means that they would likely undergo some, even small, alteration of the surface finishing in the coupling area [68, 69]. In order to screen out variables related to differences in surface finishing and (as much as possible) in total runout, it was decided to join the parts by shrink fitting. Shrink fitting is done by heating the hub up to 400°C then driving the shaft, kept at room temperature, into the hub by hands. Doing that way, no scratches are made on the contact surface as well as no risk of buckling exists any longer. A total of twenty seven shaft hub specimens were manufactured: a picture of some assembled specimens is reported in Fig. 4.5.

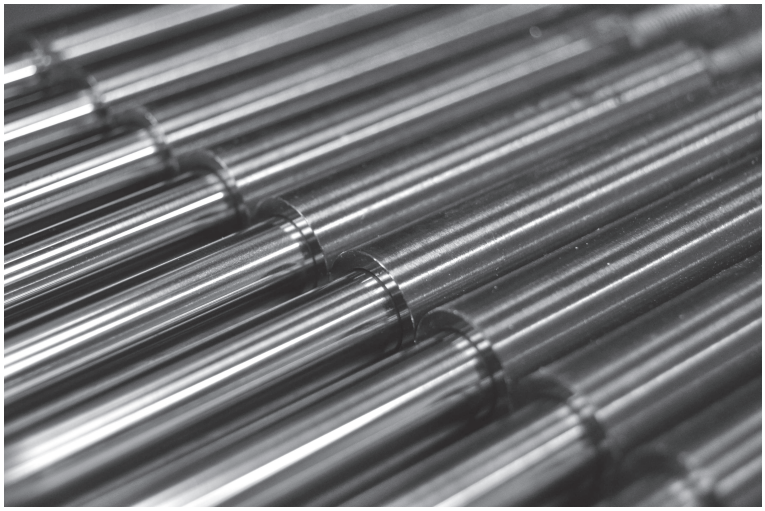

Figure 4.5: Close up of some shaft hub specimens.

4.1.2 Material

Both the plain and the shaft hub specimens were built in C40 steel [70], normalized and then cold drawn in 16mm diameter bars. Mechanical characteristics of the semi finished product are given in Tab. 4.2, according to [71]. The whole lot of specimens was realized from nominally identical bars.

Table 4.2: C40 UNI EN 10083 - 2, cold drawn in bars - mechanical characteristics according to [71].

Diameter [mm]	HB	$R_{p0.2}$ min. [MPa]	R_m [MPa]	A% min. [-]
$10 < D \leq 16$	163-211	460	650-980	7

Brinell hardness was measured on every specimen received. Moreover, one specimen was tested in tension on a standing press, in order to assess the actual

$R_{p0.2}$, R_m and $A\%$ of the received material. Results are illustrated in Tab. 4.3.

Table 4.3: C40 cold drawn in bars: actual mechanical characteristics of the tested lot.

Diameter [mm]	HB avg.	$R_{p0.2}$ [MPa]	R_m [MPa]	$A\%$ [-]
16	210	510	800	8

It is possible to observe that the material received conforms with limitations reported in Tab. 4.2.

4.1.3 Measurements and pairs matching

All the specimens were numbered upon arrival. Code CXX was assigned to every plain specimen while codes SYY and HZZ were assigned to shafts and hubs respectively. All the key dimensions and roughnesses were controlled on every single specimen. For the sake of brevity, plain specimens data are not reported here, anyway their dimensions and roughnesses conformed with those indicated in the drawing of Fig. 4.9. As for shaft hub specimens, first their diameters were measured, then pairs were formed in order to minimize discrepancies in the interference value across the batch. Each pair takes its name from the combination of shaft and hub names ($SYYHZZ$). The average value of interference was $I_{avg} = 0.014mm$. Specimens pairs, along with their interference levels and interference error evaluated with respect to I_{avg} are reported in Tab. 4.4. Lastly, as a means for checking the value of the radius realised at the hub bore edge, some more hubs were ordered. They were then cut in two halves in order to measure the radius with a caliper and to control the actual roughness at the hub internal surface. As it can be seen in Fig. 4.6, the radius is quite well realized, and very close to the required value of $r_r = 0.5mm$. Due to manufacturing reasons, the roughness of the hub bore surface was $R_{a\_H} = 0.68$, quite higher than the one of the shaft $R_{a\_S} = 0.20$.

Table 4.4: Interference level on shaft hub pairs, error with respect to average interference I_{avg} and total runout at the test bench.

Shaft		Hub		Interference [mm]	Error %	Total runout at bench [mm]
S	27	H	13	0.013	2.66%	0.10
S	17	H	17	0.013	2.66%	0.04
S	34	H	30	0.014	4.83%	0.06
S	14	H	15	0.014	4.83%	0.08
S	13	H	16	0.014	4.83%	0.10
S	26	H	25	0.014	4.83%	0.11
S	16	H	21	0.012	10.14%	0.03
S	25	H	23	0.012	10.14%	0.15
S	9	H	12	0.015	12.32%	0.07
S	30	H	18	0.015	12.32%	0.04
S	18	H	4	0.015	12.32%	0.03
S	2	H	8	0.011	17.63%	0.25
S	8	H	24	0.011	17.63%	0.06
S	32	H	26	0.011	17.63%	0.05
S	21	H	27	0.011	17.63%	0.01
S	6	H	10	0.016	19.81%	0.15
S	11	H	32	0.010	25.12%	0.04
S	23	H	28	0.010	25.12%	0.09
S	19	H	6	0.017	27.29%	0.13
S	33	H	9	0.017	27.29%	0.04
S	22	H	20	0.009	32.61%	0.12
S	15	H	29	0.009	32.61%	0.08
S	28	H	2	0.018	34.78%	0.06
S	12	H	3	0.018	34.78%	0.09
S	24	H	5	0.018	34.78%	0.10
S	3	H	1	0.019	42.27%	0.07

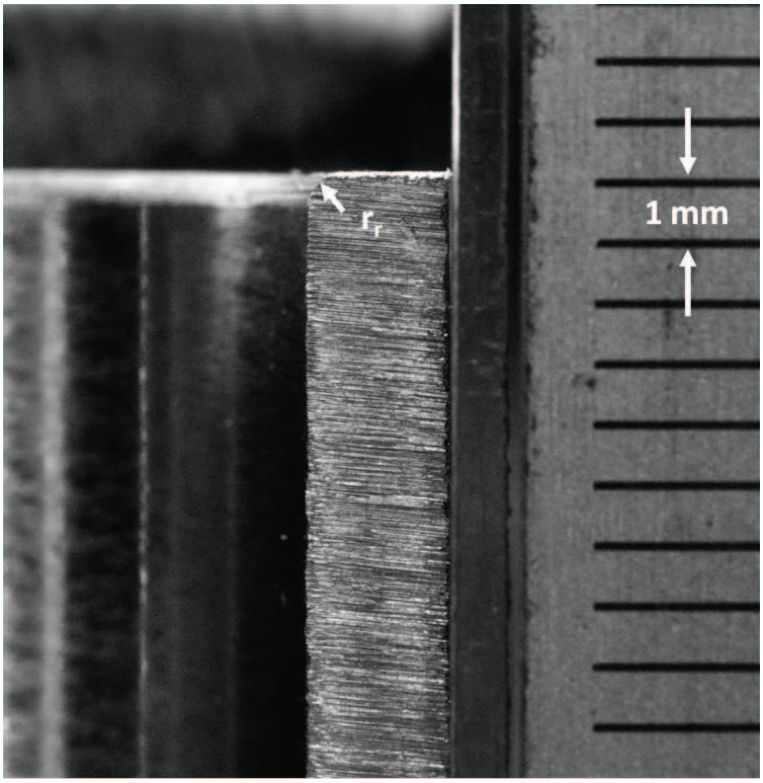

Figure 4.6: Sectioned hub, r_r radius control.

4.2 Results

The primary aim of the testing plan was to find out the endurance limit of the shaft hub ("notched") specimen to be compared with that of the base material (plain specimen). All the specimens were tested at $n = 2400rpm$ and plain specimens were tested first. By means of the staircase method illustrated in [67], an endurance limit (50% at $2 \cdot 10^6$cycles) of $S_{n\_plain} = 364MPa$ was obtained, with a standard deviation of $\hat{\sigma}_{pl} = 6.12MPa$. The S-N curve for the base material is reported in Fig. 4.7. As expected, all the failures happened in the central part of the specimen (see Fig. 4.9). Some photographs of the fracture surfaces are reported in 4.3. As for shaft hub specimens, an endurance limit (50% at $2 \cdot 10^6$cycles) of $S_{n\_sh} = 210MPa$ was obtained, with a standard deviation of $\hat{\sigma}_{pl} = 9.04MPa$. The S-N curve for the base material is reported in Fig. 4.8. Therefore, by comparing the two endurance limits, it is possible to retrieve the fatigue stress concentration factor K_f, as follows:

$$K_f = \frac{S_{n\_plain}}{S_{n\_sh}} = \frac{364}{210} = 1.73 \tag{4.2}$$

All failures took place at the end of the hub radius, suggesting that crack propagation is driven by σ_y peaks shown in 3. Some images of fracture surfaces are reported in 4.3. Recalling the definition of K_f ([72]):

$$K_f = 1 + q \cdot (K_t - 1) \tag{4.3}$$

where $0 \leq q \leq 1$ is the material notch sensitivity, it is known that $K_f \leq K_t$. Therefore, comparing results shown in Fig. 3.33 for K_t in the case of $I = 0.014mm$ with the result shown above for K_f it can be seen that the actual K_f is greater than expected. Such outcome suggests that K_t defined as for 3.17 is not suitable for describing the fatigue behaviour of the joint. Future developments of the FEA models, briefly introduced at the end of the previous chapter, will hopefully allow overcoming such discrepancy.

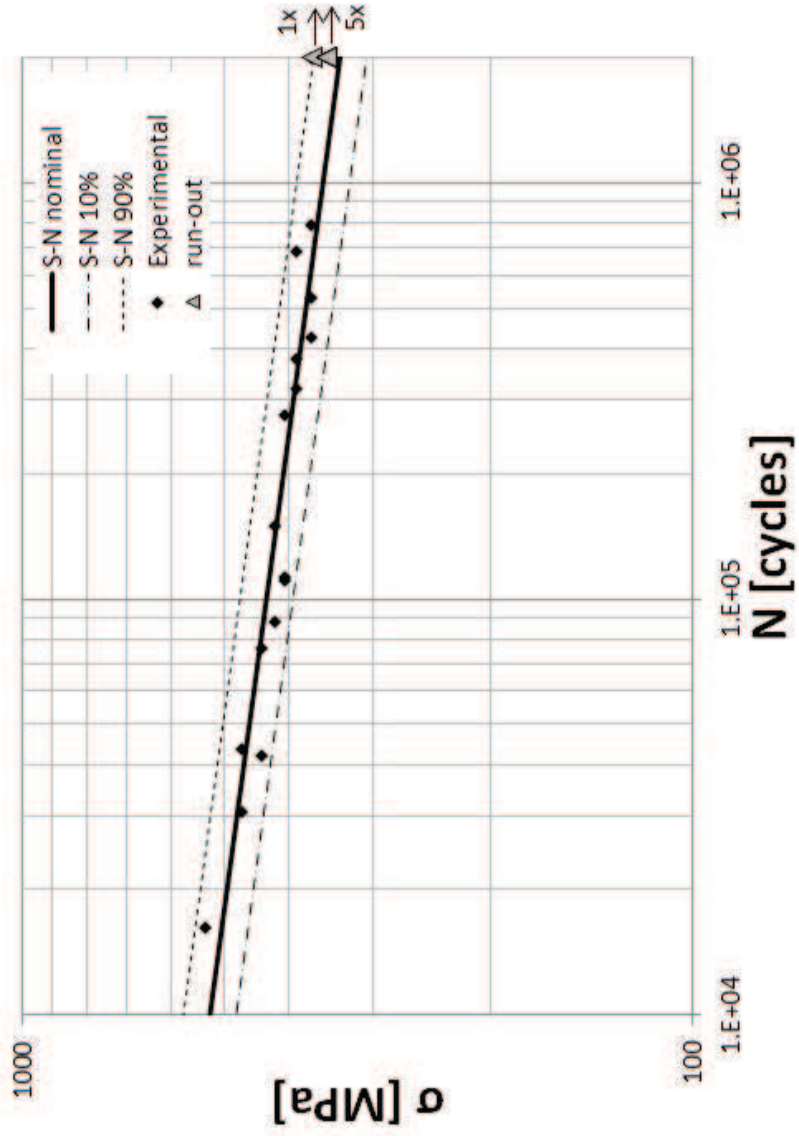

Figure 4.7: S-N curve for the base material (plain specimen).

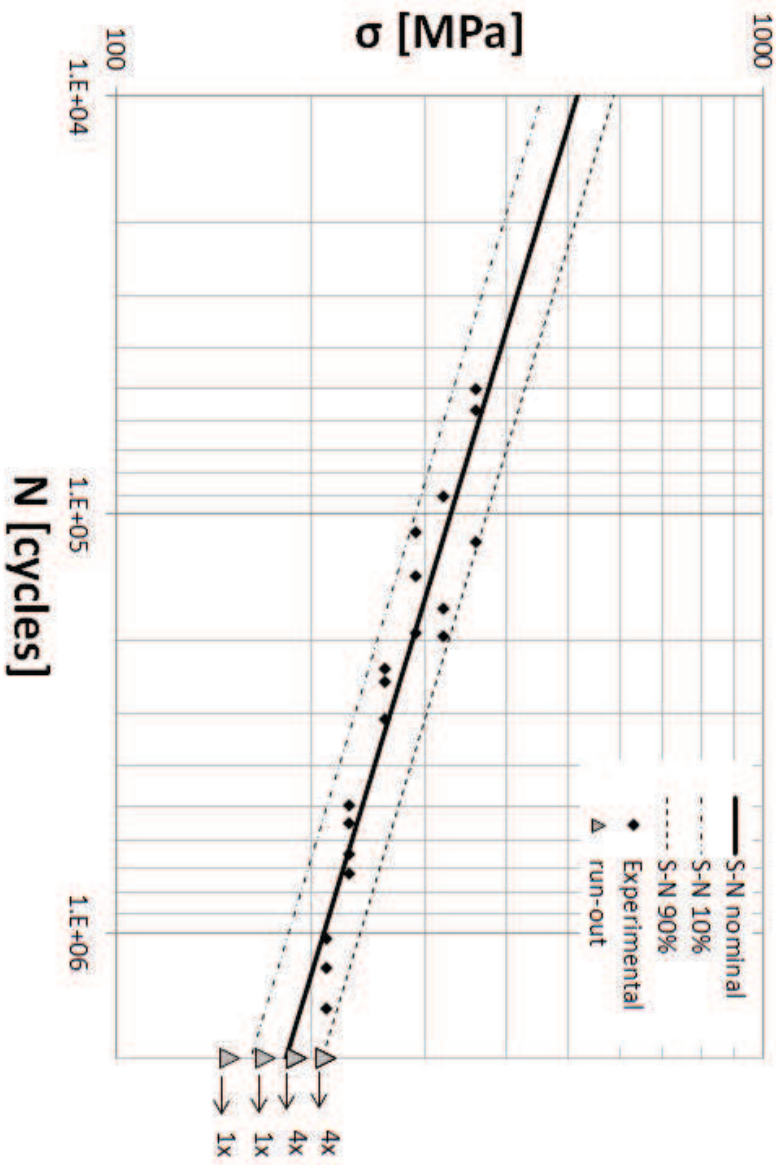

Figure 4.8: S-N curve for the notched specimen.

4.3 Appendix

4.3.1 Drawings

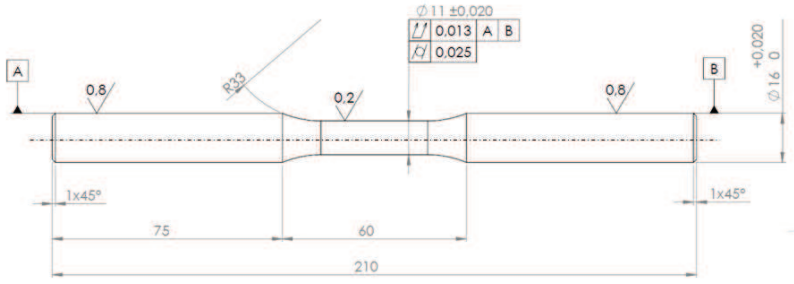

Figure 4.9: Plain specimen for rotating bending tests according to ISO1143.

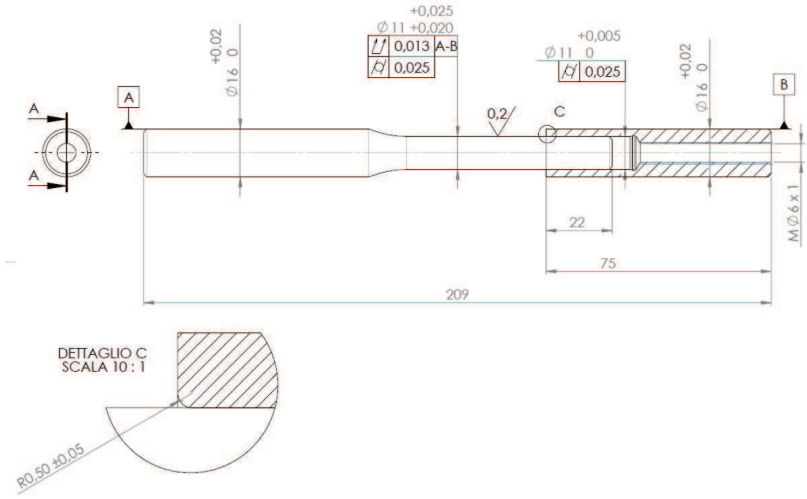

Figure 4.10: Shaft hub specimen for rotating bending tests according to ISO 1143

4.3.2 Plain specimen - fracture surfaces

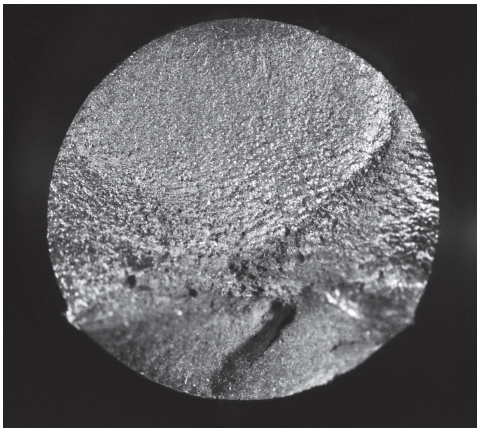

Figure 4.11: Fracture surface of specimen C3, $\sigma_{y\text{-}RS} = 440MPa$, $n = 75,777cycles$.

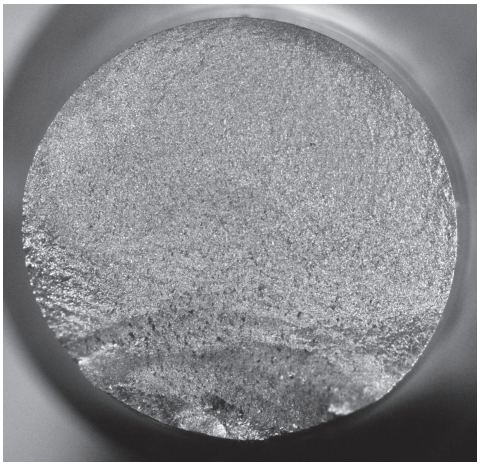

Figure 4.12: Fracture surface of specimen C12, $\sigma_{y\text{-}RS} = 370MPa$, $n = 1,985,572cycles$.

4.3.3 Shaft hub specimen - fracture surfaces

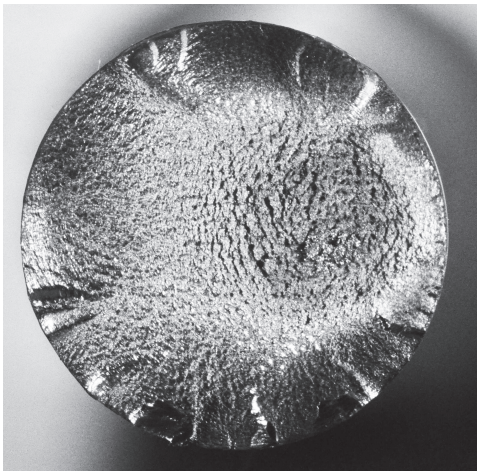

Figure 4.13: Fracture surface of specimen S19H6, $\sigma_{y\_RS} = 358MPa$, $n = 120,376cycles$.

Figure 4.14: Fracture surface of specimen S19H6, $\sigma_{y\_RS} = 358MPa$, $n = 120,376cycles$, view of the hub side.

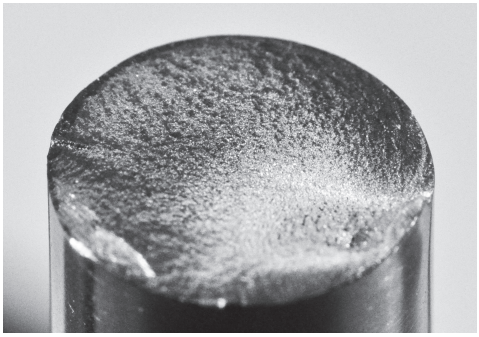

Figure 4.15: Fracture surface of specimen S28H2, $\sigma_{y\_RS} = 211MPa$, $n = 1,518,646 cycles$.

Figure 4.16: Fracture surface of specimen S28H2, $\sigma_{y\_RS} = 211MPa$, $n = 1,518,646 cycles$, view of the hub side.

Chapter 5

Conclusion

Stresses on the frame of motorbike forks were evaluated in this work. Particularly, bending stresses due to an emergency braking, at the joint between the fork clamp and the leg, were calculated analytically. Some optimization strategies, aimed at levelling the stress state of the two legs in single disc architectures were proposed. The analytical formulae were validated referring to some production forks, both by finite element analyses and by experimental mechanics road tests. Then, a numerical study began, targeted to developing efficient models for evaluating stress concentration factors in the aforementioned joint, initially idealized as an axisymmetric shaft hub interference fit, with applied external loads. Some important indications came from such numerical investigation, even if the models still need development. Lastly, a novel specimen was designed, aimed at performing accelerated fatigue tests to evaluate the fatigue stress concentration in interference fitted shaft hub couplings. Combining experimental techniques based on such specimen and some improved numerical models, will hopefully allow evaluating the fatigue performance of shaft hub couplings subjected to external bending loads.

Bibliography

[1] E. Koch. Bicycle. *U.S. Patent*, (680,048), 1901.

[2] E. D. Thompson. Bicycle. *U.S. Patent*, (598,186), 1898.

[3] A. A. Scott. Improvements in or connected with the front forks of motorcycles. *G.B. Patent*, (7,845), 1909.

[4] W. S. Harley. Shock absorber. *U.S. Patent*, (1,527,133), 1925.

[5] Aktieselskabet Fisker & Nielsen; P. A. Fisker. Improvements in and relating to handles and front fork for cycles, particularly for motor cycles. *G.B. Patent*, (416,594), 1934.

[6] R. Schleicher. Flüssigkeitsstoßdämpfer für Kraftradgabeln. *DE Patentschrift*, (675,926), 1939.

[7] Dowty Equipment Limited; P. W. Burke; R. P. Wildey Morris; A. A. John Willitt. An improved telescopic strut or shock absorber. *G.B. Patent*, (597,036), 1948.

[8] P. L. Torre. Spring suspension system for motorbike front wheels. *U.S. Patent*, (2,756,070), 1956.

[9] A. Roder. Schwinghebel-Federgabellagerung, insbesondere für das Vorderrad von Motorrädern oder Motorrollern. *DE Patentschrift*, (1,043,844), 1958.

[10] E. Turner. Motorcycle front wheel suspension. *U.S. Patent*, (2,953,395), 1960.

[11] J. P. Roberts. Telescoping, spring-loaded, hydraulically damped shock absorber. *U.S. Patent*, (3,447,797), 1968.

[12] Arces S.r.l. Perfezionamento nelle sospensioni per motoveicoli. *ITA Brevetto per invenzione industriale*, (1,039,678), 1979.

[13] M. Kashima. Front end shock absorbing apparatus for wheeled vehicle. *U.S. Patent*, (4,295,658), 1981.

[14] G. Neupert; H. Sydekum. Valvola di trafilamento per ammortizzatori idraulici pneumatici o idropneumatici. *ITA Brevetto per invenzione industriale*, (1,145,747), 1986.

[15] A. H. I. Verkuylen. Hydraulic shock damper assembly for use in vehicles. *U.S. Patent*, (4,732,244), 1988.

[16] H. Shelton, J. Obie Sullivan, and K. Gall. Analysis of the fatigue failure of a mountain bike front shock. *Engineering Failure Analysis*, 11(3):375 – 386, 2004.

[17] D. Croccolo, R. Cuppini, and N. Vincenzi. The design and optimization of fork-pin compression coupling in front motorbike suspensions. *Finite Elements in Analysis and Design*, 43(13):977 – 988, 2007.

[18] D. Croccolo, R. Cuppini, and N. Vincenzi. Friction coefficient definition in compression-fit couplings applying the doe method. *Strain*, 44(2):170 – 179, 2008.

[19] D. Croccolo and N. Vincenzi. A generalized theory for shaft-hub couplings. *Proceedings of the Institution of Mechanical Engineers, Part C: Journal of Mechanical Engineering Science*, 223(10):2231–2239, 2009.

[20] D. Croccolo, R. Cuppini, and N. Vincenzi. Design improvement of clamped joints in front motorbike suspension based on fem analysis. *Finite Elements in Analysis and Design*, 45(6-7):406 – 414, 2009.

[21] D. Croccolo, M. De Agostinis, and N. Vincenzi. Recent improvements and design formulae applied to front motorbike suspensions. *Engineering Failure Analysis*, 17(5):1173 – 1187, 2010.

[22] D. Croccolo, M. De Agostinis, and N. Vincenzi. Failure analysis of bolted joints: Effect of friction coefficients in torque-preloading relationship. *Engineering Failure Analysis*, 18(1):364 – 373, 2011.

[23] J. F. Doyle. *Modern experimental stress analysis*. John Wiley & Sons, Ltd, Chichester, GB, 2004.

[24] H. B. Pacejka. *Tire and vehicle dynamics*. Butterworth-Heinemann, Oxford, GB, 2002.

[25] V. Cossalter. *Motorcycle dynamics*. Lulu.com, 2006.

[26] M. Corno, S. M. Savaresi, M. Tanelli, and L. Fabbri. On optimal motorcycle braking. *Control Engineering Practice*, 16(6):644–657, JUN 2008.

[27] V. Cossalter, R. Lot, and F. Maggio. On the stability of motorcycle during braking. In *Proceedings of the Small Engine Technology Conference and Exhibition*, Graz, A, September 2004.

[28] D. Croccolo, M. De Agostinis, and N. Vincenzi. An analytical approach to the structural design and optimization of motorbike forks. *Proceedings of the Institution of Mechanical Engineers, Part D: Journal of Automobile Engineering*, 226(2):158–168, 2012.

[29] O. Belluzzi. *Scienza delle costruzioni*, volume 2. Zanichelli, Bologna, IT, 1994.

[30] S. Timoshenko and J. N. Goodier. *Theory of elasticity*. McGraw-Hill Book Company, New York, US, 1951.

[31] D. Croccolo, M. De Agostinis, and N. Vincenzi. Influence of tightening procedures and lubrication conditions on titanium screw joints for lightweight applications. *Tribology International*, 55:68–76, NOV 2012.

[32] D. Croccolo, M. De Agostinis, and N. Vincenzi. A contribution to the selection and calculation of screws in high duty bolted joints. *International Journal of Pressure Vessels and Piping*, 96-97:38–48, AUG-SEP 2012.

[33] W. Weitz. *Dubbel: Manuale di ingegneria meccanica - Parte 1*. Edizioni di Scienza e Tecnica Milano, IT, 1984.

[34] N. Vincenzi. *Studio statico e dinamico di accoppiamenti albero-mozzo in assenza di assialsimmetria, Ph.D. Thesis*. Universitá degli Studi di Firenze, IT, 2010.

[35] F. G. Kollmann. *Welle-Nabe Verbindungen. Konstructionsbucher Bd.32*. Springer-Verlag, Berlin, DE, 1984.

[36] A. Strozzi. *Costruzione di macchine*. Pitagora editrice, Bologna, IT, 1998.

[37] H. Niemann, G. Winter and B. R. Hohn. *Maschinenelemente*. Springer-Verlag, Berlin, DE, 2005.

[38] D Castagnetti and E Dragoni. Optimal aspect ratio of interference fits for maximum load transfer capacity. *Journal of Strain Analysis for Engineering Design*, 40(2):177–184, FEB 2005.

[39] D. Croccolo, M. De Agostinis, and N. Vincenzi. Design and optimization of shaft-hub hybrid joints for lightweight structures: Analytical definition of normalizing parameters. *International Journal of Mechanical Sciences*, 56(1):77–85, 2012.

[40] N Baldanzini. A general formulation for designing interference-fit joints with elastic-plastic components. *Journal of Mechanical Design*, 126(4):737–743, JUL 2004.

[41] D. Croccolo and N. Vincenzi. Stress concentration factors in compression-fit couplings. *Proceedings of the Institution of Mechanical Engineers part C-Journal of Mechanical Engineering Science*, 224(C6):1143–1152, 2010.

[42] M. V. Barton. The circular cylinder with a band of uniform pressure on a finite length of the surface. *Journal of Applied Mechanics*, 63():97â104, 1941.

[43] A. W. Rankin. Shrink fit stresses and deformations. *Journal of Applied Mechanics*, 66():77–85, 1944.

[44] J. N. Goodier and C. B. Loutzenheiser. Pressure peaks at the ends of plane strain rigid die contacts (elastic). *Journal of Applied Mechanics*, 32():462–463, 1965.

[45] M. Ciavarella, D.A. Hills, and G. Monno. The influence of rounded edges on indentation by flat punch. *Proceedings of the Institution of Mechanical Engineers part C-Journal of Mechanical Engineering Science*, 212(4):319–328, 1998.

[46] A. Pioli, A. Strozzi, A. Baldini, M. Giacopini, and R. Rosi. Influence of the initial clearance on the peak stress in connecting-rod small ends. *Proceedings of the Institution of Mechanical Engineers part D -Journal of Automobile Engineering*, 223(D6):769–782, JUN 2009.

[47] A. Strozzi, A. Baldini, M. Giacopini, E. Bertocchi, and L. Bertocchi. Normalization of the stress concentrations at the rounded edges of a shaft-hub interference fit. *Journal of Strain Analysis for Engineering Design*, 46(6):478–491, 2011.

[48] D. Croccolo, M. De Agostinis, and N. Vincenzi. Normalization of the stress concentrations at the rounded edges of a shaft-hub interference fit: extension to the case of a hollow shaft. *Journal of Strain Analysis for Engineering Design*, 47(3):131–139, APR 2012.

[49] M. Bijakzochowsky, P. Marek, and M. Tracz. On methods of reduction and elimination of stress singularities in some elastic contact problems. *International Journal of Mechanical Sciences*, 36(4):279–296, APR 1994.

[50] D. J. White and J. Humpherson. Finite-element analysis of stresses in shafts due to interference-fit hubs. *Journal of Strain Analysis for Engineering Design*, 4():105–114, 1969.

[51] F. Kolonits. The influence of rounded edges on the shaftâhub contact. *Periodica Polytechnica Transportation Engineering*, 51():35–44, 2007.

[52] A Strozzi. Static stresses in an unpressurized, rounded, rectangular, elastomeric seal. *ASLE Transactions*, 29(4):558–564, OCT 1986.

[53] O. A. Olukoko, A. A. Becker, and R. T. Fenner. Three benchmark examples for frictional contact modelling using finite element and boundary element methods. *Journal of Strain Analysis for Engineering Design*, 28(4):293–301, OCT 1993.

[54] A. Özel, S. Temiz, M. D. Aydin, and S. Sen. Stress analysis of shrink-fitted joints for various fit forms via finite element method. *Materials & Design*, 26(4):281–289, JUN 2005.

[55] F. Lanoue, A. Vadean, and B. Sanschagrin. Finite element analysis and contact modelling considerations of interference fits for fretting fatigue strength calculations. *Simulation Modeling Practice and Theory*, 17(10):1587–1602, NOV 2009.

[56] F. Kolonits. Fretting in a hub - axle press fit joint. In , editor, *Proceedings of the 10th mini conference on vehicle system dynamics, identification and anomalies*, volume , page 573 â 584, Budapest, HU, November 2006. . .

[57] K.L. Johnson. *Contact Mechanics*. Cambridge University Press, Cambridge, GB, 1985.

[58] E. Viola. *Scienza delle Costruzioni*, volume 3. Pitagora Editrice, Bologna, IT, 1992.

[59] T. Chakherlou, Y. Alvandi-Tabrizi, and A. Kiani. On the fatigue behavior of cold expanded fastener holes subjected to bolt tightening. *International Journal of Fatigue*, 33(6):800–810, 2011.

[60] D. Croccolo, M. De Agostinis, and N. Vincenzi. Interference fit effect on holed single plates loaded with tension-tension stresses. *Frattura ed Integrita Strutturale*, 21:13–20, 2012.

[61] W Eichlseder. Fatigue analysis by local stress concept based on finite element results. *Computers & Structures*, 80(27-30):2109–2113, NOV 2002. 5th International Conference on Computational Structures Technology/2nd International Conference on Engineering Computational Technology, LEUVEN, BELGIUM, SEP 06-08, 2000.

[62] H.-P. Gaenser, K. Glinsner, and W. Eichlseder. Dimensioning against fatigue - stress-based approach or fracture mechanics? *Proceedings of the Institution of Mechanical Engineers part C-Journal of Mechanical Engineering Science*, 220(8):1109–1120, AUG 2006.

[63] Hans-Peter Gaenser. Some notes on gradient, volumetric and weakest link concepts in fatigue. *Computational materials science*, 44(2):230–239, DEC 2008.

[64] D Bellett, D Taylor, S Marco, E Mazzeo, J Guillois, and T Pircher. The fatigue behaviour of three-dimensional stress concentrations. *International Journal of Fatigue*, 27(3):207–221, MAR 2005.

[65] F. Berto and P. Lazzarin. Relationships between J-integral and the strain energy evaluated in a finite volume surrounding the tip of sharp and blunt V-notches. *International Journal of Solids and Structures*, 44(14-15):4621–4645, JUL 2007.

[66] ISO. *1143 Metallic materials - Rotating bar bending fatigue testing*. Ii edition, 2010.

[67] ISO. *12107 Metallic materials - Fatigue testing - Statistical planning and analysis of data*. I edition, 2003.

[68] D. Croccolo, M. De Agostinis, and N. Vincenzi. Static and dynamic strength evaluation of interference fit and adhesively bonded cylindrical joints. *International Journal of Adhesion and Adhesives*, 30(5):359 – 366, 2010. Special Issue on Joint Design.

[69] D. Croccolo, M. De Agostinis, and N. Vincenzi. Experimental analysis of static and fatigue strength properties in press-fitted and adhesively bonded steel-aluminium components. *Journal of Adhesion Science and Technology*, 25(18):2521–2538, 2011.

[70] UNI EN. *10083-2 Steels for quenching and tempering - Technical delivery conditions for non alloy steels.* I edition, 2006.

[71] UNI EN. *10027-2 Bright steel products - Technical delivery conditions.* I edition, 2000.

[72] R.C. Juvinall and K.M. Marshek. *Fondamenti della progettazione dei componenti delle macchine.* ETS, 1994.